Optimisation of mechanical Metamaterials using Machine Learning

-Establishing a new Workflow-

Dissertation

zur Erlangung des Grades

des Doktors der Ingenieurwissenschaften

der Naturwissenschaftlich-Technischen Fakultät

der Universität des Saarlandes

von

Stefan Bronder, M.Sc.

Saarbrücken

2023

Tag des Kolloquiums:	1. September 2023
Dekan:	Prof. Dr. Ludger Santen
Berichterstatter:	Prof. Dr.-Ing. Dr.rer.nat. Anne Jung
	Prof. Dr.-Ing. Dirk Bähre
	Prof. Dr. Zoran Ren
Akad. Mitarbeiter:	Dr.-Ing. Prateek Sharma
Vorsitz:	Prof. Dr. Andreas Schütze

Abstract

Optimised design, either for components or materials, is a topic on the rise in our century. It is strongly linked with the thought of lightweight construction and resource management. Thus, the aim of this work is to provide a faster way to optimise the microstructure of mechanical metamaterials utilising machine learning. An optimisation scheme with neural networks is developed and experimentally validated on auxetic materials, with their governing property being a negative Poisson's ratio. This method consists of multiple steps, beginning with finding a representative volume element, followed by an investigation of the design space, creation of a database to train a neural network and finalised by an optimisation of the structure. Each step is validated by experiments and corrections to the model are applied if necessary. For the auxetics the aim is to find the structure with the maximal mass specific energy absorption capacity and negative as possible Poisson's ratio. The final optimisation routine is then transferred to another metamaterial structure, the pentamodes. Here, an investigation and successful optimisation for maximised damping and stiffness solely based on simulations is launched. In addition, adaptive sampling is applied in order to reduce the required number of simulations.

Zusammenfassung

Optimiertes Design, sei es für Bauteile oder Materialien, ist ein Thema, das in unserem Jahrhundert immer mehr an Bedeutung gewinnt. Es ist eng mit dem Gedanken des Leichtbaus und des Ressourcenmanagements verbunden. Ziel dieser Arbeit ist es daher, einen schnelleren Weg zur Optimierung der Mikrostruktur mechanischer Metamaterialien mit Hilfe von maschinellem Lernen zu finden. Es wird ein Optimierungsverfahren mit neuronalen Netzen entwickelt und experimentell an auxetischen Materialien validiert, deren maßgebliche Eigenschaft eine negative Poissonzahl ist. Diese Methode besteht aus mehreren Schritten, beginnend mit der Suche nach einem repräsentativen Volumenelement, gefolgt von einer Untersuchung des Designraums, der Erstellung einer Datenbank zum Trainieren eines neuronalen Netzes und abschließend einer Optimierung der Struktur. Jeder Schritt wird durch Experimente validiert und bei Bedarf werden Korrekturen am Modell vorgenommen. Für die auxetische Struktur ist das Ziel, die Struktur mit der maximalen massenspezifischen Energieabsorptionskapazität und einer möglichst negativen Poisson-Zahl zu finden. Die abschließende Optimierungsroutine wird auf eine weitere Metamaterialstruktur, die Pentamodstrukturen, übertragen. Hier wird eine Untersuchung und erfolgreiche Optimierung zur Maximierung von Dämpfung und Steifigkeit allein auf Basis von Simulationen gestartet. Zusätzlich wird ein adaptives Sampling angewandt, um die Anzahl der erforderlichen Simulationen zu reduzieren.

Danksagung

Ich möchte mich bei all jenen bedanken, die mich während der Anfertigung dieser Dissertation unterstützt und motiviert haben.

Besonders gilt mein Dank Frau Prof. Dr.-Ing. Dr. rer. nat. Anne Jung für die spannende Themenstellung, die wunderbare Betreuung und die Begutachtung dieser Arbeit. Zudem gilt mein Dank Herrn Prof. Dr.-Ing. Dirk Bähre, der mich als Zweitgutachter unterstützt hat und an dessen Lehrstuhl sämtliche Proben gefertigt wurden.

Für die Herstellung der Proben bedanke ich mich ganz herzlich bei Franziska Herter und Cecilia Klein vom Lehrstuhl für Fertigungstechnik.

Des Weiteren möchte ich mich herzlich bei Herrn Prof. Dr.-Ing. Stefan Diebels, für die Möglichkeit die Arbeit an seinem Lehrstuhl durchzuführen, bedanken.

Ganz herzlich bedanke ich mich bei Sergej Grednev, Janis Mathieu und Alexander Engel, die alle wichtige Beiträge zur Entstehung dieser Dissertation geleistet haben.

Ein besonderer Dank gilt auch Michael Fries, Francesco Kunz, Farshad Daneshpazoonejad, Laura Lindner und Rebecca Kose, die mir stets mit Rat und Tat zur Seite standen und die auch bei Misserfolgen aufmunternde Worte übrig hatten.

Auch allen Mitarbeitenden des Lehrstuhls danke ich für die immerwährende Hilfe und den Beistand während meiner Zeit als Mitarbeiter.

Saarbrücken, 20.01.2023 Stefan Bronder, M.Sc.

Contents

1

Motivation and Introduction

Humanity and thus engineering science today is increasingly confronted with the demand of stronger, cheaper materials with multi-functionality whilst saving resources. Hence, microstructured materials are of growing interest since porous materials save resources and mass for lightweight construction in addition to exhibiting other special properties. For example, octett truss structures display a higher specific stiffness than solid materials. There are also microstructures, such as auxetic materials, which show unusual properties, in this case a negative Poisson's ratio thereby increasing other properties as well [85]. In combination with the advances in additive manufacturing technologies, such microstructured materials can be tailored and optimised for specific tasks not only virtually. Complex geometries can easily be manufactured and experimented on.

The optimisation and tailoring process can be done with finite element (FE) simulations either as topology optimisation to find new microstructures with desired properties or as parametrised optimisation to enhance existing microstructures. Even though computational resources are fast developing, those optimisation processes are computationally costly and the simulation solely based on FE programs is very time consuming. A remedy is provided through the field of machine learning (ML). This subfield of artificial intelligence denotes to a class of algorithms capable of learning arbitrary functions based on data. Thus, ML algorithms can learn a material behaviour based on a few simulations.

The aim of this work is to optimise an auxetic re-entrant honeycomb structure and a pentamode structure for energy absorption purposes or vibration damping, respectively. Each microstructure is parametrised and a feasible geometry space is investigated. Therefore, combinations of geometry parameters are used to build up models which were then simulated and the desired properties extracted. To speed up the optimisation, neural networks were trained to predict the material behaviour based on the FE simulations in order to handle the optimisation.

Thus, only a few simulations were necessary to generate sufficient training data for the ML algorithm, which is then capable of handling the optimisation process. For the auxetic structures, the simulations and optimisation were validated with experiments. Selective laser melting (SLM) was used to manufacture specimens out of aluminium.

The amount of saved time is directly linked to the amount of FE simulations. Consequently, another aim was to minimise the number of simulations by introducing adaptive sampling. This means a sampling strategy to evaluate the feature space during training and find the most critical areas where training data would have the biggest impact on the quality of the ML predictions.

For a more detailed theoretical background the reader is referred to chapter 2. There, a short review of ML will be given, followed by a more detailed explanation of neural networks, topolgy optimisation in general, selective laser melting, mechanical metamaterial structures as well as an overview of design of experiment. Also recent advances especially in the field of material science will be investigated there.

In chapter 3, the optimisation procedure is developed on the example of auxetic structures. Starting with the investigation to find the representative volume element, followed by a more detailed explanation of the finite element simulations, the inspection of the design space, the explanation of the neural network training and finished with the experimental validation of the optimised structure, the reader is taken through the whole process of the optimisation and the development of the procedure.

The optimisation procedure is adapted to pentamode structures in chapter 4. There, the developed adaptive sampling is utilised. Due to time constraints the pentamode structures were investigated only with simulations. Within this chapter the simulation setup, the design space investigation, the adaptive sampling and neural network training, as well as the optimisation is explained in detail.

Chapter 5 summarises all important conclusions and provides a final discussion for the whole optimisation scheme. It is finalised with an outline of future work.

2

Theoretical Background

Within this chapter, a broad overview of the theories for the most important concepts used in this work is given. There is no extra chapter on FE method, since it is a well known simulation method and ABAQUS® was used as a solver software. In addition, each chapter contains recent advancements in the respective fields.

2.1 Machine learning

Machine learning (ML) as a subfield of artificial intelligence is thought of as a modern concept, but part of the mathematical foundation is more than a century old. The method of least squares for example was published by Legendre in 1805 even though Gauss claimed to have discovered it 10 years earlier [133]. However, this method is the basis for linear regression, which is already a simplistic machine learning algorithm. To clarify, Machine learning is the term for all algorithms, that are solely based on approximations through data and are capable of self modification. Whereas, artificial intelligence (AI) is a much broader term since it envelopes every algorithm that is able to recognise something and make a conclusion. So e.g. a simple if-else statement would already count as AI but it does not learn with more data, so it would not be machine learning. Another prominent term over the recent years is deep learning, which is exclusively reserved for neural networks and thus is a type of machine learning. Figure 2.1 summarises those connections. So in general ML describes a class of algorithms capable of learning from data.

The reason why ML gained popularity only recently is simply the technological advancements in computer science and computational power. Already in the 60's and 70's many algorithms, though mostly linear methods, were developed. But the lack of computational power hindered the study of those, especially the non-linear models [50].

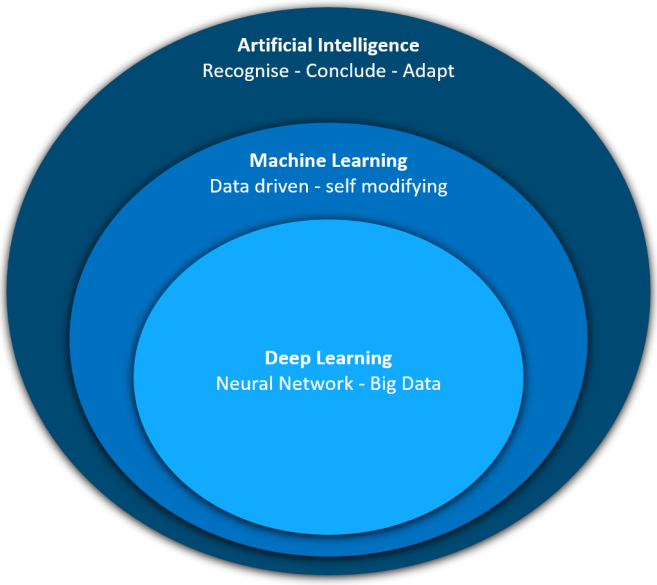

Figure 2.1: Classification of prominent terms in relation to artificial intelligence

In the field of mechanical engineering ML concepts are successfully used e.g. for predicting the surface roughness in wire electrical discharge machining [114]. Brillinger et al. [18] predicted energy consumption for CNC machining to ease the development of energy efficient machining strategies using tree-based algorithms. Hennebold et al. [64] employed different ML techniques to predict production cost of products during an early development stage. They found linear regression and k-nearest neighbours to produce the most reliable results even though not much of the final product is known during that stage of development. By using Gaussian process regression, Tamura et al. [136] were able to optimise the powder production process for Ni-Co superalloys.

In the context of material design, Xiong et al. [149] improved the accuracy and stability of empirical models which describe the transformation in shape-memory alloys. They used generated data by different ML tools to forgo expensive experiments. Generative adversarial networks were utilised by Challapalli et al. [27] in order to design new lattice structures which are superior to the known octet truss structure concerning mass and stiffness. The microstructure of polycrystalline Galfenol was optimised by Liu et al. [92] by applying different ML models to refine the search space and for feature selection, thus boosting the FE simulations. In general, ML concepts are applied in every engineering task either to replace or to improve conventional methods, hence making simulations faster, more time efficient or saving the trouble of many expensive experiments.

The focus of this work is the prediction of material properties with neural networks, which is a supervised regression task. Therefore, only this branch of ML algorithms is investigated in more detail in 2.2.

2.1.1 Basic terminology

To gain a better understanding of the chapters to come, here some basic terminology typically encountered when dealing with ML will be explained. First of all, ML concepts are typically divided into supervised learning, unsupervised learning and reinforcement learning. Supervised learning tries to predict a relation between a set of input variables and output variables. Therefore, the training data must consist of input variables, which are also called features, and **known** output variables, also referred to as predictors, targets or target values [113]. In contrast, unsupervised learning strives to find structure in data and thus has input features with **unknown** target values. A prominent example for unsupervised learning is clustering. Reinforcement learning as a third class describing a learning process through interaction with an environment and receiving rewards or punishments based on the outcome of an interaction. Learning occurs through an iterative exploration of the solution space, for example a robot learning to walk without falling [70].

As mentioned before, for supervised or unsupervised learning there is a so called training dataset or train set, which consists of all the samples used to adjust the model parameters, also often called hyper parameters, and thus enables it to make predictions. There usually exists also a validation dataset and a test dataset when working with ML. The validation data is used during the training to check the training process and to hinder an overfitting of the training data. Training in this case refers to the iteratively adjustment of the hyper parameters to achieve a better solution according to an error function. The test set is completely excluded from the modelling process and used to evaluate the final model performance after all hyper parameter tuning and training is finished. Thereby it ensures that there is no overfitting of the validation data.

Over- or underfittig are one major issue when working with ML. Overfitting occurs when the data points of the train set are almost perfectly matched, but when new data is introduced the predictions made by the model are highly error-prone (Figure 2.2). This can either happen due to a too complex model or a too perfect tuning of hyper parameters. When increasing complexity of a model, it gains flexibility and thus cannot only approximate the general dependencies but also unwanted details like noise for example. Yet, those details differ for different samples and when introducing new data, the model predicts badly [52]. The

other case, a too perfect tuned model, is due to a too long training process. The algorithm memorises the training data almost perfectly thereby raising expectations, yet produces bad predictions on new data [15]. In ccontrast, underfitting happens if the model is not complex enough to capture the dependencies between features and targets, thereby not being able to fit the training data within a reasonable error.

In total, overfitting is the more dangerous issue since it is disguised as good performance on the training data. Underfitting shows a general bad performance on all datasets and is discovered easier. The desired model should thus be complex enough to fit the overall dependencies but also simple enough not to find too much details. This choice off model complexity is also often referred to as the bias-variance trade-off [107]. This means a consistent model performance, even a bad one, is more desirable than a too good to be true performance which can not be upheld when applied to new data.

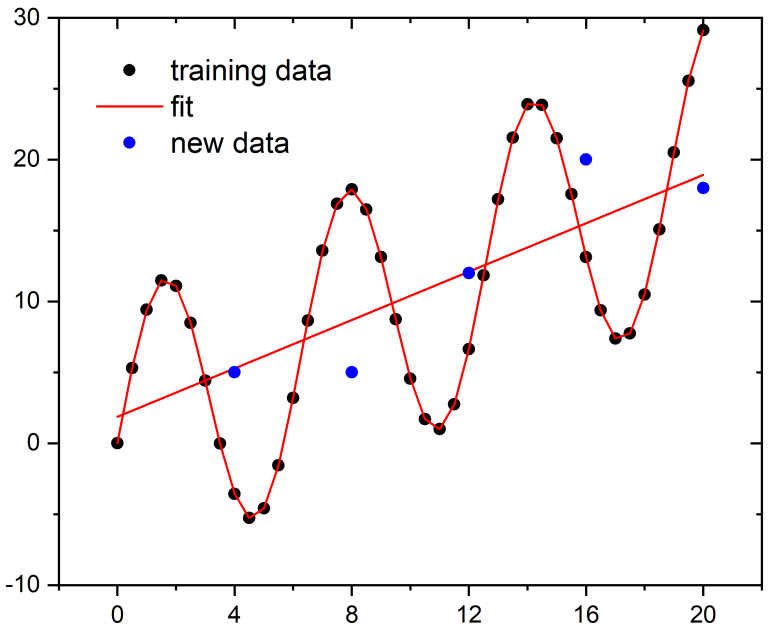

Figure 2.2: Example for overfitting, the linear fit approximates the training data imperfectly but can predict the new data with a smaller error than the perfect but complex fit of the training data.

In this context, there are often the terms generalisation and extrapolation in use. Generalisation describes the predictive performance on completely new data and is an indication of how well the trained model predicts on a real world application. Extrapolation is the property to give good estimated beyond the trained on

feature space. Most ML algorithms are only capable of performing well within the feature space that was covered by the training data.

A further division of the algorithms is the distinction in parametric and non-parametric. On the one hand, parametric algorithms make initial assumptions about the form of the function to learn and then only fit their tunable parameters, which is a fixed number determined by the chosen model. Linear regression or simple neural networks would be an example for parametric algorithms. On the other hand, non-parametric algorithms make no assumptions about the mapping function. They have hyper parameters too, but it is not a fixed number from the start of the training. An example for this would be the k-nearest neighbours method, which gives predictions of new data based on the k most similar training patterns.

Supervised learning is additionally divided into two main tasks, regression and classification. Regression means learning a mapping function for real valued output variables, e.g. predicting the market values of houses based on their size, location and building year. So a numerical quantity is learned. Classification refers to the assignment of a category to an input, e.g. telling if there is a picture of a cat or a dog. This leads to a discrete target space, where a prediction is either right or wrong. Most ML algorithms were first developed for classification, since this is by far the most prominent usage. Afterwards these algorithms were extended to perform regression tasks as well. Hence, the error metric for classification and regression differs. For regression the error needs to evaluate how well the prediction matched the target while for classification a hit or miss evaluation is necessary [70, 107, 132, 140].

2.1.2 Error functions

For regression tasks, there is only a handful of viable choices for the error function since it is not important if the prediction is good but rather how good or bad a prediction is. So for regression the aim is to minimise the error of the predictions. The most commonly used metrics are the mean squared error (MSE), mean absolute error (MAE), the Huber loss, the mean average percentage error (MAPE) and the coefficient of determination (R^2) [52, 107], which were also used within this work. Below, these metrics are introduced including their advantages and disadvantages. In all following definitions N is the total number of samples used to make the predictions, $\hat{y}_i$ the predicted target value for the i-th sample and y_i the true target value of the i-th sample.

Mean Squared Error

The MSE is the most popular error metric for regression tasks and is given by [132] as

$$\mathrm{MSE} = \frac{1}{N}\sum_{i}^{N}\left(\hat{y}_i - y_i\right)^2. \tag{2.1}$$

The main motivation behind the MSE is to avoid cancellation of single errors by summing over the squares since a prediction can either be larger or smaller than the true value. This metric puts a higher penalty on few larger errors than on many small ones, which makes it sensitive for outliers. However, the interpretation of the error is difficult because a squared unit does not make sense often.

Mean Absolute Error

When dealing with datasets with too many outliers, the MAE is often helpful. It is given by [52] as

$$\mathrm{MAE} = \frac{1}{N}\sum_{i}^{N}\left|\hat{y}_i - y_i\right|. \tag{2.2}$$

Here, the cancellation is forgone by summing over the absolute of the errors thereby preserving the original units and thus making it more interpretable.

Huber loss

This is basically a combination of MSE and MAE to use both their advantages and is given by [52] as

$$L_\delta = \begin{cases} \frac{1}{2}(\hat{y}_i - y_i)^2 & \text{for } |\hat{y}_i - y_i| \leq \delta \\ \delta|\hat{y}_i - y_i| - \frac{1}{2}\delta^2 & \text{otherwise} \end{cases}. \tag{2.3}$$

The δ parameter controls the piecewise definition or in other words when to use MAE or MSE.

Mean Average Percentage Error

All metrics presented above have the severe issue of scale dependency. In order to make those errors scale independent, the absolute error is divided by the corresponding target value. So the MAPE is given by [69]

$$\mathrm{MAPE} = \frac{1}{N}\sum_{i}^{N}\left|\frac{\hat{y}_i - y_i}{\hat{y}_i}\right|. \tag{2.4}$$

Since it provides a percentage error value, the measure can intuitively be understood. However, if the true values are close or equal to zero, the errors become arbitrarily high.

Coefficient of Determination

For regression tasks, the measure of the amount of variance in the target varaible R^2 is also a common error metric to estimate the quality of a fit. It is given by [5]

$$R^2 = 1 - \frac{\sum_{i=1}^{N}(y_i - \hat{y}_i)^2}{\sum_{i=1}^{N}(y_i - \overline{y})^2} \tag{2.5}$$

with $\overline{y}$ being the mean of the whole target vector. Hence, a R^2 value of 1 means the model is the best possible fit since it is able to explain all variance present in the data. If $R^2 = 0$, then the model is just fitting the mean of the target vector. There is also the possibility of R^2 becoming negative, which happens if the slopes of predictive model and actual target data have different signs. For example if the target values are oscillating and the model is capable to predict these oscillations, but with a phase shift, this would lead to negative R^2 scores, although the model might be satisfactory to the user.

2.2 Neural Networks

Arguably the most prominent example of a ML method are neural networks (NN). The first idea of this algorithm is from the 1940's by McCulloch and Pitts [99]. They proposed a neuron as a switch, thought to loosely mimic the human brain function [120]. Based on input values from other neurons it calculates a weighted sum and is then either activated or not. Later those neurons were also called perceptrons and were proven to be capable of sophisticated pattern recognition, even if some neuron failed [120]. Nevertheless, Minsky and Papert [103] proved that only linearly separable problems could be solved with those perceptrons. Only a few years later these networks of neurons gained the ability to learn non-linear problems from data through the developement of the error-backpropagation algorithm [122] and were first applied for machine reading of texts [127]. Yet, another two decades went by without any noticeable progress because the necessary computational power was not feasible at that time. Today, the interest in neural networks, deep learning and computervision has increased significantly, accelerating the development of new network models and enhancing the training processes.

2.2.1 Perceptrons, Neurons and Feed Forward Networks

Before going to artificial neurons, it is worth while to first understand the function of a so called perceptron developed by Rosenblatt [120]. It takes multiple binary inputs, applies weights, sums those products up and based on a threshold gives a single binary output (Figure 2.3). The threshold and the weights are real valued numbers where the weights represent the importance of single inputs [108].

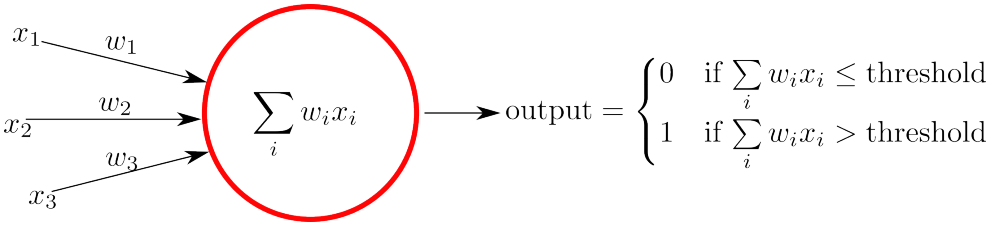

Figure 2.3: Schematic function of a perceptron with three exemplary inputs x_i and respective weights w_i

In other words, the perceptron can be viewed as a decision making tool, that weighs different input conditions and generates outputs as either yes or no. Now to develop from perceptron to artificial neuron the threshold or bias is included in the sum and the hard switch is replaced by an activation function (Figure 2.4). The activation function can basically be any function, yet for multi layered networks, those function must be non linear [4]. Either with perceptrons or neurons, it is possible to build networks by arranging them in layers and connecting those. The easiest way is to just start with the first or input layer, then connect each layer with the following until the last layer or output layer is reached. Every layer in between input and output is called hidden layer. This architecture is a fully connected feed forward neural network (Figure 2.4).

There are other possible architectures, such as recurrent or convolutional neural networks. Recurrent neural networks (RNN) allow also connections to previous layers or to the same layer. Convolutional neural networks (CNN) are specifically designed for two or three dimensional data and work with a kernel matrix that slides along the data grid and performs a matrix multiplication, thus generating a feature map. The convolution layer is typically followed by a pooling layer to extract meaningful representations of the data in lower dimensions. Further information on different network architectures can be found in [4, 52, 57, 108]. Since all networks used in this work are feed forward networks (FNN), only this type will be explained in more detail.

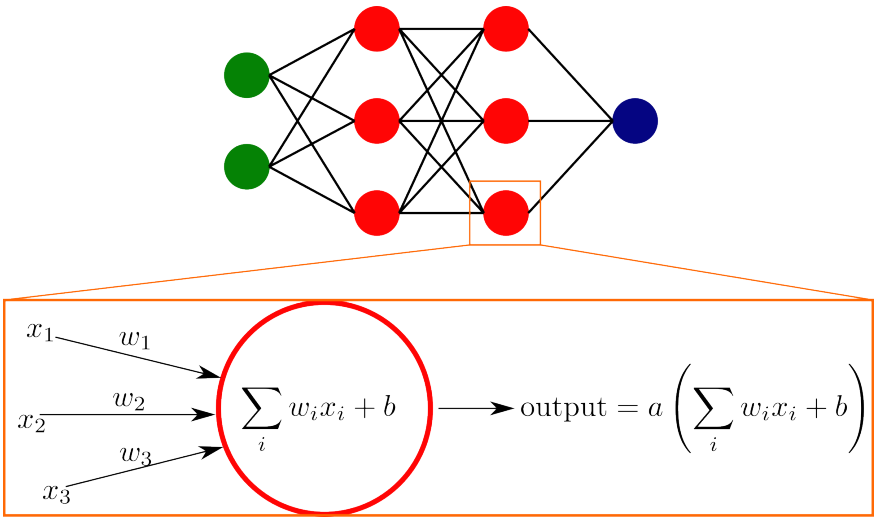

Figure 2.4: Schematic of a feed forward neural network with two hidden layers (red), two input values (green) and one output value (blue). More detailed view of a single neuron with its functionalities; input values x_i, weights w_i, bias b, activation function$a()$

In summary, every neuron calculates a real numbered value and also the input neurons are just real valued numbers. Hence, for any problem that shall be handled by a FNN, a numerical representation of said problem needs to be found and implemented.

2.2.2 Activation functions

As indicated before, neurons calculate a so called activation function after the summation of the inputs, even perceptrons calculate a basic sign function with 0 and 1 as output instead of -1 and 1. The importance of this function becomes obvious if we were just leaving it out. Then our network would just be a large summation of our input variables and would not be able to approximate any function. Honik et al. [66] proved that in theory it is possible to use just one large layer of neuron with a non linear activation function to approximate any complex arbitrary function. Yet, in practical use this would increase the necessary amount of units in a network drastically and would likely be prone to extreme overfitting of the problem [4]. The non-linearity condition imposed on the activation function arises from the fact that a linear activation function would not provide any gain for multiple layers. The multilayer network would become redundant and would not perform any better than linear regression with multiple outputs [3].

A second condition imposed on the activation is its piecewise differentiability due to the training with backpropagation. This method is gradient based and will be explained further in 2.2.3. In theory any function fulfilling those two conditions would work as an activation, but for practical use there is a certain amount of carefully designed activation functions because of their other properties [4]. Four of the most prominent examples are depicted in Figure 2.5.

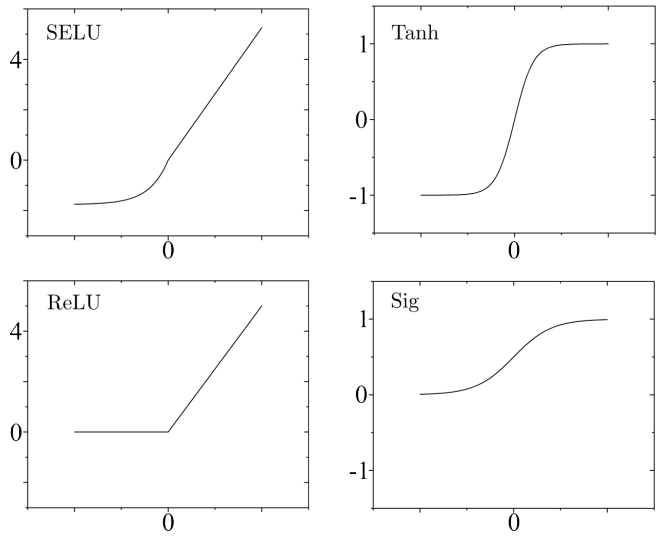

Figure 2.5: Exemplary activation functions: scaled exponential linear unit (SELU), rectified linear unit (ReLU), hyperbolic tangent (Tanh) and sigmoid function (Sig).

The classical activation functions are the sigmoid sig and the hyperbolic tangent $tanh$ functions [4] given by

$$sig(x) = \frac{1}{1 + e^{-x}} \tag{2.6}$$

$$tanh(x) = \frac{e^{2x} - 1}{e^{2x} + 1}. \tag{2.7}$$

The sigmoid function is helpful in creating outputs that can be interpreted as probabilities. The $tanh$ function is similar to the sigmoid, yet is preferred if negative outputs are desired and is easier to train due to its larger gradient around zero. Today however, a number of piecewise linear functions and modifications thereof have become more popular. The rectified linear unit ReLU and the scaled

exponential linear unit SELU in Figure 2.5 are given by

$$\mathrm{ReLU}(x) = \max(0, x) \tag{2.8}$$

$$\mathrm{SELU}(x) = \lambda \begin{cases} x & \text{if } x > 0 \\ \alpha e^x - \alpha & \text{if } x \leq 0 \end{cases}. \tag{2.9}$$

The ReLU function gained popularity since it is much faster to compute than a sigmoid or hyperbolic tangent and in practice works well especially in large neural networks. The SELU function is relatively new and has self normalising properties if $\lambda \approx 1.0507$ and $\alpha \approx 1.6733$ and if the weights are initialised with a variance of $1/n$ [78]. Normalisation is important to combat the exploding or vanishing gradient problem during training, which will be explained in more detail in 2.2.4.

2.2.3 Training with Backpropagation

When talking about training in context of neural networks, the search for the best combination of weights and biases is meant. An error function, sometimes also referred to as loss or cost function, needs to be chosen to evaluate the quality of the approximation. The cost function therefore is a function of all the weights and biases within the network and the goal is to find the minimum of this cost function. Based on that minimisation the weights and biases within the network are updated to work towards a better approximation. This is usually done using the backpropagation algorithm which is based on gradient descent and consists of two steps, the forward pass and the backward pass [4]. In the forward pass the samples of the training data are passed through the network one by one and an output is generated with the current set of weights and biases. The prediction in the output layer is compared to the true target value and its gradient with respect to the output layer is computed. Now, in the backward pass the gradient of the cost function is calculated for each neuron starting from the last hidden layer up to the input layer with respect to the corresponding weights and biases employing the chain rule. These gradients are used to update the respective weights and biases by subtracting a fraction of the gradient from the current value. This fraction is referred to as the learning rate.

The way this works is easiest explained with an example. Let us consider a simple neural network with one input node, then two hidden layers with one neuron each and a single output neuron. Starting with the forward pass, one instance of the training data is passed through the network and the predicted value is compared to the true target via the cost function C. The derivative of

C with respect to the weight w and bias b of the output layer is calculated as

$$\frac{\partial C}{\partial w^{(3)}} = \frac{\partial z^{(3)}}{\partial w^{(3)}} \frac{\partial a^{(3)}}{\partial z^{(3)}} \frac{\partial C}{\partial a^{(3)}} \tag{2.10}$$

$$\frac{\partial C}{\partial b^{(3)}} = \frac{\partial z^{(3)}}{\partial b^{(3)}} \frac{\partial a^{(3)}}{\partial z^{(3)}} \frac{\partial C}{\partial a^{(3)}} \tag{2.11}$$

with

$$z^{(i)} = w^{(i)} a^{(i-1)} + b^{(i)}. \tag{2.12}$$

Here, a is the value of the activation function, also referred to as the activation, z is the value of the weighted sum calculated before the activation function is applied, sometimes called the pre-activation. The upper case indices in brackets indicate the layer number counted from the input layer onwards starting at 0. The derivative of C with respect to the activation of the output layer can directly be calculated from the evaluation of the cost function. The only change is the first partial derivative in the above expressions when changing from weight to bias. The partial derivative of a with respect to the pre-activation is calculated directly from the chosen activation function.

The backward pass then propagates this gradient backwards through the network by calculating the gradient of the cost function with respect to weights and biases of subsequent layers as

$$\frac{\partial C}{\partial w^{(2)}} = \frac{\partial z^{(2)}}{\partial w^{(2)}} \frac{\partial a^{(2)}}{\partial z^{(2)}} \frac{\partial C}{\partial a^{(2)}} \tag{2.13}$$

with

$$\frac{\partial C}{\partial a^{(2)}} = \frac{\partial z^{(3)}}{\partial a^{(2)}} \frac{\partial a^{(3)}}{\partial z^{(3)}} \frac{\partial C}{\partial a^{(3)}}. \tag{2.14}$$

The problem in equation 2.13 is, that there is no possibility to calculate the partial derivative of C with respect to $a^{(2)}$ directly. But as seen in equation 2.14 it is possible to calculate the missing derivative as a function of the later derivative, which is where the idea of propagating backwards comes in. In more general terms, these equations can be written as

$$\frac{\partial C}{\partial w^{(i)}} = \frac{\partial z^{(i)}}{\partial w^{(i)}} \frac{\partial a^{(i)}}{\partial z^{(i)}} \frac{\partial C}{\partial a^{(i)}} \tag{2.15}$$

$$\frac{\partial C}{\partial b^{(i)}} = \frac{\partial z^{(i)}}{\partial b^{(i)}} \frac{\partial a^{(i)}}{\partial z^{(i)}} \frac{\partial C}{\partial a^{(i)}} \tag{2.16}$$

$$\frac{\partial C}{\partial a^{(i-1)}} = \frac{\partial z^{(i)}}{\partial a^{(i-1)}} \frac{\partial a^{(i)}}{\partial z^{(i)}} \frac{\partial C}{\partial a^{(i)}} \tag{2.17}$$

with

$$\frac{\partial z^{(i)}}{\partial w^{(i)}} = a^{(i-1)} \quad \text{and} \quad \frac{\partial z^{(i)}}{\partial b^{(i)}} = 1. \tag{2.18}$$

To transition from single neurons to multiple neurons per layer, only a few more indices need to be introduced. The activation of the j-th neuron in the i-th layer is written as $a_j^{(i)}$ and the activation of the k-th neuron in the previous layer as $a_k^{(i-1)}$. Consequently, the weight connecting both will be written as $w_{jk}^{(i)}$. This changes the equations to

$$z_j^{(i)} = \sum_{k=0}^{n_i-1} w_{jk}^{(i)} a_k^{(i-i)} + b_j, \tag{2.19}$$

$$\frac{\partial C}{\partial w_{jk}^{(i)}} = a_k^{(i-1)} \frac{\partial a_j^{(i)}}{\partial z_j^{(i)}} \frac{\partial C}{\partial a_j^{(i)}} \tag{2.20}$$

and

$$\frac{\partial C}{\partial a_j^{(i)}} = \sum_{j=0}^{n_{i+1}-1} w_{jk}^{(i+1)} \frac{\partial a_j^{(i+1)}}{\partial z_j^{(i+1)}} \frac{\partial C}{\partial a_j^{(i+1)}}. \tag{2.21}$$

n_i is the number of neurons in layer i. As mentioned above the calculation of the respective derivatives for the biases is analogous to the weights. The only major change when having multiple neurons per layer is the summation in equation 2.21 since the activation in one layer influences the activations of multiple neurons in the following layer.

For one sample X_m of the training data all those partial derivatives are calculated and put into the gradient vector ∇C_{X_m}, thus the total gradient vector of the training data ∇C is calculated as the average

$$\nabla C = \frac{1}{m} \sum_{i=1}^{m} \nabla C_{X_i}. \tag{2.22}$$

With the total gradient it would now be possible to update all weights and biases within the network by subtracting a fraction of the respective gradient vector entry from the corresponding weight or bias

$$w_{i,new} = w_{i,old} - \eta \frac{\partial C}{\partial w_i}, \tag{2.23}$$

$$b_{i,new} = b_{i,old} - \eta \frac{\partial C}{\partial b_i} \tag{2.24}$$

with the learning rate η. Yet, for a large amount of training data this would be very time consuming and would require a huge amount of memory to store all gradient vectors. In practice, a stochastic gradient descent (SGD) method is used. The training dataset is divided into mini batches by randomly picking samples from the dataset until every sample is used exactly once (Figure 2.6).

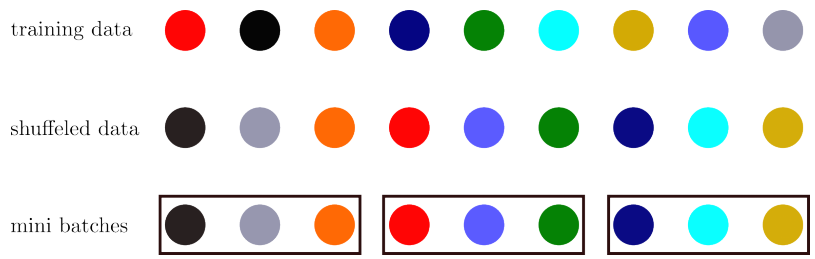

Figure 2.6: Example division of training data into mini batches

Then, each mini batch is processed by the backpropagation algorithm to compute its gradient vector ∇C_x. With the assumption [108]

$$\nabla C_x \approx \nabla C \tag{2.25}$$

the mini batch gives a good estimate for the gradient vector and thus can be used to update the weights and biases. This procedure is repeated until all mini batches are processed once, which is then called one training epoch. At that point, the process is repeated until either the pre-defined number of epochs is reached or a cancellation criterion is fulfilled. If the gradient descent is viewed as stepping down a hill into a valley, the stochastic gradient descent is analogue to taking multiple small steps roughly downhill instead of one large careful chosen step in the steepest direction. Using mini batches also reduces the generalisation error [56].

2.2.4 Issues with Gradient Descent

From equation 2.21 it becomes obvious that the calculation of the gradient is directly linked to the product of weights and the derivatives of the activation function. In networks with many layers this unfolds due to the chain rule into a large product term for neurons in the layers close to the input. So, especially for deep networks this causes instability in the training process, due to either too large updates, called exploding gradients or negligible small updates, called vanishing gradients [4]. To better understand this point let us consider a network with many layers and one neuron per layer. Consider further, that each local derivative is randomly distributed with an expected value of less than one.

Hence, multiplying those values along the path would lead to an exponential decay of the gradient with growing path length. If the expected value of the local derivatives were greater than 1, the gradients would grow exponentially. Even for an expected value equal to 1, the actual distribution could lead to instabilities during training, in other words, for deep neural networks this is a natural problem [4].

Many solutions to exploding or vanishing gradients have been proposed. For example the sigmoid activation function is rather problematic due to its gradient close to 0 especially for highly positive or negative values. Thus, the ReLU function grew more popular because its gradient is always 1 for positive values. But there is also the dying ReLU problem if the arguments are negative which leads to a gradient of 0. Also concepts like an adaptive learning rate and momentum [37, 77, 155] or the relatively new concept of batch normalisation [72] were developed as remedies for the gradient problem.

Another quite popular problem with gradient based methods are saddle points, local minima or flat regions of constant value within the objective function [56]. Empirically, SGD methods seem to escape saddle points rather rapidly though [57]. As for local minima, the cost function of a neural network is usually a high dimensional, non-convex function. Hence, there can be an extremely large up to uncountable infinite number of local minima within a neural networks cost function. But, most of them are of equivalent cost value, which makes being in a local minimum not really a problem since all local minima provide roughly equal solutions [56]. However, they can become an issue if there is one global minimum of significantly smaller cost value than the local minima. Current theories nonetheless state, that for sufficiently large networks it is not necessary to find the true global minimum since there is a local minimum with a low enough cost [34, 57, 123].

2.2.5 The Adam Optimiser

In the previous section, a few remedies or improvements to basic SGD were briefly named. Since the adaptive moment estimation (Adam) optimisation algorithm was used in this work, the important concepts will be explained in more detail below. For mathematical details the reader is referred to the original work of Kingma and Ba [77]. Adam can effectively be seen as a combination of the unpublished RMSprop [138] and momentum.

The concept of momentum [115] is introduced to the gradient descent method to accelerate the learning. In its essence, momentum accumulates an exponentially decaying moving average of past gradients in order to continue moving into their

direction. In practical terms, a new hyperparameter, the momentum factor γ, is introduced and the weight update $\Delta w_{i,t}$ is now given as

$$\Delta w_{i,t} = \eta \frac{\partial C}{\partial w_i} + \gamma \Delta w_{i,t-1}. \tag{2.26}$$

The momentum factor takes a value between 0 and 1, t indicates the number of mini batch training steps. This means a fraction of the weight update from previous mini batch iteration is added to the current weight update with γ mostly being a default value of 0.9 [56]. For Adam now the previously fixed rates η and γ become adaptive, meaning the learning rated for different parameters are computed individually. To this end, Adam uses first and second order moments of the gradient vector. In this context N-th order momentum means the expected value of a random variable to the power of N. So first order would be the mean, second order the uncentered variance.

2.2.6 Parameter Initialisation

The basics of how neural networks function and learn are covered. But the training in its nature is an iterative process and thus it is mandatory to choose a starting point. This parameter initialisation can have a huge impact on generalisation of the model and convergence [56]. The choice of initial point is hence paramount to the success of learning, however there are little to no guidelines on how to find the best initial point. The only certain property of our initialisation is the breaking of symmetry between different units. Meaning, two hidden units with similar activation functions and connections to the same inputs must have different initial parameters. If they were initialised equally, then a deterministic learner applied to a deterministic loss and model would constantly update both units in the same way [56]. Usually, the biases are initialised to heuristically chosen constants and only the weights are randomly drawn from a Gaussian or uniform distribution. For the bias this constant is zero most of the time [4].

The scale of the Gaussian distribution for the weight initialisation is rather important. The weights need to be large enough to transfer information in the beginning yet small enough not to cause the gradients to explode or the activation functions to saturate [56]. For example LeCun et al. [88] proposed a scaling of the distribution according to the number of inputs n to a fully connected layer to a mean of 0 and a variance of $1/n$, which is the necessary initialisation for a SELU activation function. Sometimes this is also normalised to a variance of $1/\sqrt{n}$. For Sigmoid or Tanh activations a normalised initialisation proposed by Glorot and Bengio [54] is often more preferable. They suggested the variance to be chosen as $\sqrt{\frac{6}{m+n}}$, where m is the number of outputs of a fully connected layer.

One major drawback to this kind of initialisation scheme is that the weights become very small for layers with many neurons in them. To counter this effect Martens [96] introduced sparse initialisation where each unit has exactly k non-zero weights. Thereby, the magnitude of the weights is not shrinking with growing number of inputs and outputs. This imposes a very strong prior though and can cause large training times since it takes long to shrink too large weights by SGD. This is especially problematic in maxout units.

2.2.7 Sampling Strategies

Everything discussed above is algorithm specific and the delicate topic of where the data comes from was omitted so far. But the best ML tool cannot learn anything with low quality data. There can be diverse issues, such as irrelevant attributes, missing attributes, redundant attributes, missing values, or noise [81]. Those are all issues with the data quality but are not a concern in this work since all data used here comes from FE simulations. Hence, a complete parametrised representation as well as a complete set of results is available for the specific problem of this work.

Alternatively, the data can have a strong bias, some critical regions in the feature or the solution space can be extremely under represented or there is just not enough data to learn from. These issues however, can certainly occur during the data acquisition of this work and will from now on be referred to as sampling. There are different types of sampling strategies from which three will be discussed in more detail below.

Random Sampling

The strategy is based on the principle of bootstrapping [137] which is a statistical resampling method that approximates inference of a distribution by evaluating some random samples. This means picking a certain number of random choices from the continuous feature space as samples for the training data. In the context of this work it would mean choosing for example 100 different parameter sets at random and perform FE simulations with those parameter sets to acquire 100 training data samples. In any case, a complete random sampling could lead to a strong clustering effect in the feature space or pulling the same sample more than once which in turn would lead to either a strong clustering effect or completely redundant data, respectively. For ML algorithms this would be less than ideal. Hence, some restrictions are necessary, for example one parameter instance may occur exactly once which prevents redundant training samples in the feature space. To further prevent a strong clustering within the feature space, that happens if many points close to each other would be drawn at random, latin

hypercube sampling [100] can be applied. Herein, the range of each sampling variable is subdivided into N equal intervals and then N samples are placed in a way that there is only one sample per partition. In two dimensions this would be a square grid placed over the sampling space and then samples are selected such that only one is in each row and line. This ensures a set of random numbers to be representative for the variability of a sampling space. Nevertheless, one downside of this technique is the primary knowledge of how many samples are necessary since the sub intervals are dependent on that number. For many ML applications and for neural networks especially, this number is unknown most times beforehand.

Adaptive Sampling

All sampling methods based on randomisation only take the feature space into consideration. With the approach of adaptive sampling also the prediction or solution space is considered. In the context of ML algorithms this means iteratively training and evaluating the model performance in order to identify the regions with the most potential information gain. There are two basic approaches towards that. First, the feature space is divided into regions for which test data points are generated to evaluate the predictions. The worst region is identified and more training data is generated there [14]. Second, identification of points with the most gain can be achieved through a surrogate model [94]. This approach is based on the Bayesian global optimisation method [83, 106] which allows to search for extrema in unknown functions. Thus, it can identify data points with maximum information gain through a surrogate model constructed on few initial points. Adaptive sampling in general can reduce the necessary amount of training data drastically because the ML algorithm only learns with data that contains the most information [29]. However, this procedure is only viable if data generation with specific features is easy and works best for computer generated data since there is no real noise [29]. Also a sensible stopping criterion must be implemented in order to not explore the feature space infinitely [94].

2.2.8 k-Fold Cross Validation

As discussed above the training data and its composition is important to discuss when machine learning is used. The easiest way to train and evaluate a ML tool is by splitting all the data just once into train and validation set. Yet, this may not give a representative estimate of the performance and the data composition for training might not be ideal. Thus, the data is being randomly split into k smaller batches of approximately the same size. Then the first batch is used for validation and the remaining k-1 batches for training. Afterwards, the second batch is used for validation and the remaining batches for training and so on

until each of the k batches was used for validation exactly once. This procedure is called k-fold cross validation or just cross validation (CV). When all splits are processed, the performance is averaged and a standard deviation is calculated. Due to this, CV provides a more stable performance measure and more information about the models variance [61, 62, 82].

CV can further be a valuable tool when dealing with scarcely available data. A reasonable estimate of the overall performance without a separate test set is possible since the risk of overfitting is reduced by validating with data not present in the current training set and averaging in the end over multiple trained ML tools while making use of the whole dataset. This makes CV a useful tool when dealing with scarce data, though it generally should only be used to enhance performance measures and the split into training, validation and test set, if possible, is always preferable [62, 82].

2.2.9 Recent Advancements in Material Science

The concept of machine learning can be employed on almost any kind of data. Also in material science it is used often for segmentation of microscopy or tomography images. Durmaz et al. [39] for example applied a U-net structure to find lath-bainite in complex phase steel. Neural networks are also applied as enhancements for constitutive models [95, 128]. Other successful applications include finding new materials [76], speed up optimisation processes [21], model material damage and predicting defects [1, 45]. Also as a design help for composite materials [2], convolutional neural networks are in use. A relatively new approach is to incorporate partial differential equations in the learning process of neural networks [119]. This advancement is able to learn not only based on some error function but to actually respect laws of physics and thereby gains better extrapolation properties.

For most cases in material science the scarcity of data is a major issue since simulations with classical methods are very time consuming or experiments expansive. Therefore, those networks are mostly designed either to speed up classical methods or to completely replace them. Yet, working with scarce data poses other issues since most ML algorithms and especially neural networks usually need large amounts of data to produce reasonable performance.

2.3 Topology Optimisation

When talking about materials design, topology optimisation is also important to discuss. This topic deals with finding an optimal structure under certain boundary conditions, for example finding the stiffest structure with a volume ratio of 0.3 under compressive loading. In combination with FE simulations, there are different, iterative approaches to go from solid material to the optimised, porous structure. The first one deletes elements at less stressed areas and adds elements in highly stressed areas and is called bidirectional evolutionary structural optimisation (BESO) [118]. Another possibility is the solid isotropic microstructures with penalization (SIMP) [121] method in which each finite element is assigned a density function ranging from 0 to 1. Over the course of the iterations this density function is adapted in less stressed areas to 0, meaning no material and in highly stressed areas to 1, meaning full material. A third method is called level-set [10, 11] and uses shape derivatives for the development of optimal design.

All the above methods usually start with an area of full material and develop some porous structure for the design task. If the porous structure is already known or fixed and just should be optimised for a certain task, there is the possibility to employ a parametrised approach. This means finding sensible geometry parameters to describe the structure and finding optimal values for those parameters [19, 21]. Usually a surrogate model technique is applied to describe the relation between design target variables and geometry parameters. Then, the minimum of the surrogate function is determined to take a step towards optimised geometry parameters, which are then simulated for example to determine the resulting design target variables. The surrogate function is adapted to the new datapoint and minimised again. This procedure is repeated until a cancellation criterion is met.

For the minimisation of the surrogate function Newton's method or different quasi Newton procedures are feasible. Within this work a type of quasi Newton minimiser originally developed by Broyden [23], Fletscher [47], Goldfarb [55] and Shanno [129] (BFGS) is used. For all quasi Newton procedures, just the gradient of the objective function is necessary to calculate and the Hessian is only approximated. A brief overview how the BFGS algorithm works is given below and explained in more detail in [109].

Let us begin with a squared model m which can be viewed as a Taylor expansion of the scalar objective function f that is given for the iteration step k as

$$m_k(\mathbf{p}) = f_k + \nabla f_k^T \mathbf{p} + \frac{1}{2}\mathbf{p}^T \mathbf{B}_k \mathbf{p}. \tag{2.27}$$

Here, ∇f_k^T is the gradient of the objective function, $\mathbf{B}$ is a symmetric, positive definite $n \times n$ matrix which is updated within every iteration step and can be identified as the Hessian approximation. The search direction $\mathbf{p}$ for the next iteration step of the convex, quadratic model can be written as

$$\mathbf{p}_k = -\mathbf{B}_k^{-1} \nabla f_k. \tag{2.28}$$

Combined with the step size α, the location vector for the next iteration is calculated as

$$\mathbf{x}_{k+1} = \mathbf{x}_k + \alpha_k \mathbf{p}_k \tag{2.29}$$

and α_k is chosen to satisfy the Wolfe condition (equation 2.30).

$$f(\mathbf{x}_k + \alpha_k \mathbf{p}_k) \leq f(\mathbf{x}_k) + c_1 \nabla f_k^T \mathbf{p}_k, \tag{2.30a}$$

$$\nabla f(\mathbf{x}_k + \alpha_k \mathbf{p}_k)^T \mathbf{p}_k \geq c_2 \nabla f_k^T \mathbf{p}_k, \tag{2.30b}$$

with the constants c chosen to fulfil $0 < c_1 < c_2 < 1$ this condition is used as step size control and ensures the degradation of the objective function values. Typical values for the constants are $c_1 = 10^{-4}$ and $c_2 = 0.9$. In order to include the curvature from the previous step, $\mathbf{B}$ is updated. Therefore, a new model for step $k+1$ is constructed as

$$m_{k+1}(\mathbf{p}) = f_{k+1} + \nabla f_{k+1}^T \mathbf{p} + \frac{1}{2}\mathbf{p}^T \mathbf{B}_{k+1} \mathbf{p}. \tag{2.31}$$

A requirement for $\mathbf{B}_{k+1}$ to carry over the knowledge from the last step, is that the gradient of m_{k+1} and the gradient of the objective function f for the current step k and the next step $k+1$ match. Since $\nabla m_{k+1}(0)$ is exactly ∇f_{k+1} and is thus automatically fulfilled, only the following condition must be met

$$\nabla m_{k+1}(-\alpha_k \mathbf{p}_k) = \nabla f_{k+1} - \alpha_k \mathbf{B}_{k+1} \mathbf{p}_k = \nabla f_k \tag{2.32}$$

$$\Leftrightarrow \quad \mathbf{B}_{k+1} \alpha_k \mathbf{p}_k = \nabla f_{k+1} - \nabla f_k \tag{2.33}$$

For simplicity the vectors

$$\mathbf{s}_k = \mathbf{x}_{k+1} - \mathbf{x}_k = \alpha_k \mathbf{p}_k, \qquad \mathbf{y}_k = \nabla f_{k+1} - \nabla f_k, \tag{2.34}$$

$$\mathbf{B}_{k+1} \mathbf{s}_k = \mathbf{y}_k \tag{2.35}$$

are defined and equation 2.35 has a guaranteed solution if

$$\mathbf{s}_k^T \mathbf{y}_k > 0 \tag{2.36}$$

which is enforced by the Wolfe condition (equation 2.30). With the definition of the Hessian $\mathbf{H}$ as

$$\mathbf{H}_k = \mathbf{B}_k^{-1} \tag{2.37}$$

we obtain

$$\mathbf{H}_{k+1} \mathbf{y}_k = \mathbf{s}_k. \tag{2.38}$$

This equation is also solvable under the condition from equation 2.36 and has an infinite number of solutions. Hence, to determine a single solution a further condition is imposed on $\mathbf{H}_k$,

$$\min_{\mathbf{H}} \|\mathbf{H} - \mathbf{H}_k\| \tag{2.39}$$

where $\mathbf{H}$ is the analytical Hessian. To solve this problem, various matrix norms can be used, each of which forms the basis of its own quasi Newton method. For the BFGS method the weighted Frobenius norm is used. This results in,

$$\mathbf{H}_{k+1} = (\mathbf{I} - \mathbf{b}_k \mathbf{s}_k \mathbf{y}_k^T) \mathbf{H}_k (\mathbf{I} - \mathbf{b}_k \mathbf{y}_k \mathbf{s}_k^T) + \mathbf{b}_k \mathbf{s}_k \mathbf{s}_k^T, \tag{2.40}$$

with identity matrix $\mathbf{I}$ and

$$\mathbf{b}_k = \frac{1}{\mathbf{y}_k^T \mathbf{s}_k} \tag{2.41}$$

for the updates of the Hessian. Summarising, the BFGS method stepwise is:

- Calculate search direction $\mathbf{p}_k = -\mathbf{H}_k \nabla f_k$
- Calculate step size α_k to satisfy the Wolfe condition (Equation 2.30)
- Calculate location vector $\mathbf{x}_{k+1} = \mathbf{x}_k + \alpha_k \mathbf{p}_k$
- Calculate $\mathbf{s}_k$ and $\mathbf{y}_k$ (Equation 2.34)
- Update $\mathbf{H}_{k+1}$ (Equation 2.40)

These steps are repeated until some convergence criterion is fulfilled. The further development of the BFGS method into the Limited BFGS for Bound Constrained Routine (L-BFGS-B) by Byrd et al. [25] introduces the possibility of specifying bounds and constraints for the parameters to be minimised. Furthermore, this extension reduces the computing time and the required memory capacity is significantly reduced.

2.4 Selective Laser Melting

Additive manufacturing (AM) is a technology on the rise in recent years. From metals over polymers to ceramics, AM is popular in many fields of materials and production and thus there exist many different methods [145]. They all have in common the basic working principle, first a 3D model of the final product needs to be obtained either by computer aided design (CAD) or 3D reconstruction of images for example. Second, the surface of the structure is approximated by triangles thus creating a surface mesh resulting in an STL (surface tessellation language) file. Last, this STL file is sliced into 2D images so that the printer can build up the product layer by layer [142]. One possibility for AM in the field of metals is selective laser melting (SLM) developed in 1998 [101] as a powder bed fusion technology. A laser melts and thereby fuses together selected regions of a metal powder bed to create the final product. In the beginning, a thin layer of metal powder is put on a substrate plate for the first layer. The substrate plate is lowered and new metal powder is layed on top for the next layer of the product. Common layer resolution ranges between 20 µm and 100 µm with the usually used metal powders for SLM nickel, iron and titanium [152]. Aluminium, as used within this work, has significantly fewer publications and the most commonly used alloy in SLM is AlSi10Mg [152]. The resolution is strongly dependent on the powder size and balanced within this region. Too small particles tend to agglomerate due to van der Waals forces, while too large particles result in poor build tolerance and resolution [30]. The fusion process is most times performed under nitrogen or argon gas atmosphere to protect the heated metal from oxidation.

The laser system for SLM progressed from CO_2 (wavelength $\approx$ 10.6 µm)to Nd:YAG lasers with a wavelength of $\approx$ 1.06 µm since most metals have a better absorptance in this region of the infrared spectrum [152]. Also Yb:YAG fiber lasers are of increasing interest due to a higher absorption bandwidth to reduce thermal management requirements for diode lasers, a lower thermal loading per unit pump power and a longer upper-state lifetime [152]. For detailed information on laser sources and working principle the reader is referred to [40].

Apart from the laser medium and the powder there are other important process parameters such as the layer thickness, the hatch spacing or the scanning speed just to name the major ones (Figure 2.7). All those parameters combined with the absorptance of the powder give the volumetric energy density. The heat capacity and latent heat are heavily dependent on the material and need to taken into account when melting occurs. Hence, balling can happen if there is insufficient energy due to a lack of wetting of the melt with the previous layer [90]. If the laser power is too high or the scanning speed too slow evaporation

of the powder material can arise [80]. This can lead to condensation of material particles on the laser window and thus disrupt the beam. In addition, a poor hatching space can be responsible for a high porosity since adjacent melts do not fuse together [32].

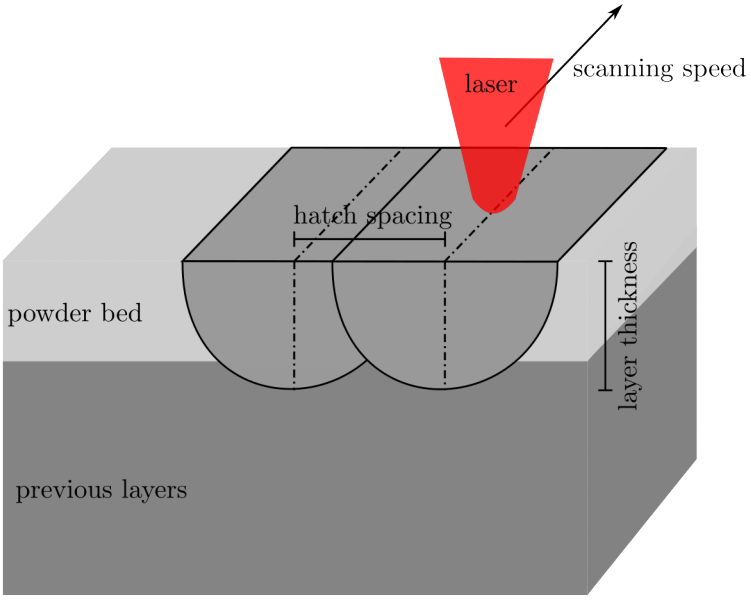

Figure 2.7: Schematic of the SLM process with process parameters.

However, for the purpose of this work, SLM was only used to manufacture specimens to validate the simulation results. Hence, there was no deeper investigation of the SLM process itself. Therefore, the reader is referred to the literature for deeper insight into SLM and its challenges [67, 116, 147, 152].

2.5 Metamaterials

Most materials display properties within certain limitations [154] which are also most often linked by some power law[53]. For applications, the design space of natural materials is therefore limited and it is desirable to develope materials with arbitrary properties. Metamaterials are constructed to overcome the boundaries in materials design and give a higher tailoring potential for applications.

Initially, the term metamaterials was linked to optics and electromagnetism [93], e.g. for materials with a negative refractive index. Within the last few years however, the term mechanical metamaterials has emerged [154] and gained interest, even though some basic concepts of those materials are already known for some decades. This class utilises a hierarchical architecture with effects on the meso-, mikro- or nanoscale [135], thus it is mostly porous structures. Thereby, a superior mechanical performance can be achieved and gives rise to many multifunctional applications. There is no clear definition of the term metamaterial up to now [75] but most would agree on the somewhat loose definition: "metamaterials are rationally designed composites made of tailored building blocks that are composed of one or more constituent bulk materials. The metamaterial properties go beyond those of the ingredient materials, qualitatively or quantitatively." [75].

A basic classification of existing mechanical metamaterials can be found in [153] and is depicted in Figure 2.8. The classification is according to the respective effect area, whereas an assignment to more than one area is also possible, e.g. chiral/anti-chiral structures. The subdivision is based on the three elastic constants Young's modulus, shear modulus and bulk modulus as well as on the Poisson's ratio, which classifies mechanical metamaterials according to their fundamental mechanics rather than their material class. The class Young's modulus describes materials which are either light and strong or have a tunable stiffness. The materials in the group of shear/bulk modulus share the main characteristic of being rather hard to compress yet easy to shear since the shear modulus approaches zero or the compressibility is even negative. The last group, Poisson's ratio, gathers materials with a negative to zero or a switchable Poisson's ratio also called auxetics. Within this work, two types of mechanical metamaterials, auxetics and pentamode structures were investigated and are explained in more detail below.

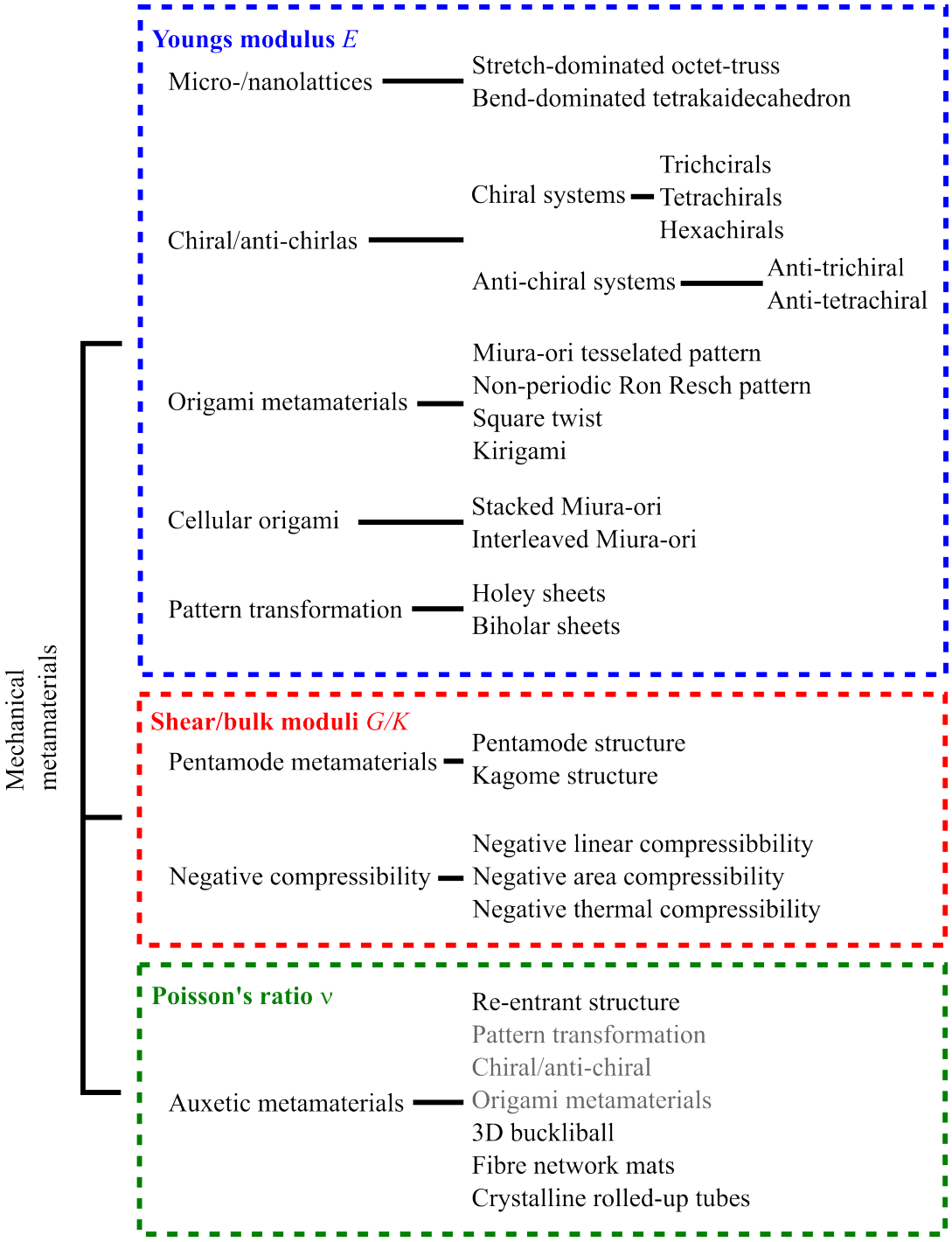

Figure 2.8: Possible classification of mechanical metamaterials according to their effects (adapted from Yu et al. [153])

2.5.1 Auxetic Structures

These type of structures have the governing property of a negative Poisson's ratio, which means they expand perpendicular to a loading direction [85]. Their name is derived from greek auxetikos which means 'that which tends to increase'[43]. The Poisson's ratio ν of a structure is defined as

$$\nu = -\frac{\varepsilon_\perp}{\varepsilon_\parallel}, \tag{2.42}$$

where $\varepsilon_\perp$ is the strain perpendicular to an uniaxial loading direction and $\varepsilon_\parallel$ is the strain parallel to the loading direction. It can also be expressed through other elastic constants such as Young's modulus E, bulk modulus K and shear modulus G, which are interdependent as [151]

$$G = \frac{E}{2(1+\nu)}, \tag{2.43}$$

$$K = \frac{E}{3(1-2\nu)}, \tag{2.44}$$

$$E = \frac{9KG}{3K+G}, \tag{2.45}$$

$$\nu = \frac{3K-2G}{2(3K+2G)}. \tag{2.46}$$

For isotropic material behaviour there are theoretical limits for the Poisson's ratio of -1 and 0.5. The upper limit is a result of the assumption of constant volume, the lower limit results from the positive definition of E and G [28]. This however only holds if the material at hand is isotropic and the loading is in the elastic regime of the stress-strain behaviour. A further implication for the measurement of the Poisson's ratio is that the experiment should be uniaxial. For anisotropic materials these theoretical limits do not hold, for example for some polymers, negative Poisson's ratios up to -6 were reported [8].

With the negative Poisson's ration certain properties can be enhanced such as thermal shock resistance [91], fracture toughness [17, 86] and indentation resistance [9, 84, 87]. This can be attributed partly to the higher shear modulus with a negative Poisson's ratio since [28]

$$\frac{G}{E} = \frac{1}{2(1+\nu)} \tag{2.47}$$

is given and with a constant E the shear modulus is increased with lower values of ν. How auxetics work through their microstructure is easiest explained in 2D. Figure 2.9 depicts three possible micromechanisms, the re-entrant honeycomb structure (Figure 2.9 a)) [12], the double arrowhead (Figure 2.9 b)) [150] and the

rotating rigid bodies (Figure 2.9 c)) [60]. There are also chiral lattice structures which display auxetic behaviour [38, 105, 148, 146]. For more unit cells and a deper mathematical background the reader is referred to [68, 124].

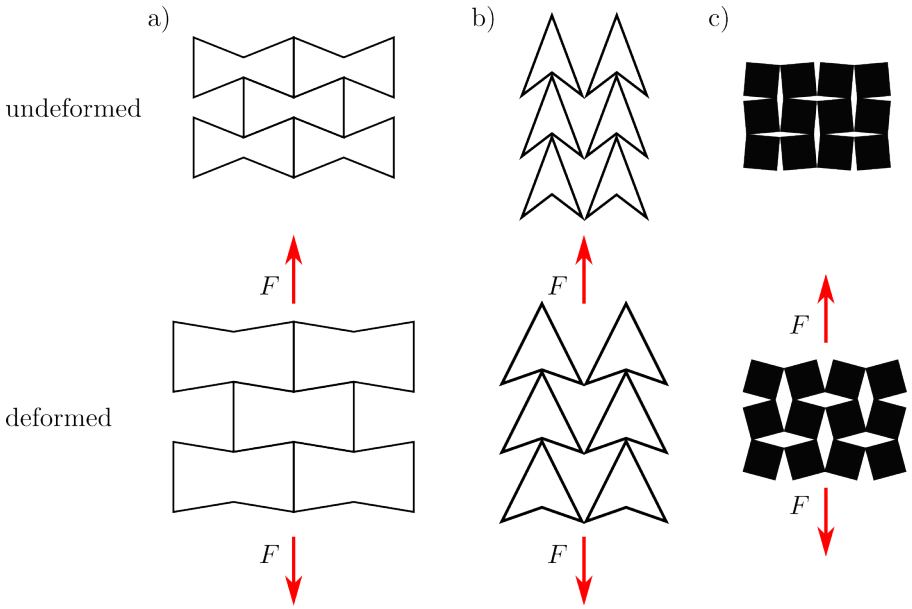

Figure 2.9: 2D working principle of auxetic structures a) re-entrant honeycomb, b) double arrowhead, c) rotating rigid bodies

There are several ways to proceed from the 2D to 3D unit cells, the most simplistic being to just extrude the 2D structure in the third dimension. For the re-entrant honeycomb it is possible to interlock the 2D structure in different directions [143]. Structures created in this way, however, only show auxetic behaviour when loaded perpendicular to the assembly plane. Furthermore, the behaviour of the 3D structure cannot be modelled from the 2D model [42]. In order to generate an auxetic behaviour in all three spatial directions, the idealised model of the imprinted polyhedron presented by Lakes [84] can be used. Here, a 24-sided polyhedron is imprinted inwards at all connecting struts, which is what happened in the case of the PU foam treated by Lakes [84]. Another construction method is beam based in combination with an eigenmode analysis [79]. Here, differently shaped struts are connected at nodal positions, which is usable for 2D and 3D applications and can even provide novel unit cell geometries.

All those property enhancements make auxetics suitable for many applications to replace the existing solutions. For example in crash absorber [16, 125] or as ballsistic blast protection [71, 110, 111]. Also to save resources, a lightweight approach through truss structures [104], hybrid materials [19] or optimised design

[20, 21, 22] is of importance. Also within composites either through auxetic fibres increasing the pull-out resistance [7], or a suitable stacking sequence of the fibre layers [31, 65] thereby increasing impact resistance and having a more localised initial damage [6], auxetics can be applied. Further applications are stents and arterial prosthesis [26] or sport-protective equipment [48].

The first artificially created auxetic material was a polyurethane (PU) foam in 1987 by Lakes [84]. It utilized the re-entrant honeycomb mechanism and was manufactured from a conventional PU foam through heating above the softening temperature and triaxial compression. His investigation marked the starting point of the research into the tailoring potential of auxetics even down to a molecular level [43]. However, the auxetic effect is not exclusively reserved for designed metamaterials. Also in nature there are many examples for materials with a negative Poisson's ratio such as some forms of animal skin [49, 89, 141] or different cubic crystal lattices [58].

Recently, multiple investigations of auxetics under dynamic loading were performed [19, 46, 98, 112], since applications as crash absorbers or blast protection are of interest for the auxetic structures with their superior energy absorption capacity over conventional metal foams [19]. In addition, a modified auxetic unit cell with a half strut in their mid was proposed by Bronder et al. [20] to further increase the energy absorption capacity over normal 3D re-entrant honeycomb structures. Moreover, auxetic materials can be applied to enhance stretchable strain sensors. Jiang et al [73] were able to design a piezoresistive sensor which could stretch up to 98 % and was used to detect the radial artery pule of a human. Wong et al [144] designed and 3D printed an ionogel strain sensor superior to conventional strain sensors, which was able to extend roughly three times as much.

2.5.2 Pentamode Structures

A different class of metamaterials called pentamode materials is a part wise result of the question which elasticity tensors are realisable [102] and the endeavour to tailor materials with prescribed elasticity tensors through a combination of beams [131]. The elasticity tensor $\mathbf{C}$ is a fourth order tensor with 81 components, which can be reduced to 21 independent constants for completely anisotrop materials [13] and it is used to calculate the stress tensor σ from the corresponding strain

tensor ε. The Voigt notation gives it as a matrix vector product

$$\begin{bmatrix} \sigma_{11} \\ \sigma_{22} \\ \sigma_{33} \\ \sigma_{23} \\ \sigma_{13} \\ \sigma_{12} \end{bmatrix} = \begin{bmatrix} C_{11} & C_{12} & C_{13} & C_{14} & C_{15} & C_{16} \\ C_{21} & C_{22} & C_{23} & C_{24} & C_{25} & C_{26} \\ C_{31} & C_{32} & C_{33} & C_{34} & C_{35} & C_{36} \\ C_{41} & C_{42} & C_{43} & C_{44} & C_{45} & C_{46} \\ C_{51} & C_{52} & C_{53} & C_{54} & C_{55} & C_{56} \\ C_{61} & C_{62} & C_{63} & C_{64} & C_{65} & C_{66} \end{bmatrix} \begin{bmatrix} \varepsilon_{11} \\ \varepsilon_{22} \\ \varepsilon_{33} \\ 2\varepsilon_{23} \\ 2\varepsilon_{13} \\ 2\varepsilon_{12} \end{bmatrix}. \tag{2.48}$$

Hence, the elasticity tensor can be represented as a 6×6 matrix, for which eigenvalues can be calculated. In the special case of pentamode materials, five out of the six eigenvalues are equal to zero, where the name pentamode is derived from. Therefore, those materials are ideally incompressible but non resistant to shear deformation and that is why they are also referred to as metafluids since they show similar behaviour. Milton et al. [102] proved that every elasticity tensor is realisable with a composite material with a rigid and non rigid phase. For pentamodes they also proposed the diamond lattice structure out of four biconical beams (Figure 2.10).

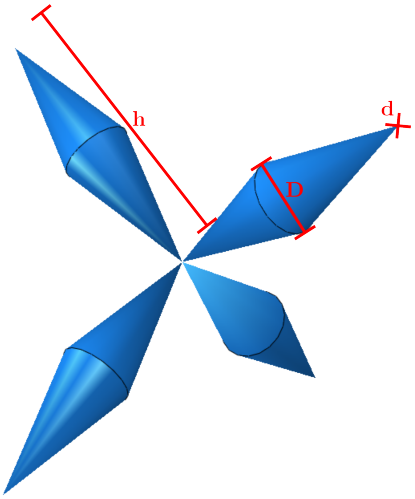

Figure 2.10: Idealised pentamode unit cell with the three geometry parameters h, D and d

In the modern literature this is the only pentamode structure investigated and the beam based variants by Sigmund [131] are neglected. The first produced pentamode structure however, was in 2012 by Kadic et al. [74] with stereolithography since AM technologies were not enough developed in 1995. They identified three geometry parameters (Figure 2.10) that influence the behaviour. Ideally, the pentamode structures would have a finite bulk modulus k and a shear

modulus G equal to zero, which is not feasible because the connecting dots between the bicones would have to be infinitely small and the material would flow away immediately [74]. Nevertheless, it was possible to manufacture structures with a K/G ratio of over 10^3. An ideal pentamode material would also have a Poisson's ratio of 0.5 (Equation 2.46 for $G = 0$).

Since the first production, a few investigations into the experimental and numerical study of pentamode materials haven been launched. Either produced by SLM out of a metal alloys [63] or by 3D printing for polymers [126], the main concern here is on the one hand the producibility and on the other hand the stability under compression. Schittny et al. [126] found for small overlap diameters d and large unit cells the K/G ratio to increase significantly but under compressive load, the resistance to deformation is correspondingly lower. Among other things, this can be explained by the smaller amount of material in the area of the point of contact of the struts for small d. Furthermore, it became clear from the observations that the Poisson's ratio is directionally dependent.

A proposed application for pentamode materials is a mechanical cloak [24]. This means that it is possible to use pentamode materials in order to hide objects within in order to make it impossible to feel the objects geometry. In order to achive the cloaking, Bückmann et al. [24] used a rigid, hollow cylinder which was immersed into a pentamode shell produced by direct laser writing and consisted of two different pentamode structures. Similarly, an underwater acoustic cloak was developed to scatter acoustic waves and make elliptical objects underwater undetectable [117]. Moreover, for underwater communications, pentamode metasurfaces are explored to enhance orbital angular momentum multiplexing communication [134]. Apart from acoustics, another possible application is as tunable, seismic isolation devices [44] which were shown to outperform the classical rubber based isolations.

2.6 Design of Experiment

When conducting experiments, either in simulation or reality, it is often worth while to utilise some designed testing plans in order to keep the required number of experiments as small as possible. If it is either one parameter at a time or by statistical means is strongly dependent on the number of parameters, also called factors in the context of this topic [130]. An example for such a design is a full factorial testing plan, which was also employed within this work. Here, each factor is varied one after the other to establish its impact on the result, also called the effect. For three factors this would mean eight necessary experiments, which could be depicted as a cube (Figure 2.11) with the experiments on each corner.

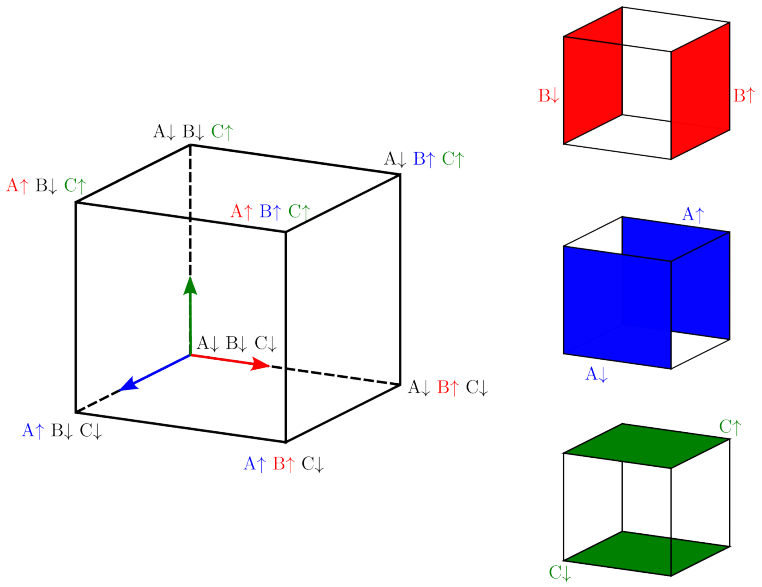

Figure 2.11: Schematics of a full factorial testing plan with factors A,B and C

This implies linear effects for the factors, if they are only varied between a low and a high value, also called levels [130]. The six sides of the cubes thus represent planes of equal level for the respective parameters. Effects are calculated by taking the mean values of the two levels. The slope of the straight line connecting these two mean values gives information about the size of the influence on the effect on the target variable [130]. The full factorial testing plan also offers the possibility of investigating interactions between the effects. For this purpose, the prefactors of the levels are multiplied and then the mean values of the different combinations are calculated [130]. For each interaction plot, two straights result which, with increasing antiparallelism, represent the growing influence of the interaction. The lower level has a prefactor of -1, the higher level a prefactor of 1.

The simple linear model gives an intuitive understanding of an otherwise complex problem and can give helpful insight [51]. It is also possible to use more than two levels and calculate the linear model through interpolation, even though the model is not exact for non-linear problems [130]. Extrapolation beyond the limits of the investigated factors is not permissible, since there could be new physical phenomena [130]. In case of non-linear problems, the level distance could be decreased, so that linearity within a smaller region of the parameter space gives still a good estimate [130].

3

Auxetics

Within this chapter, modified auxetics based on re-entrant honeycomb structures are optimised. The goal is to find a structure capable of absorbing as much energy as possible while having a negative as possible Poisson's ratio and a low as possible mass. The modification consists of a supplemented half strut in the center of the unit cell (Figure 3.1). In addition, there are five geometry parameters chosen to describe the unit cell completely.

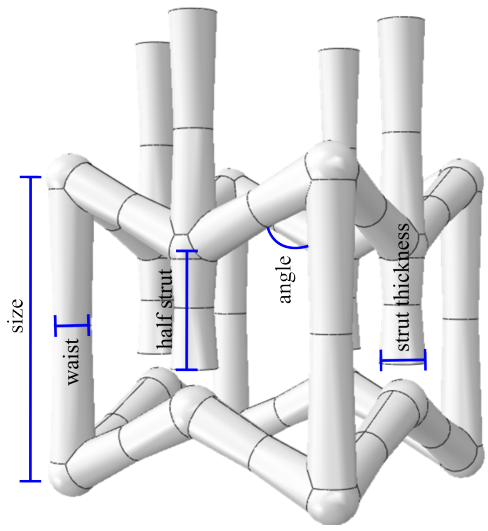

Figure 3.1: Modified auxetic unit cell with five identified geometry parameters for optimisation purposes

The half strut enhances the energy absorption capacity under compression (Figure 3.2). Due to reaching contact with the rest of the structure after a certain deformation, the structure is capable of undergoing higher compressive stresses compared to a structure without the supplemented half strut. It also maintains its stiffness for larger deformations.

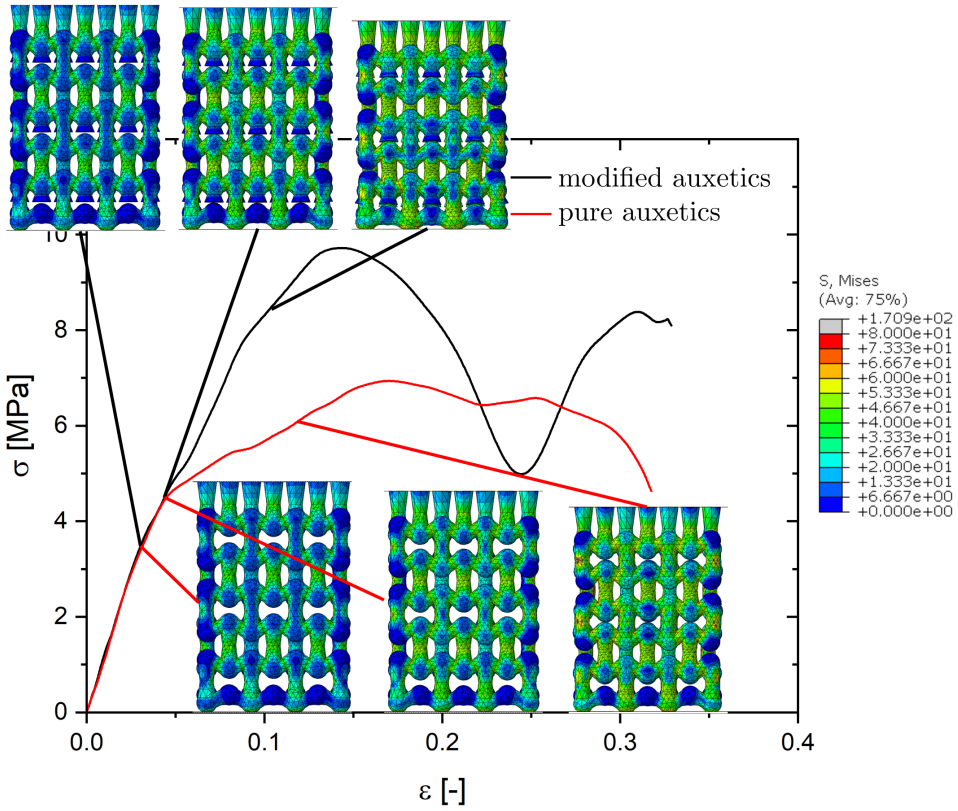

Figure 3.2: Stress-strain diagrams of two comparable auxetic unit cells; one with an additional halfstrut (modified) and one without (pure); the modified version reaches higher stress values due to contact at a certain point (Bronder et al [20])

In the following sections, the procedure of optimising the structure is described. First, a study concerning the representative volume element (RVE) was conducted, then the FE simulations are described to generate a training database. Afterwards, a full factorial testing plan was used to gain general insight into the relations of the geometry parameters to the target values. The next section describes the applied neural networks and the optimisation of the structure and the last sections concern is the experimental validation of the optimised structure.

3.1 Size Effect

In order to derive the macro behaviour from simulations of the microstructure, the question arises: What is the smallest amount of unit cells, that have to be considered? To find such an RVE seven different specimen types (Figure 3.3) of the modified auxetics were produced by the institute of production engineering, Saarland University of Prof. Bähre with an SLM® 125 machine (SLM Solutions Group AG, Lübeck, Germany). All specimens were manufactured out of AlSi10Mg metal powder (SLM Solutions Group AG, Lübeck, Germany) under argon atmosphere, subjected to a heat treatment at 300 °C for 2 hours and cooled naturally. The other process parameters are listed in Table 3.1. From 2×2 to 6×6 unit cells base area with a height of 3 unit cells were produced. In addition, for the 3×3 base area, specimens with a height of 2 and 4 unit cells respectively were fabricated.

Table 3.1: Process parameters for the SLM manufacturing process; "total fill" means a circular fill pattern for the slices.

process parameter [unit]	value
laser wave length [nm]	1064
laser Power [W]	250
scan speed [mm s^{-1}]	2000
layer thickness [μm]	30
laser hatch distance [mm]	0.114
scanning strategy:	"total fill"

All specimens were investigated under uniaxial compressive loading on the universal testing machine ElectroPuls E10000 (Ltd. Instron, Pfungstand, Germany) and a speckle pattern was applied to evaluate the experiments with digital image correlation (DIC). The experiments were quasi-static with a strain rate of $0.003\,s^{-1}$. For the purpose of DIC, every experiment was observed with a 9 megapixels CCD (charged coupled device) camera (Manta G-917B, Allied Visions Technologies GmbH, Puchheim, Germany) and the software ISTERA4D® (Dantec Dynamics, Skovlunde, Denmark) was utilised. The trigger for image acquisition was linked to the testing machine so as to take one image every 0.5 % strain.

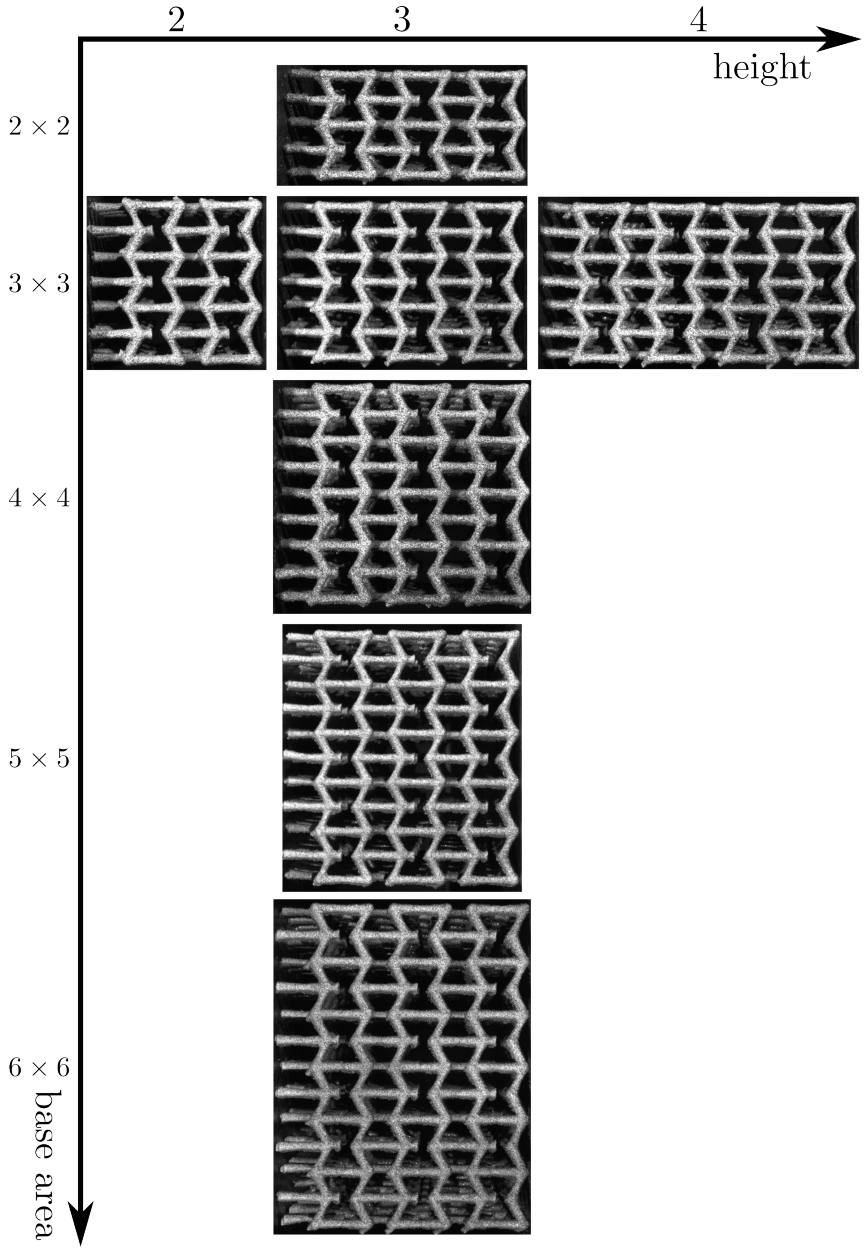

Figure 3.3: Seven different types of specimens for the RVE study; speckle pattern applied for DIC measurements

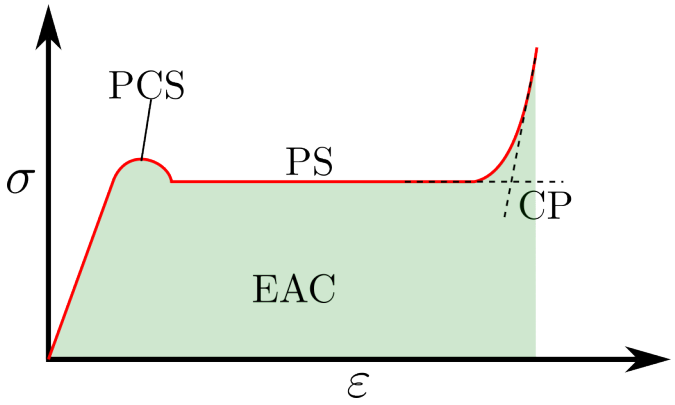

Figure 3.4: Schematic of a stress-strain diagram typical for open porous structures with commonly used terms: plastic collapse stress (PCS), plateau stress (PS), compation point (CP) and energy absorption capacity (EAC) marked as green area.

A typical resulting stress-strain diagram for compression is depicted in Figure 3.4 with the commonly used terms. It is similar for foams and other porous materials. There is a pseudo elastic regime before the plastic collapse point, which can be identified as an initial stiffness. The regime of constant stress after the collapse of the first porous layer is called the plateau phase, which is followed by the compaction when all layers are collapsed and the structure is essentially bulk material. The area under the stress-strain diagram is identified as the energy absorption capacity (EAC) or in case of mass normalised stresses as a mass specific EAC.

Each type of specimen was produced thrice, so the stress-strain diagrams (Figure 3.5) are mean values of three experiments. For all specimens, there is no significant change for plastic collapse stress (PCS), plateau stress (PS) (Figure 3.6) or stiffness before PCS. Most curiously, the PCS is lowest for the 6×6 specimens and highest for the 2×2 specimens with a difference of 1.5 MPa. Yet, all stress-strain diagrams are within the scatter range of the single experiments, thus leading to the conclusion that 3 unit cells in every direction is sufficient for the simulation. The PCS might get overestimated but only within a small margin of error. Also for the PS, the $3 \times 3 \times 3$ can be regarded as the RVE. In addition, everything larger only extends the simulation time significantly without much further information gain. According to the size effect experiments, smaller volumes might also be possible, but then no unit cell would be within the volume, which could eventually lead to too many surface effects and a slight overestimation of the stress-strain behaviour.

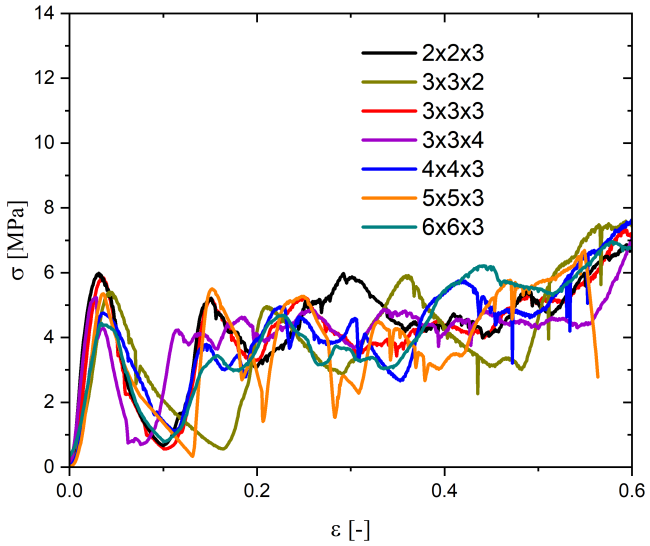

Figure 3.5: Mean stress-strain diagrams of three specimens each for the respective size effect experiments.

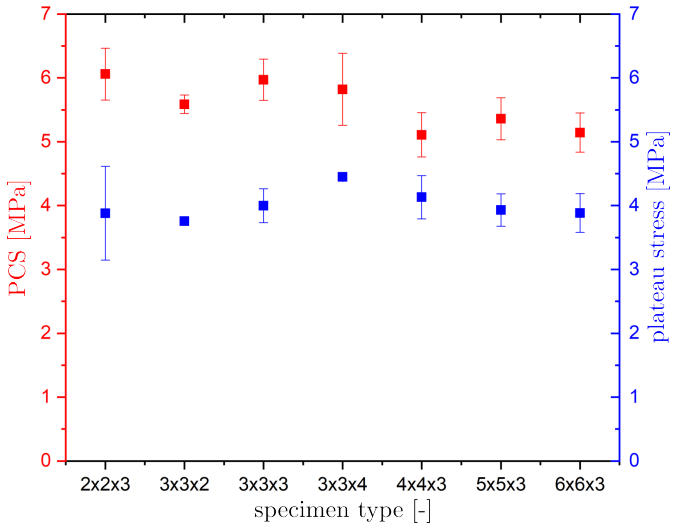

Figure 3.6: Resulting mean plastic collapse stress (PCS) and plateau stress for the size effect experiments; the small deviations within the error regime confirm the choice of the RVE

3.2 FE Simulations

Since the size effect experiments resulted in an RVE with $3 \times 3 \times 3$ unit cells, the simulations were set up accordingly. The compression test was simulated using displacement controlled rigid bodies, similar to the experimental setup (Figure 3.7). The lower plate acted as a force sensor fixed in space, while the upper plate was responsible for the deformation. The contact between plates and specimen was simulated as coulomb friction with a 0.1 friction penalty coefficient through ABAQUS® general contact, which enforces the contact constraints by detecting node-into-face and edge-into-edge penetrations with a pure master-slave procedure.

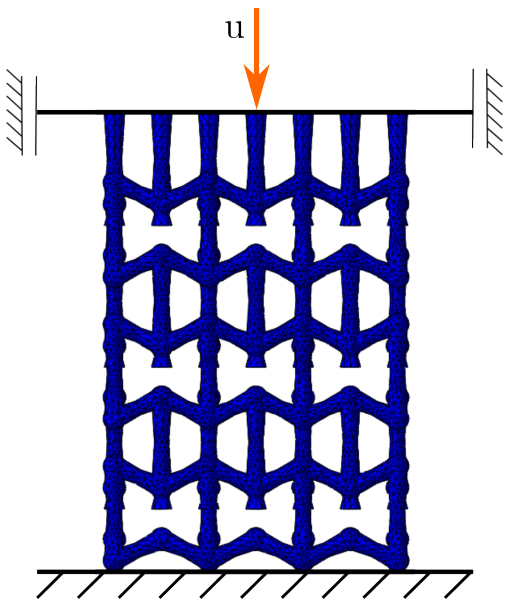

Figure 3.7: Setup of the simulations for the compression experiments of the modified auxetics.

Due to the complex geometry, the model was meshed with quadratic, tetrahedral C3D10M elements. The M here marks a modification of the classical tetrahedral element, meaning three additional displacement variables [33]. This makes those elements more accurate for contact simulations especially when using the explicit solver, which was employed for all simulations. The model was built by multiplying the parametrised unit cell (Figure 3.1) three times in all spatial directions. Thus, after the simulation is finished, the set of geometry parameters is linked to a mass specific stress-strain behaviour and a Poisson's ratio, which are the two optimisation targets. In order to save computational time, all simulations were done until 0.33 compressive strain, which is well after the PCS and within the

PS. The plateau is approximated as almost constant, so 0.33 strain gives a good estimate of the plateau and only neglects the compaction phase.

In order to calibrate the elasto-plastic material model for the simulations, tensile tests on dog-bone specimens according to DIN EN ISO 6892-1 [36] were performed. The experimental setup is essentially the same as for the size effect specimens. For comparability, these specimens were also manufactured with SLM by the institute of production engineering of Prof. Bähre, yet initially with different production parameters. This will later lead to discrepancies between simulations and experiments. Therefore, new tensile specimens were produced with the same manufacturing parameters as the modified auxetic specimens (Figure 3.8). The corrected material model though was only used for the validation simulation of the optimised structure, since all other simulations for the network training were already done. Even though error prone, the optimisation can still be regarded as valid because the error in all training data is the same, which still gives good qualitative results.

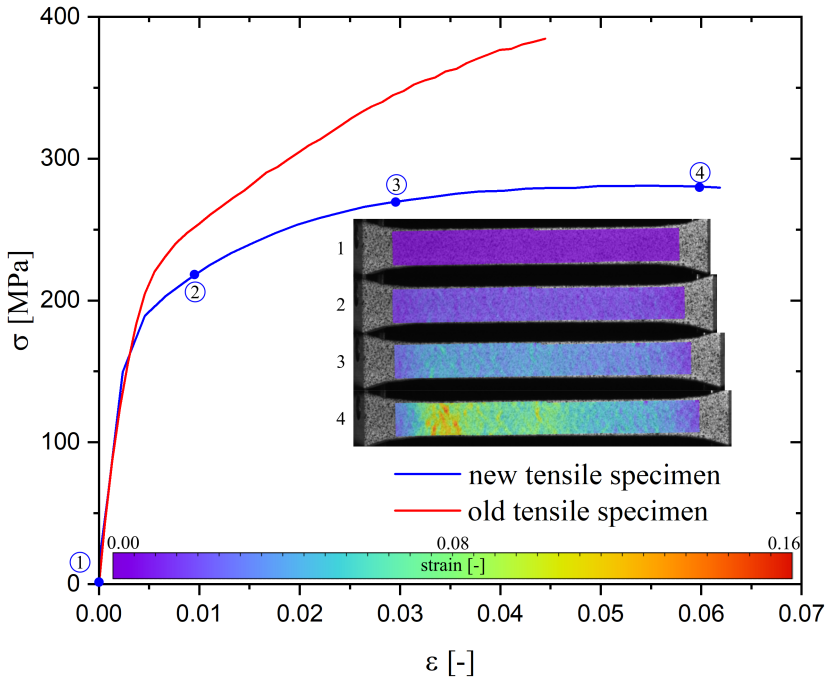

Figure 3.8: Comparison of dog-bone tensile specimens for material model calibration; DIC images of one tensile test with points marked on the stress-strain curve (Bronder et al. [21])

The Young's modulus was only slightly corrected from 62.2 GPa to 58.8 GPa. Within the plastic region there is a larger difference and hence 38 new points for

a plastic table were extracted from the stress-strain diagram. The diagrams in Figure 3.8 are the mean values of three experiments each, with almost no deviation, which hints to a good reproducibility of the SLM process. This can also be seen in the comparison of the first batch of dog-bone specimens (Figure 3.9) where the single experiments of the same specimens have only a small scattering. Here, also the angle between specimens and the substrate plate was investigated since the struts of the auxetics are also not all in the same direction and the specimens itself were also manufactured in a tilted fashion. The specimens laying flat on the substrate plate (0°) behaved more brittle and were the weakest. But, all three directions do not deviate far from each other, with the 45° specimens being the strongest. This lead to the decision to produce all later specimens in a way that most struts had a 45° angle between itself and the substrate plate. In the DIC measurement (Figure 3.8) it becomes visible, that the strain is uniformly distributed over the whole specimens, meaning there are no large manufacturing errors. Those would have been visible as a strong localisation of the strain in one region.

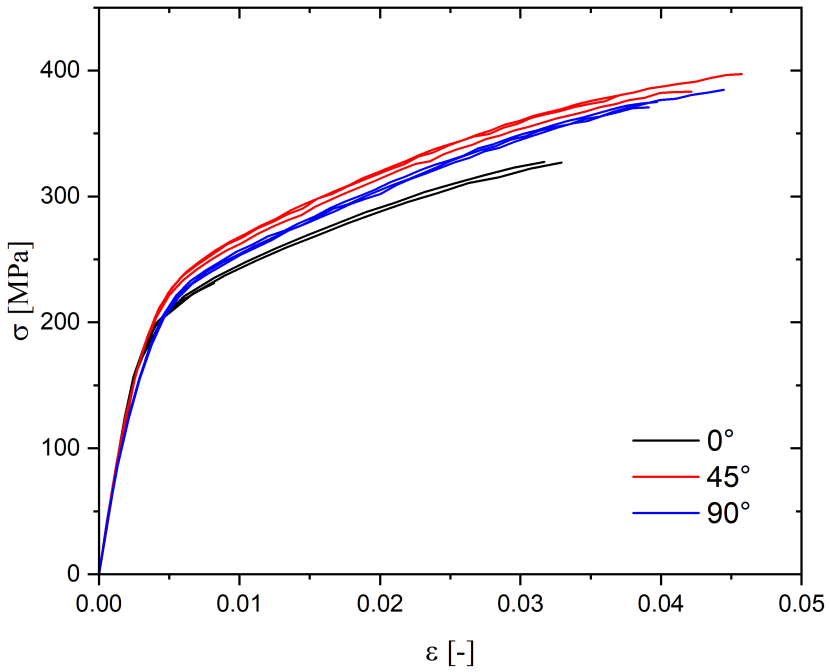

Figure 3.9: Stress-strain results of the first dog-bone specimen batch to calibrate the material model; 0°, 45° and 90° describe the angle between specimen and substrate plate in the SLM process; 0° means the specimens were flat on the substrate plate (Bronder et al. [22])

The simulation build up the database for the subsequent neural network training and optimisation process. Also an inspection of the later design space in form of a full factorial testing plan was performed commencing with simulations and followed by experimental validation of the results.

3.3 Full factorial testing Plan

Exploration of the design space was performed with a full factorial testing plan in simulation and experiment for three out of five geometry parameters. The parameters **waist, size** and **strut thickness** (Figure 3.1) were investigated while keeping the re-entrant angle and gap between half strut and unit cell constant. The three selected parameters were deemed the most influential ones and were varied between a maximum (1) and a minimum (-1) value. In addition, since the number of necessary specimens is 2^n, with n being the number of parameters, only three parameters were selected to keep the number of specimens within reason. The boundaries (Table 3.2) of the design space were chosen because of the production restrictions of the SLM machine. The maximal values were the largest specimens possible to manufacture while the minimum values were the smallest sensible measurements. Smaller parameters would either have lead to too fragile structures or reached the boundaries of the manufacturing accuracy.

Table 3.2: Minimum and maximum values for the geometry parameters varied within the full factorial testing plan (Bronder et al.[22])

	waist[mm]	strut thickness [mm]	size [mm]
min (-1)	0.5	0.5	7
max (1)	1.5	1.5	20

In total, this leads to eight different types of specimens which can be depicted as a cube (Figure 3.10). These structures were simulated according to the method described in section 3.2 and produced with SLM in the same fashion as the specimens in section 3.1 with the only difference of the scanning strategy. Specimens with the minimum **strut thickness** of 0.5 mm were produced with total fill, while specimens with the maximum **strut thickness** of 1.5 mm utilised hatch which means stripes as a fill pattern. This was more beneficial for the thicker struts since it produced better surface qualities.

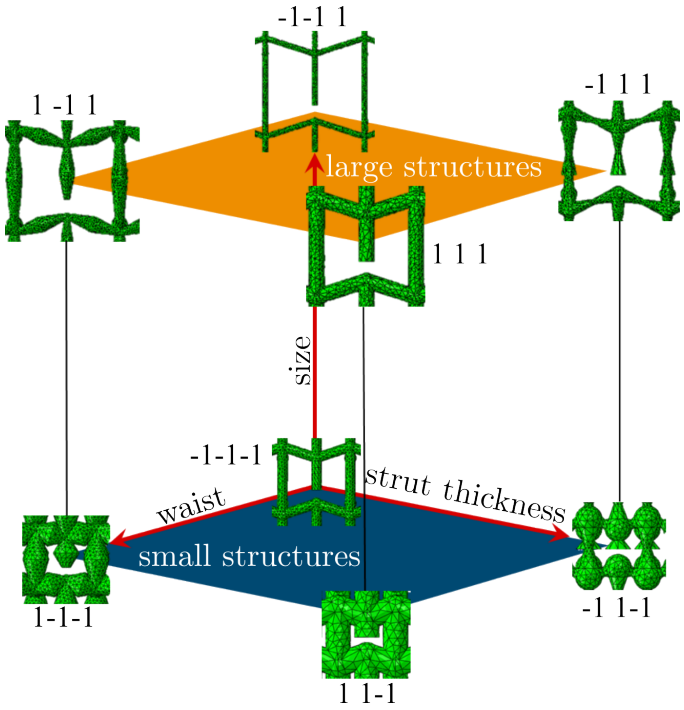

Figure 3.10: Unit cell structure of the eight resulting specimen types in factorial space, with 1 and -1 meaning the max and min value of the geometry parameters, respectively (Bronder et al. [22]).

The produced specimens, again by the institute of production engineering, Saarland University of Prof. Bähre, (Figure 3.11) were all measured (Table 3.3) and subjected to compression experiments with the same machine and camera equipment as the size effect experiments in section 3.1. Also the DIC was performed with ISTRAD4D® to evaluate the strains and Poisson's ratio. Due to the friction on the boundary of the specimens, the Poisson's ratios were only evaluated in the middle layer of the specimens.

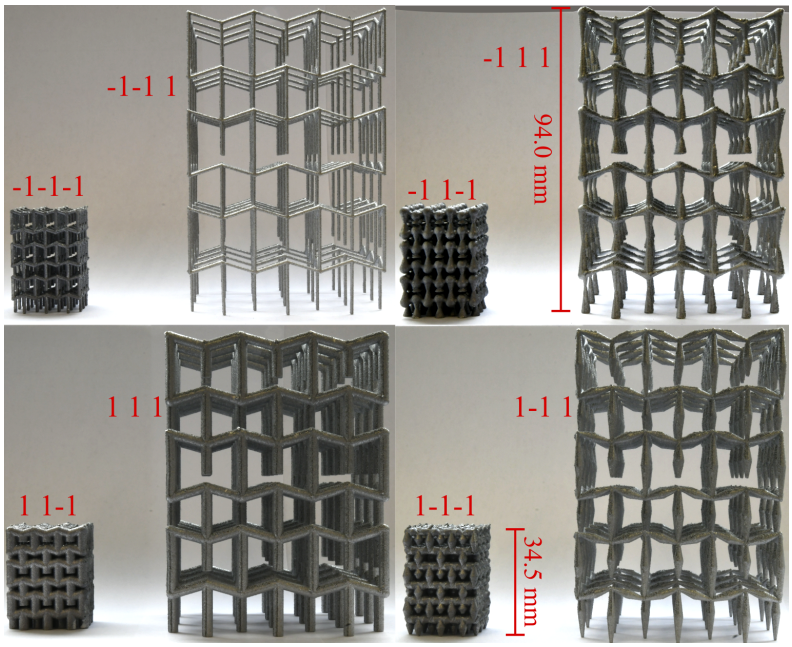

Figure 3.11: All eight types of specimens produces with SLM; 1 and -1 meaning the max and min value of the geometry parameters, respectively (Bronder et al. [22])

Table 3.3: Mean measures and mass of the manufactured specimens per type; geometry parameters waist(w), strut thickness (st) and size (s)

	w [mm]	st [mm]	s [mm]	length [mm]	width [mm]	height [mm]	mass [g]
small	0.5	0.5	7	22.3	22.4	33.4	3.85
	1.5	0.5	7	24.0	24.1	34.5	17.36
	1.5	1.5	7	24.2	24.5	34.3	26.93
	0.5	1.5	7	24.2	24.6	34.5	14.66
large	0.5	0.5	20	61.6	61.7	94.1	11.27
	1.5	0.5	20	63.0	63.1	93.3	48.55
	1.5	1.5	20	63.4	63.5	93.3	97.82
	0.5	1.5	20	63.2	63.7	95.2	42.89

3.3.1 Simulation Results

The stress-strain behaviour for the eight different unit cells is extracted from the simulations (Figure 3.12) and already shows the huge potential within the small subset of geometry space. There is a wide range of maximum stresses and thus a large variety and optimisation potential for the EAC. The calculated mass specific EAC to incorporate the lightweight goal and the resulting Poisson's ratios are listed in table 3.4. With the aim of achieving a good compromise between EAC and Poisson's ratio in mind, a small structure with waisted struts yields the best result (Table 3.4 green). Apart from the large variety of EACs, also the Poisson's ratio is widely adjustable even in this small fraction of possible geometries. The large structures display a large auxetic effect, yet a low mass specific EAC, whereas the small structures all provide a significantly higher EAC.

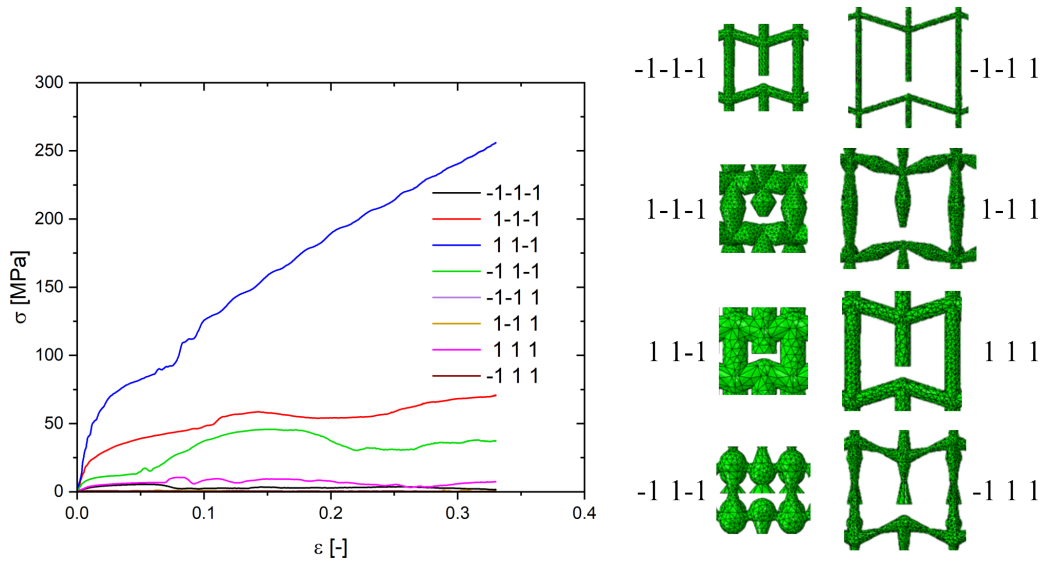

Figure 3.12: Stress-strain diagrams for the eight different specimens extracted from the simulation of compression experiments; respective unit cells on the right (Bronder et al. [22])

With linear approximation, the effects of the single parameters on the target values can be visualised (Figure 3.13 a)). The geometry parameters have directly opposing impacts on the target variable since the goal is to maximise the EAC while having a large as possible auxetic effect. The slope of the straight line between min(-1) and max(1) value measures the strength of the impact, thus showing the **size** to have the strongest influence, followed by **waist** and **strut thickness**. Moreover, increasing the unit cell size has the opposite effect on EAC and Poisson's ratio compared to **waist** and **strut thickness**. In order to find one

Table 3.4: Calculated mass specific energy absorption capacity EAC and Poisson's ratio ν from the simulations. 1 and -1 denote to the max and min value of the three geometry parameters waist, strut thickness and size, respectively. Green marked is the best compromise for both target values (Bronder et al. [22]).

	parameter level	EAC [mJ mm^{-3} g^{-1}]	ν [-]
small	-1-1-1	0.2199	-0.33
	1-1-1	0.8933	0.03
	1 1-1	1.8009	0.01
	-1 1-1	0.5941	-0.45
large	-1-1 1	0.0030	-0.64
	1-1 1	0.0024	-0.67
	1 1 1	0.0026	-0.44
	-1 1 1	0.0188	-0.41

single optimisation goal, the product of EAC and Poisson's ratio was chosen as a first simple approach (Figure 3.13 b)). Curiously, the **waist** has the largest impact here, followed by **size** and **strut thickness**. The tendencies, nonetheless, are the same as for the single target values.

The evaluation of the interactions between the parameters only yields the **size** and **waist** to have the strongest interaction. This however, is clear a priori since these two parameters have the biggest influence on both target variables. Hence, there is no further information gain from the interaction plots what cannot already be concluded from the effect diagrams.

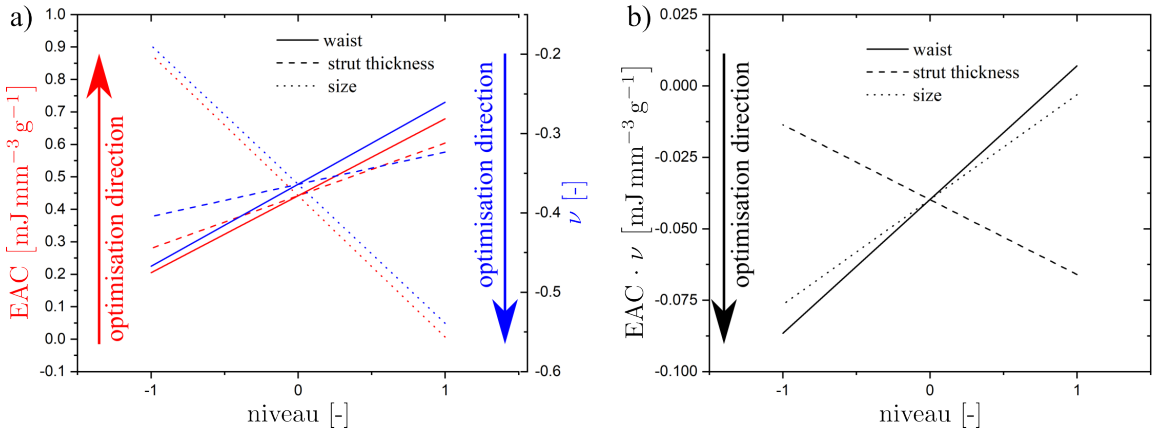

Figure 3.13: a) Effect plots of the geometry parameters on the energy absorption capacity E and the Poisson's ratio ν. The optimization of E is opposing the optimization of the Poisson's ratio; b) effect plots of the product E·ν (Bronder et al. [22]).

3.3.2 Compression Experiments Results

The comparison between simulation and experiment (Figure 3.14) yields a good accordance for the two in the pseudo-elastic regime before the plastic collapse peak. Afterwards there is a larger discrepancy because of the wrongly calibrated material model as mentioned in section 3.2. However, the simulations still give valuable insight into the general behaviour of the structures. Noticeable is the increase in the PCS for the smaller structures compared to the larger ones. For the structures with straight struts it is only an increase by a factor of approximately 14, the structures with waist and belly increase their PCS by a factor of approximately 50.

An additional reason for the discrepancies between simulation and experiment is a shearing-off during plastic deformation instead of collapsing in a straight fashion as was the case within the simulations (Figure 3.15). This is more dominant for the large structures since this shearing is a result of a bending dominated deformation mechanism. As a result the half strut does not reach contact at all and loses its functionality. Therefore, the small structures show better accordance for simulation and experiment. This behaviour is another reason why the Poisson's ratio was only calculated and compared before the first collapse of the structures.

Table 3.5: Experimental (exp) and simulated (sim) Poisson's ratio ν and energy absorption capacity E up to 5% strain for the eight parameter sets, with their respective errors e. -1 and 1 represent the min and max value of the three geometry parameters waist, strut thickness and size, respectively. Marked in green is the best compromise solution for the experiment, which is the same as for the simulations (Bronder et al. [22]).

		ν_{exp} [-]	ν_{sim} [-]	e_ν [-]	E_{exp} [mJ mm^{-3}]	E_{sim} [mJ mm^{-3}]	e_E [-]
small	-1-1-1	-0.40	-0.33	0.175	0.137	0.201	0.31
	1-1-1	0.13	0.03	0.76	1.564	1.456	0.07
	1 1-1	0.16	0.01	0.94	3.443	3.246	0.06
	-1 1-1	-0.22	-0.45	1.05	0.313	0.529	0.41
large	-1-1 1	-0.51	-0.64	0.25	0.002	0.007	0.71
	1-1 1	-0.40	-0.67	0.68	0.009	0.022	0.59
	1 1 1	-0.36	-0.44	0.22	0.141	0.249	0.43
	-1 1 1	-0.34	-0.41	0.21	0.013	0.029	0.55

The simulations of the large structures (Figure 3.14e)-h)) further display an oscillation behaviour after the PCS not visible in the experiments. This is a result of the contact of half strut and structure during the deformation. After contact a slipping occurs which leads to these oscillations. Since there is less space within the smaller structures (Figure 3.14 a)-d)) and the half strut is shorter, there is no slipping and sudden collapse possible, hence no oscillations.

Table 3.5 compares the resulting Poisson's ratio and EAC for experiment and simulation. For the larger structures the simulations overestimate the negative Poisson's ratio while they underestimate it for the smaller structures with the only exception being the structure with waisted struts (-1 1-1). Yet, the overall tendencies are similar. As already visible from the stress-strain diagrams, the EAC up to 5 % strain are a better match for the small structures. The area was only calculated this far because the small structure with thick struts (1 1-1) could experimentally only be evaluated until this compressive strain. The experiments further validate the small structure with waisted struts to be the best compromise solution for EAC and negative Poisson's ratio. Thus, the experiments verified the overall tendencies, meaning the simulations are applicable for an optimisation task. They give good estimates of the qualitative behaviour and influence of the parameters.

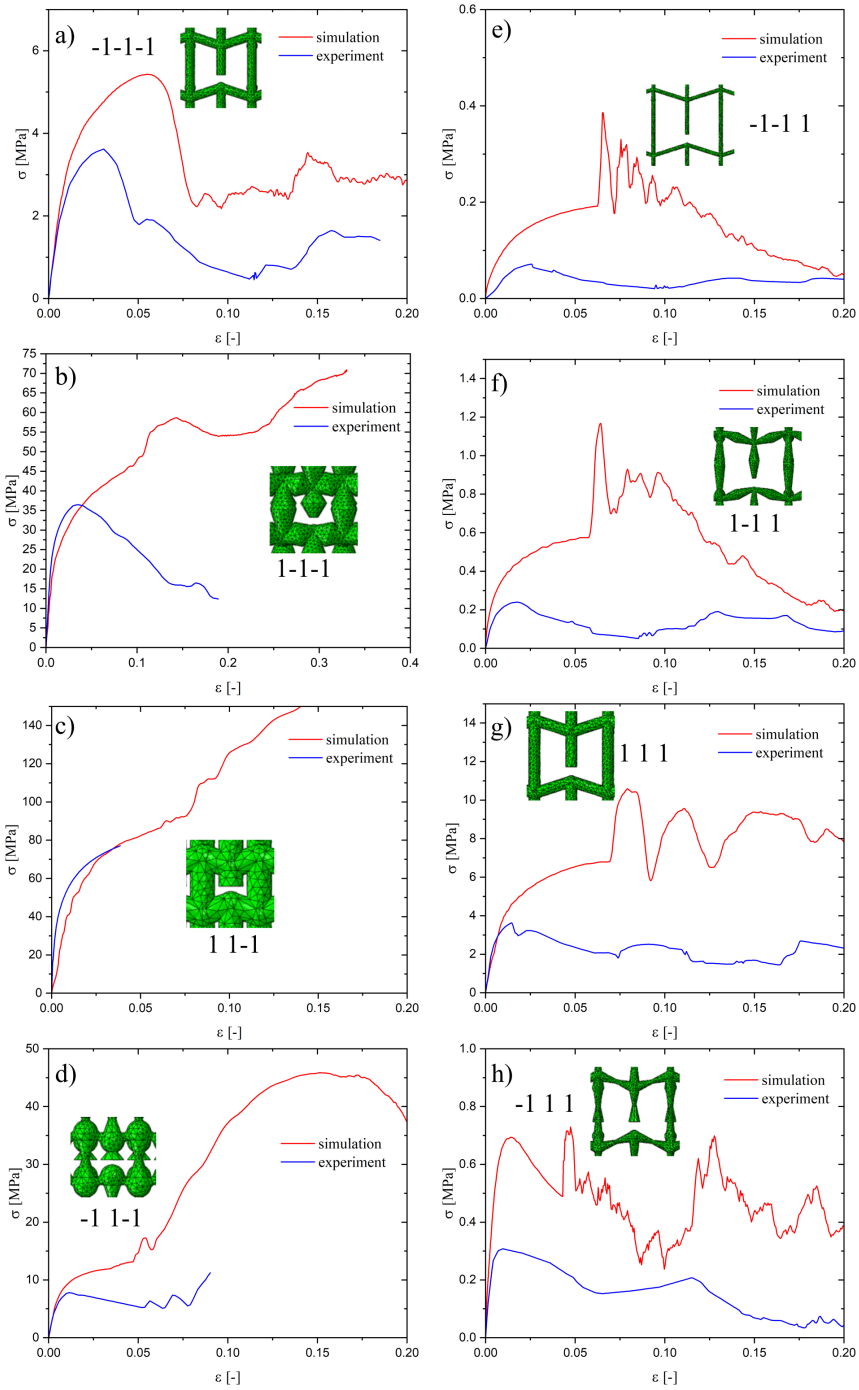

Figure 3.14: Stress-strain diagrams of the simulations compared to the experiments. All experimental curves are the mean value of three experiments. The geometry parameters are according to table 3.2. The small structures are on the left (a)-d)) and the large structures on the right (e)-h)) (Bronder et al. [22]).

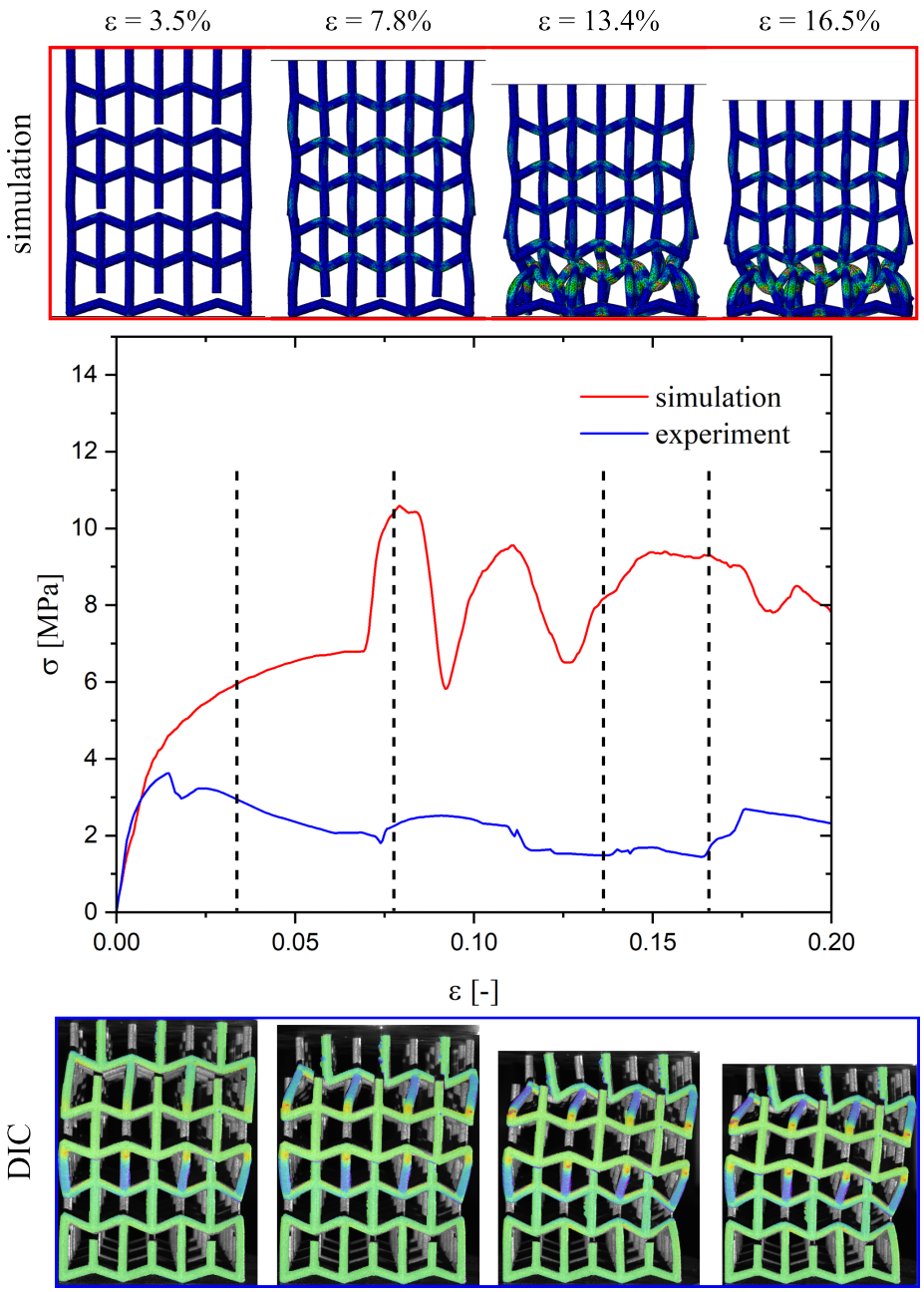

Figure 3.15: Comparison of the deformation behaviour between simulation and experiment for specific global strains ε on the example of the large structure with all geometry parameters on maximum level (1 1 1); differing deformation mechanism of simulation and experiment becomes apparent (Bronder et al. [22])

3.4 Network Training and Optimisation

After the investigation of the design space and the generation of some initial training data points within these boundaries, different ML algorithms were investigated in the master thesis of Sergej Grednev [59], which resulted in neural networks to be the best approach for the given task. Especially for predicting stress-strain curves, they were superior compared to support vector machines, k-nearest neighbours or decision tree based approaches such as boosting.

3.4.1 Neural Network Architecture and Training Process

For the implementation of the neural networks the application programming interface (API) Tensorflow with Keras was used. The training data was generated in the same fashion as described in 3.2. Since some investigations were launched in parallel, the sampling of the training data is not entirely random. An adaptive sampling algorithm was developed by Janis Mathieu [97] during his master seminar, which showed the adaptive sampling algorithm to reach a lower generalisation error with fewer training examples. Therefore, the training data for the final optimisation here is sampled as a combination of random sampling and adaptive sampling.

Two different feed forward neural networks were designed for the two targets stress-strain behaviour and Poisson's ratio ν. For the stress-strain relation, a subsampling approach was used, meaning the network had 201 output nodes, each predicting the stress at a certain strain. Since the simulations yielded 1001 stress-strain pairs, a data reduction was used because it is easier for the network to predict fewer values and hence this is called subsampling. As input for both networks solely the five geometry parameters were used. For predicting the stress-strain behaviour four hidden layers, in order 30, 50, 100 and 200 neurons per layer , were found to give a good approximation. As for the prediction of the Poisson's ratio a network with a total of nine hidden layers, five with 40 and four with 20 neurons per layer was found to give good estimates of the single output value. All neurons used the SELU activation function because of its self-normalising properties and thus the networks were initialised with lecun-normal. The stress-strain network was trained with Huber loss while the Poisson's ratio network was trained with the MAPE.

The suitable networks were established through gradually increasing the number of layers and neurons per layer starting from just two hidden layers with 50 neurons each. The final training was done on 179 simulations with four fold cross validation which means that only 80 % of the available data was used for training

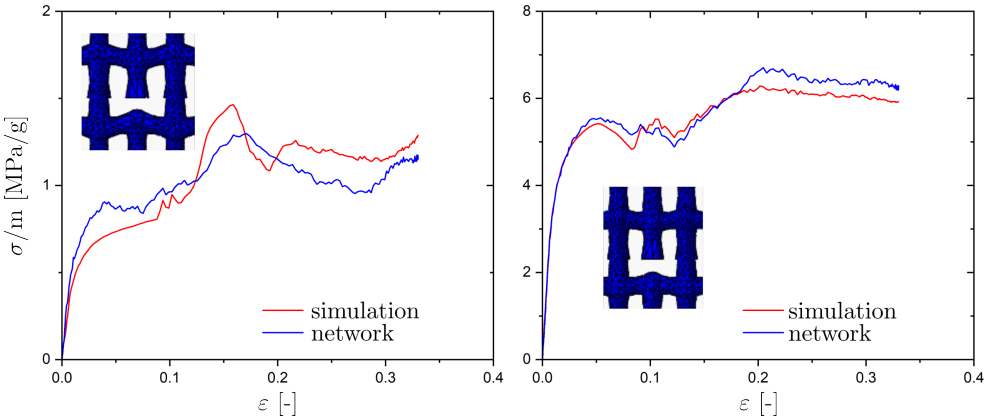

Figure 3.16: Exemplary test stress-strain diagrams of the trained neural network confirming the good predictions; left is the test data with the largest prediction error on the test dataset

10 % for validation and 10 % for testing. Thus all data was shuffled four times and split accordingly, resulting in 4 different data compilations to minimise the influence of the data selection on the training. Yet, there is no way to guarantee that those are the best achievable networks for the task, they are only one possibility within an acceptable margin of error on the test data. The validation data was used for early stopping to prevent overfitting.

As mentioned above, in general it is easier to predict fewer numerical values. Hence why not predict the EAC directly instead of the whole stress-strain behaviour? Firstly, the stress-strain behaviour can directly be compared with the compression experiments and gives a better understanding of the material behaviour in general. Secondly, it would additionally be possible to evaluate stiffness, PCS and plateau stress from the stress-strain behaviour and utilise them for further investigations. And thirdly, for a homogenisation approach it is mandatory to know the material behaviour, e.g. the stress under certain compressions. Hence, the trained neural network can later be used to model the homogenised material behaviour.

From the four-fold cross validation resulted four trained networks, whose performance was evaluated on the test data and the network with the smallest test error, a MSE of 0.107 or Huber 0.051, was selected. Exemplary stress-strain predictions of the selected network (Figure 3.16) confirm that the predictions give a good approximation of the simulations. Even the worst prediction (Figure 3.16 leaft) is still acceptable to extract a material behaviour and gives a good estimate of the EAC, since the area under the curves do not differ as much.

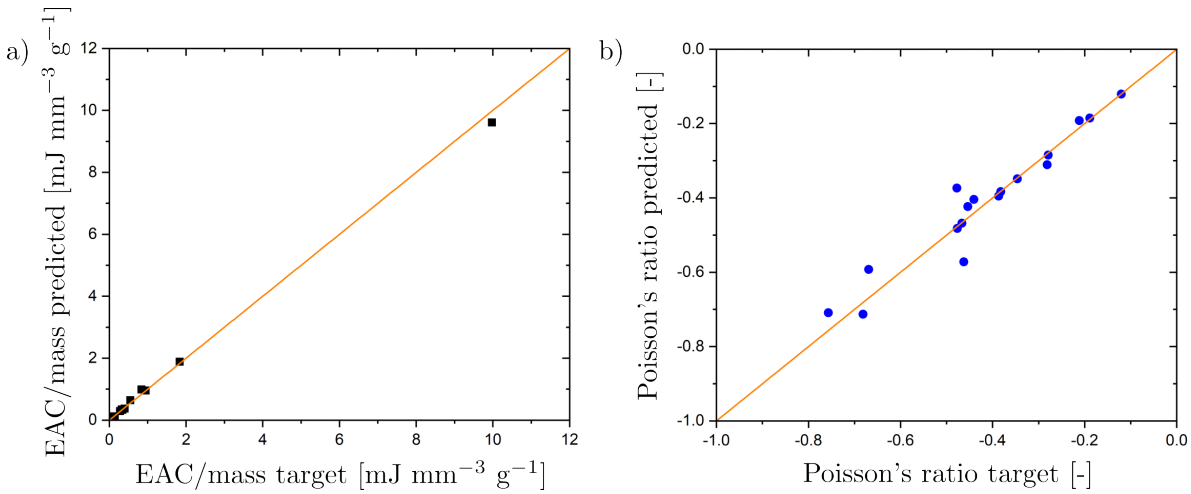

Figure 3.17: Predicted over target value of the test data for a) mass specific energy absorption capacity and b) Poisson's ratio; orange is the straight for a perfect match of both

The good accuracy for both networks becomes also visible when comparing the predictions for both target values to the labels of the test data set (Figure 3.17). The mass specific EAC in Figure 3.17 a)) is calculated from the predicted mass specific stress-strain diagrams. The area is integrated numerically using Simpson's rule [35]. The final network can then be used to optimise the structure.

3.4.2 Optimising the Structure

Finding the best structure in the case of the auxetics means a high as possible mass specific EAC with a small as possible Poisson's ratio, which boils down to a minimisation problem. To that end, the quasi Newton procedure L-BFGS-B, implemented in the python library scipy, was utilised in combination with a surrogate model technique. A multidimensional, quadratic polynomial function of the form

$$\begin{aligned} T =& ax_0 + bx_0^2 + cx_1 + dx_1^2 + ex_2 + fx_2^2 \\ &+ gx_3 + hx_3^2 + ix_4 + jx_4^2 + kx_0x_1x_2x_3x_4 + l \end{aligned} \tag{3.1}$$

was fitted by the method of least squares to the existing data. Here, T is the optimisation target, which is the product of mass specific EAC and Poisson's ratio, $\mathbf{x}$ is the geometry parameter vector and a to l are curve fitting parameters. The product of EAC and Poisson's ratio as minimisation target was chosen since this value must be as negative as possible. The EAC itself is always positive while the Poisson's ratio should be negative and by multiplication the product of the two becomes larger with increasing magnitudes.

The minimisation results in a new set of geometry parameters, for which the neural networks approximate Poisson's ratio and EAC. This in turn extends the already existing database of geometry parameters to target variables list, which is then refitted to the surrogate model. The newly adapted model is then minimised again and in turn results in a new set of geometry parameters. This procedure is repeated until a previously set cancellation criterion is fulfilled, e.g. difference between target values of current and previous step is below 0.1 % (Figure 3.18). In this way, it is possible to incorporate the whole minimisation history and use the set of simulations already existent for the optimisation.

After multiple runs of the optimisation algorithm from different starting points one final set of geometry parameters emerged (Figure 3.19 table). Those were subjected to a FE simulation in order to validate the approximation of the neural network. The good accordance of network prediction and simulation for stress-strain behaviour and Poisson's ratio (Figure 3.18) verifies the optimisation. Now, only the experimental validation of the optimisation is still pending.

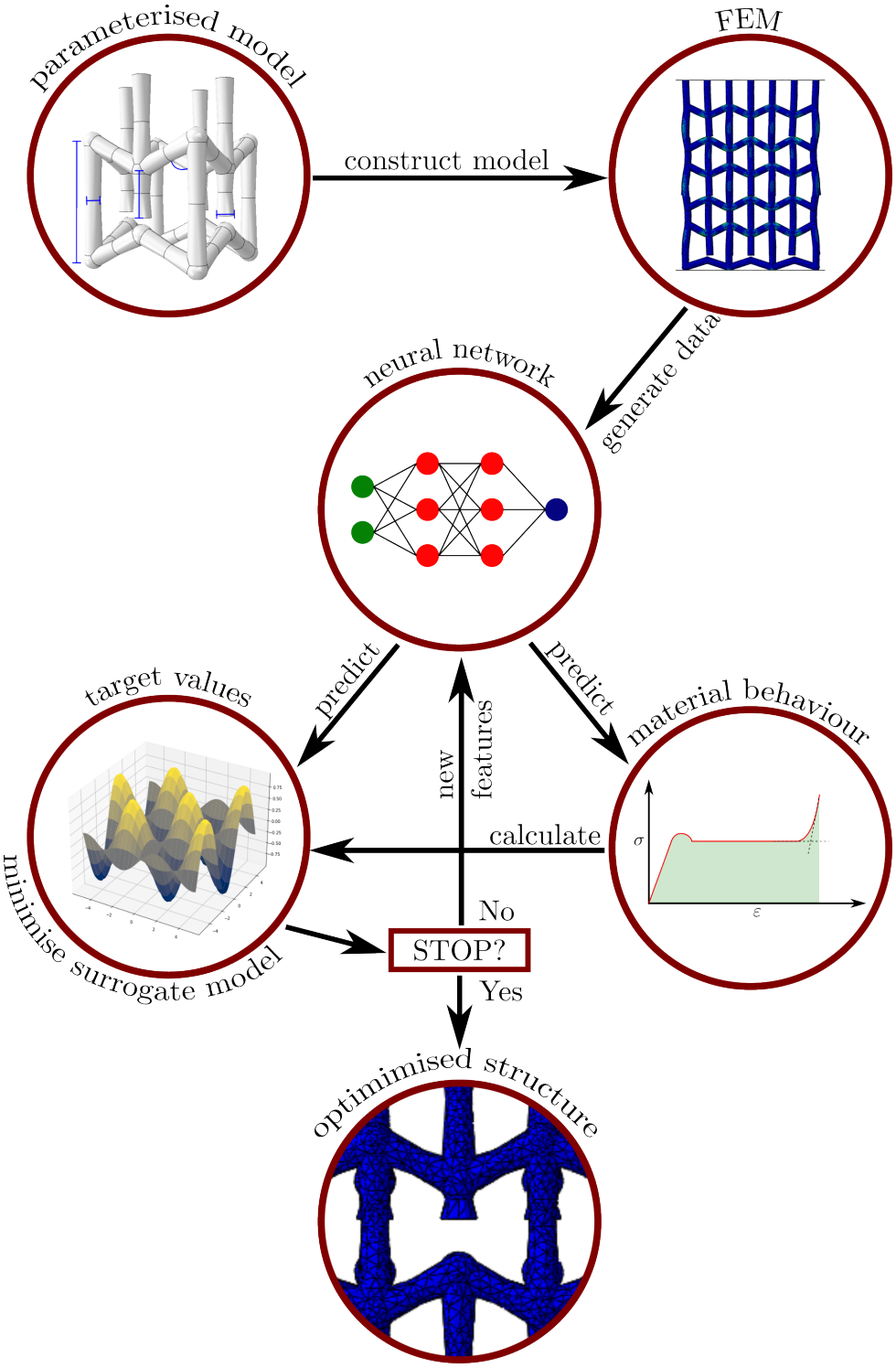

Figure 3.18: Schematic of the optimisation routine

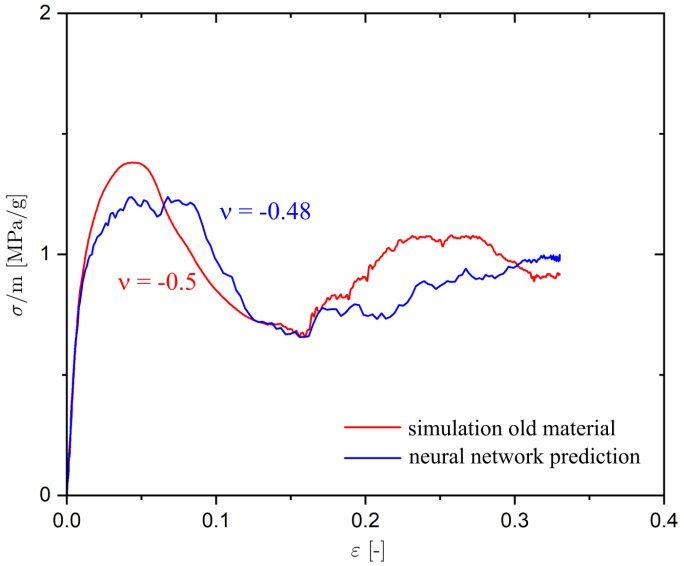

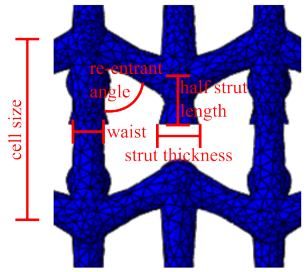

parameter	value
waist	0.56 mm
strut thickness	0.78 mm
re-entrant angle	65.61 °
cell size	7.29 mm
half strut length	1.66 mm

Figure 3.19: Stress-strain diagrams of the optimised structure for neural network prediction and validation simulation; additional table with the optimised values of the geometry parameters

3.5 Experimental Validation

To investigate the optimised structure, a set of three specimens was produced by SLM at the institute of production engineering, Saarland University of Prof. Bähre with the same production parameters as the specimens in section 3.1 (Figure 3.20). All specimens were subjected to compression experiments with the same experiential equipment and setup as all previous compression experiments. The resulting stress-strain behaviour is compared to the results of the validation simulation (Figure 3.21). The large discrepancy between simulation and experiment is due to the wrongly calibrated material model discussed in section 3.2. With the recalibrated elastic-plastic model, experiments and simulation are a much better match.

The still remaining mismatch is a combined result of a deviating failure mechanism (Figure 3.22), a non perfect manufacturing and the exclusion of material failure. During the simulations the auxetic structures failed in the middle layer whilst during the experiments the topmost struts were bending and buckling. Since the main structure stayed undamaged, it could not bear the load to its fullest and was rendered weaker as predicted. Hence, also the Poisson's ratio is different. In addition, SLM is a process still to be perfected and under heavy investigation. The predicted mass of the ABAQUS® with 6.98 g differs from

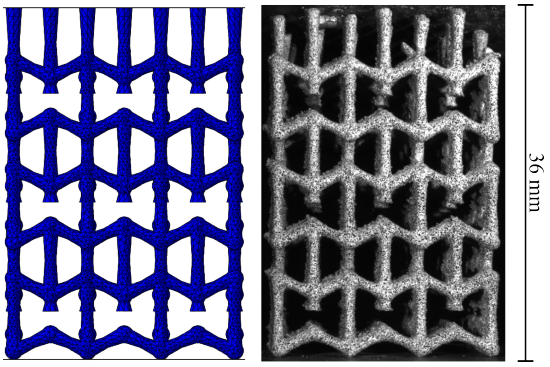

Figure 3.20: FE model left and SLM specimen right of the optimised structure; a black and white speckle pattern is applied to perform DIC (Bronder et al. [21])

the specimens with only 6.82 g. This deviation of 2.3 % hints to either deviating dimensions, small pores or pre-existing damage within the structures, which all could potentially lead to an earlier failure. Also the inclusion of damage in the material model can potentially improve the accuracy of the simulations, but leads to increased simulation times. This was researched in the master thesis of Alexander Engel [41]. Nevertheless, the validation of the optimisation was successful. Also the mass specific EAC of $0.19\,\mathrm{mJ\,mm^{-3}\,g^{-1}}$ for the experiments matched the $0.22\,\mathrm{mJ\,mm^{-3}\,g^{-1}}$ for the simulations closely.

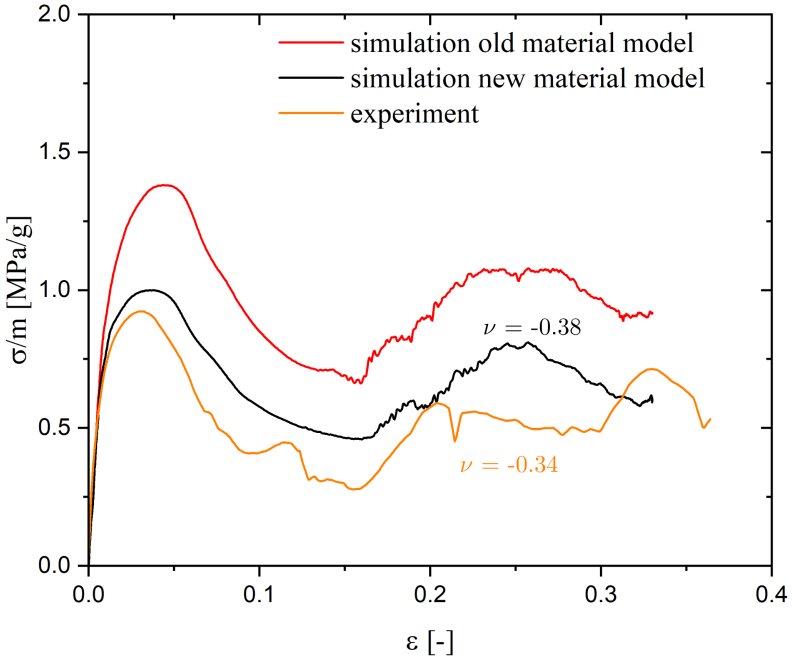

Figure 3.21: Stress-strain diagram comparing the experimental results as mean of three compression experiments with the simulations of the optimised structure

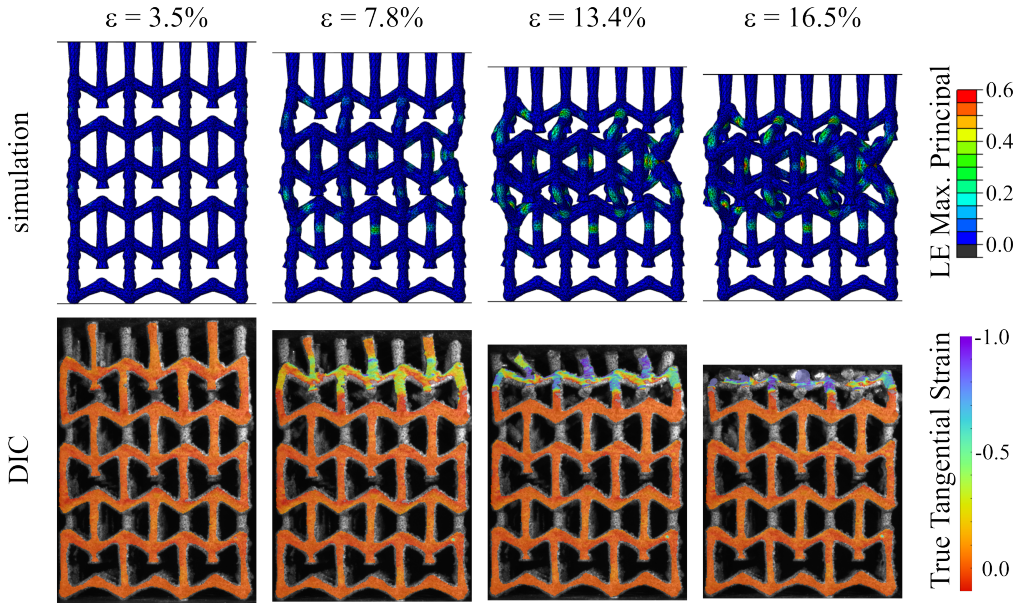

Figure 3.22: Comparison of deformation during compression of simulation and experiment for different global strains

3.6 Main Results

This chapter dealt with the optimisation of a modified 3D auxetic re-entrant honeycomb structure and the development of an optimisation routine. The key findings are briefly summarised within this section.

- The modified version of the auxetic unit cells keeps its stiffness for larger deformations and is able to withstand higher stresses and thus has an enhanced EAC
- The RVE was established to be $3 \times 3 \times 3$ unit cells through an experimental investigation on size effects. The PCS and PS for this specimen type was well within the deviation of the single experiments and gives a good estimate of a global behaviour while preserving a small as possible modle to reduce simulation time.
- A full factorial testing plan was established to investigate the design space for three out of five geometry parameters. The two main targets, negative as possible Poisson's ratio and high as possible mass specific energy absorption capacity are contradictory to each other. Thus, a compromise solution must be found which is achieved through an optimisation of the product term of both targets.
- The simulative investigation was confirmed by experiments and lead to a recalibration of the material model to counter the discrepancies between simulation and experiment.
- Multiple neural networks were trained and validated to predict either the stress-strain behaviour or the Poisson's ratio based on geometry parameter composition. The ones with the best performance were picked to perform a structural optimisation of the modified 3D re-entrant honeycomb auxetics.
- Through the combination of the neural networks and a surrogate model technique with a multidimensional quadratic function, the structure for the auxetics was optimised and resulted in a small structure with waisted struts. This compromise solution was again subjected to experimental testing and validated the results from the simulations. Also the simulations validated the neural network predictions and hence the optimisation itself.
- All those steps together give a new optimisation scheme, which can be utilised for arbitrary structures. The only requirement is some kind of numerical representation which is simple and yet complete in describing the structure and the design possibilities.

4

Pentamode

This chapter deals with optimising pentamode structures to improve their damping capabilities. The optimisation procedure, developed on the auxetic structures (Figure 3.18) is transferred to the pentamode structures. The general aim is to optimise the damping for transversal deformations while keeping the mass as small as possible and preserving a structural stability, so axial forces do not crush the structures. A possible application could be protective devices for seismic activities as postulated in [44]. To that end, four geometry parameters **strut length**, **angle**, **middle** and **connection** (Figure 4.1) describing the geometry were identified. One pentamode unit cell is composed of four bases. The only expansion to the structure described in the literature from 2.5.2 is the introduction of the angle.

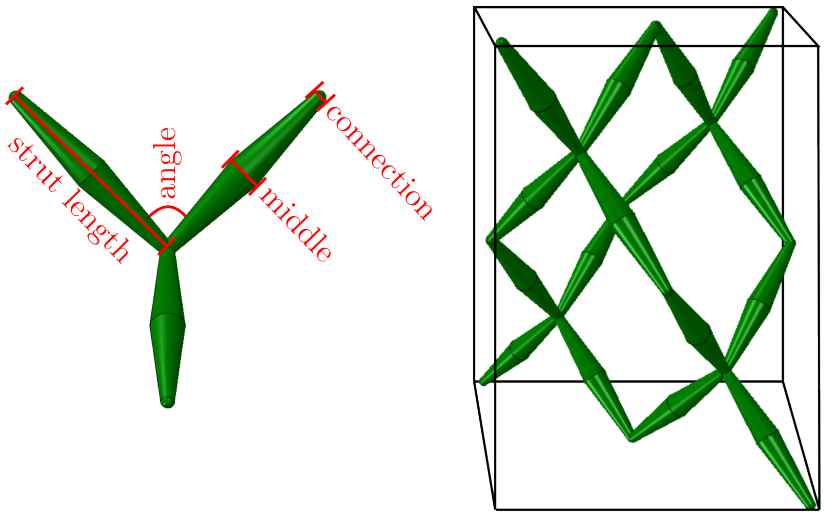

Figure 4.1: Schematic of the pentamode structure; left is the base with the four identified geometry parameters; right is an assembled unit cell

In this chapter an overview of the simulation setup is given, followed by the investigation of the design space and training the neural network with adaptive sampling. Finally, the pentamode structure is optimised with regard to the mass specific damping. Since a new set of simulations is needed to calculate the structural stability, this was only carried out for the initial investigation of the design space due to time constraints, but will be the subject of future investigations. Also the experimental investigation was omitted because of the lack of time. So all the results presented within this chapter are purely the result of simulations, specimen production and testing will be done in the future.

4.1 Simulations

The FE simulations were all done with the ABAQUS® explicit solver on models composed out of four unit cells. The structure was placed between two rigid plates, similar to the auxetic specimens. For the damping simulations the upper plate was rotated oscillating around the longitudinal axis ± 10° with a frequency of 2.5 Hz in order to mimic vibrations (Figure 4.2 a)). As for the structural stability simulations, the pentamode structure was compressed under uniaxial loading until 33 % strain (Figure 4.2 b)). The frequency can be regarded as another tailoring parameter but was left constant for the following investigations in order to reduce the number of features for a first inspection of the design space. The 2.5 Hz were chosen because they fit into the frequency range of most earthquakes which is between 0.1 Hz and 10 Hz [139] and has a deformation speed which is feasible to simulate within a reasonable time frame. The lower plate is fixed in space and serves as a sensor, measuring the reaction forces and moments in both simulations. A tie constraint is used in the vibration simulations to bind the closest nodes to the movement of the respective plate and thus make the simulation as close as possible to an achievable experimental setup. For the compression simulations a contact formulation similar to the one for the auxetics in section 3.2 is implemented also with a friction coefficient of 0.1. Here, it is also expanded with a hard contact in normal direction to minimise surface penetrations, since the contact geometry of the pentamode structures is more complex.

Because of the complex geometry, the structure was meshed utilising tetrahedrons and since a fine mesh was required, linear elements (C3D4) were used. They provide enough accuracy and keep the simulation time within a practicable measure. Quadratic elements would have an estimated simulation time of over 120 days for just one structure and a coarser mesh would give insufficient results or would not represent the geometry correctly, especially for small joints. Again, the recalibrated SLM AlSi10Mg material model from section 3.2 as an elastic-plastic model was employed, since the specimens were planned to be

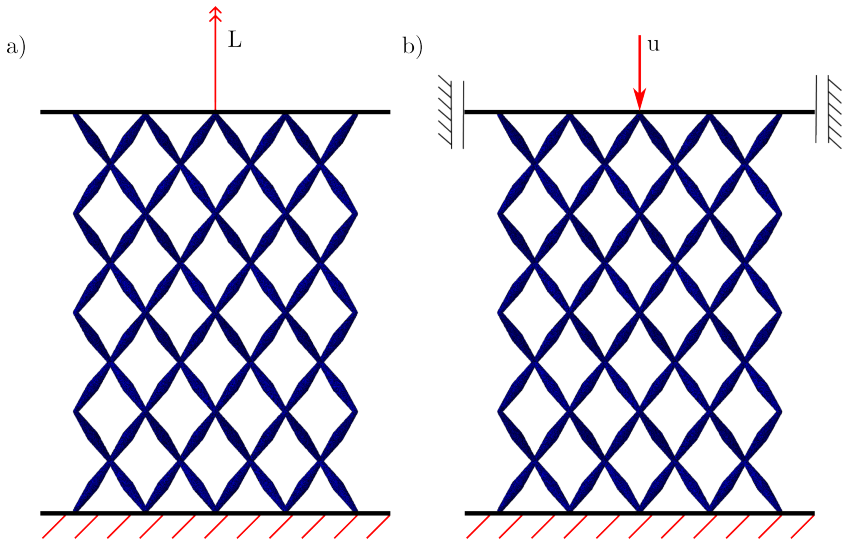

Figure 4.2: Setup of the simulations for the pentamode structure, a) vibration simulations with rotation L b) compression simulations for structural stability with displacement u; the lower plate fixed in space measures the reaction moments and forces in both simulations

manufactured on the same SLM machine. Also, the oscillation simulations had to be done until 4 s, since there was a transient response to the oscillations (Figure 4.3). Meaning, the mechanical wave needs a certain amount of time to stabilise the forced oscillation within the structure. This however, is not only linked to the specimen dimension, since for some specimens the transient response time is almost zero. But since there are specimens with a longer time period, the measure for the damping is the area under the curve of moments after 2 s. This is called *action* (S) and is a measure for the change of a system over time with the unit Joule-second. The action is smaller the better the damping. From the first inspection of the simulation result also a phase shift between oscillation input and reaction moment becomes apparent. It is represented by the time shift of the respective minima and maxima of the forced oscillation at the top and the reaction moment at the bottom. Nevertheless, this has no direct impact on the damping properties of the structures.

The compression simulations resulted in the usual stress-strain relations, from which a structural stiffness is obtainable. This however, is not the Young's modulus, which would have to be measured from an unloading of the structure. For porous structures there exists only a pseudo-elastic regime, which is due to minor plastic deformations already happening during this loading stage. Thus, to gain the purely elastic information, an unloading step during the pseudo-elastic

deformation stage would be necessary. Even so, this unloading is omitted for the simulations, since the structural stiffness is sufficient to evaluate the stability and an additional simulation step would only lead to prolonged simulation times.

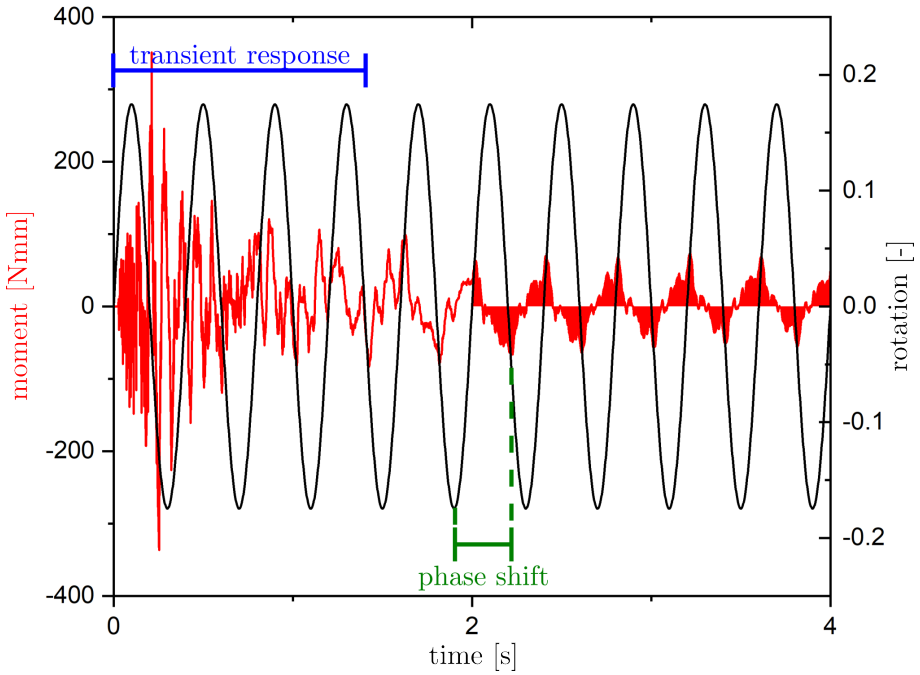

Figure 4.3: Reaction moment for the oscillating simulations on the pentamode structures; the area filled in red under the moment curve after 2 s was evaluated for the damping purposes

4.2 Investigation of the Design Space

In order to gain a deeper understanding of the design space and to explore its limits, a simulative investigation again with a 2^3-full factorial testing plan was utilised. Therefore, the parameters **strut length**, **middle** and **connection** were varied between an minimum (-1) and maximum (1) value (Table 4.1). Hence, this resulted in eight different geometries (Figure 4.4) to be simulated with the parameter angle kept constant at 109.4°. This angle was chosen since it is the tetrahedral angle which is proposed in literature [102] for pentamode structures as they are based on diamond structures. The respective min and max values of the parameters were chosen according to the production constraints of the SLM machine used to produce all auxetic specimens. Smaller parameters, especially for **connection** and **middle** would have caused severe problems with the resolution of the SLM machine, whereas a factor of ten for min to max value

Table 4.1: Minimum and maximum values for the geometry parameters varied within the full factorial testing plan of the pentamode structures

	middle [mm]	connection [mm]	strut length [mm]
min (-1)	0.25	0.24	6
max (1)	2.5	2.4	12

was deemed large enough for this investigation. The **strut length** minimum was chosen in order to still generate sensible structures for the max values of the other two geometry parameter. The max **strut length** here is restricted due to the design space of the SLM machine. Also to avoid meshing problems with the ABAQUS® meshing tool, **connection** and **middle** have slightly different values for their respective min and max values.

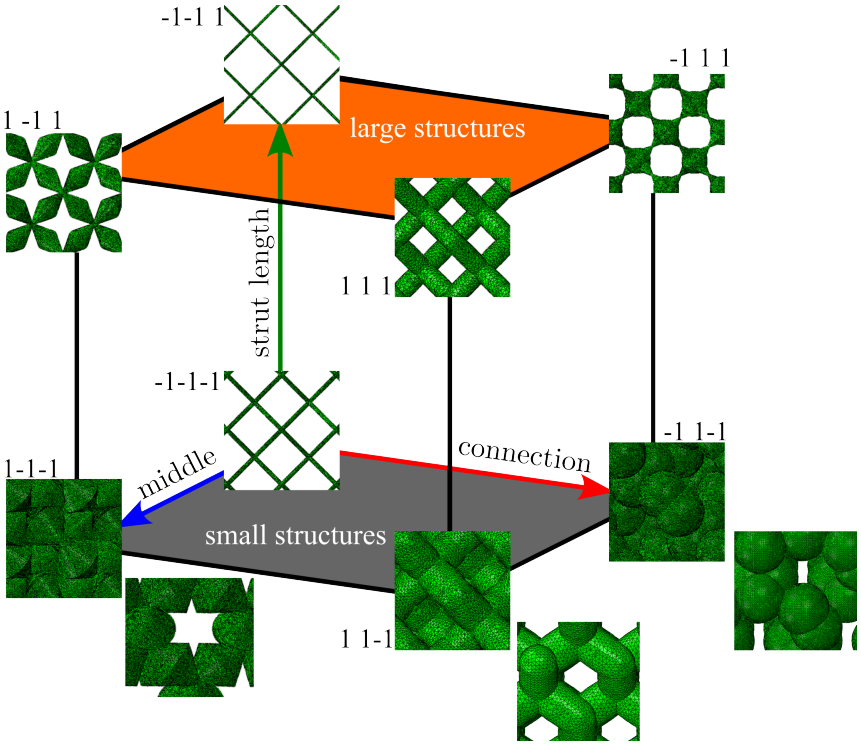

Figure 4.4: Eight resulting structures in the factorial space for the three varied geometry parameters middle, connection and strut length; 1 and -1 describe the respective parameter level; additional rotated view for the smaller structures with at least one parameter on max level for better visibility

For the vibration analysis there is a huge range of achievable moments (Figure 4.5 b)) only by adjusting the chosen three geometry parameters. Hence, also a

good damping is already possible within the chosen confinements of the geometry space. In this case a small reaction moment indicates good damping capabilities. Figure 4.5 c) shows the large variety of resulting actions with a range of roughly 10 000 mJ s for the eight different structures. For the damping there is already a clear trend to structures with longer struts and thus larger structures visible, since their action with one exception is much smaller. It is also apparent, that structures with small connection points display a better damping (Figure 4.5 structures 1, 2, 5 and 6). Structure 8 also displays a significantly lower action even though its **connection** parameter is on max level. This is due to the fact, that the **middle** parameter is minimal and serves as new joints. For structure 4 this effect is not visible because the struts are too small and the connecting spheres touch directly.

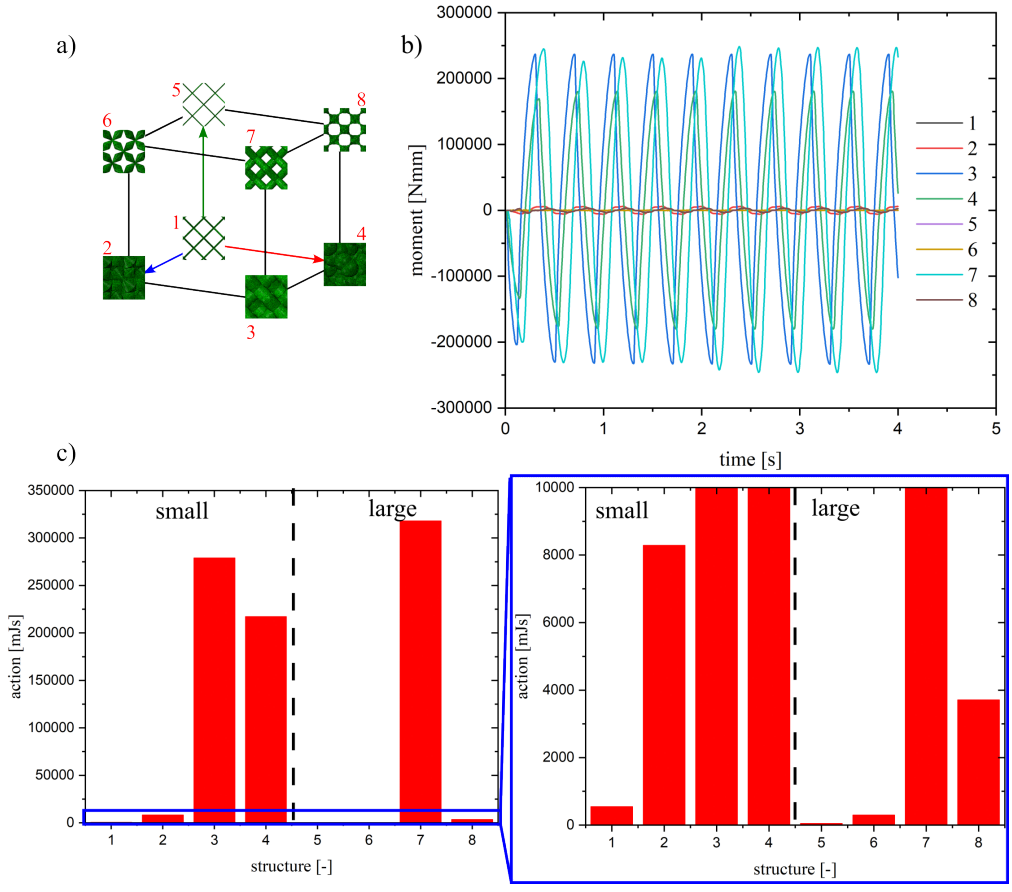

Figure 4.5: a) Structure numbering in factorial space, b) resulting reaction moments for all eight structures, c) calculated actions for the eight structures; smaller reaction moments result in a smaller action and thus a better damping

In addition, the transient response time and the phase shift is significantly lower for some parameter combinations (Figure 4.6). However, for the phase shift there is no clear distinction between small and large structures. Only the small structure with the other two parameters on max level has by far the smallest phase shift. Otherwise, the phase shift has no technical effect, since on the one hand it signifies a delayed response of the structure, but on the other hand this delay is in the range 0.15 s which is also almost instant.

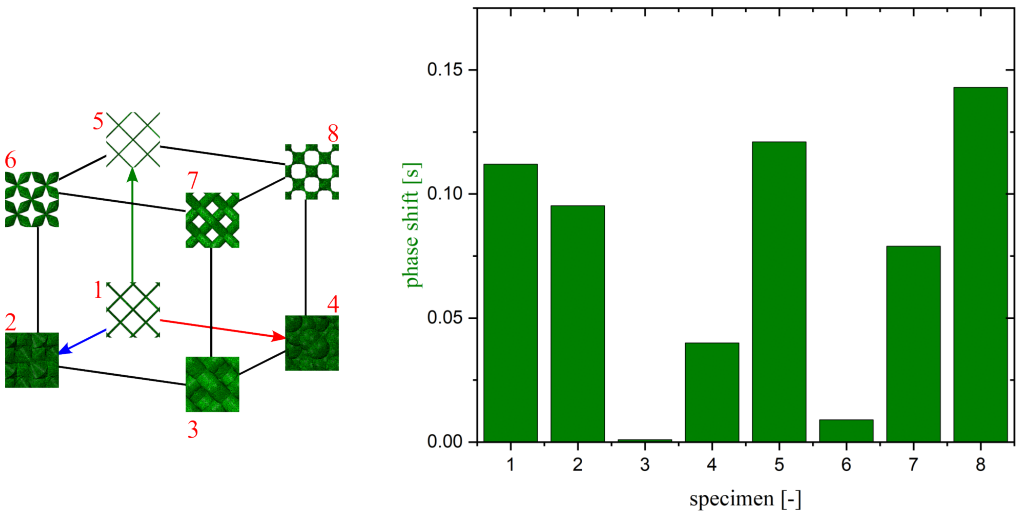

Figure 4.6: Evaluated phase shift for all eight different specimen types of the full factorial testing plan

The mass specific stiffness (E/m) and the yield strength ($R_{p0.2}$) were evaluated with the compression simulation setup from the resulting stress-strain diagrams (Figure 4.7) in order to gain insight into the structural stability. There is a very large difference in scale for the stress-strain behaviour visible with the structures 3 and 4 being the ones capable to withstand the most stress, yet also being the ones with by far the worst damping capabilities. For structure 6 no yield strength could be evaluated since simulating this structure had many issues with meshing and finally only produced reasonable results only up to 4 % strain, which was just enough to evaluate a stiffness. Thus, for the effects discussed below, only the stiffness was taken into account. The resulting values are listed in Table 4.2. There is a clear trend to a higher mass specific stiffness for the smaller structures visible. This is caused by a significantly lower mass for the smaller structures and also a much higher unnormalised stiffness in case of structures 3 and 4 due to their packing factor. The shorter struts which are less prone to bending are another factor for the higher mass specific stiffness compared to the larger structures. In addition, a higher mass specific stiffness is an indicator for a higher yield strength.

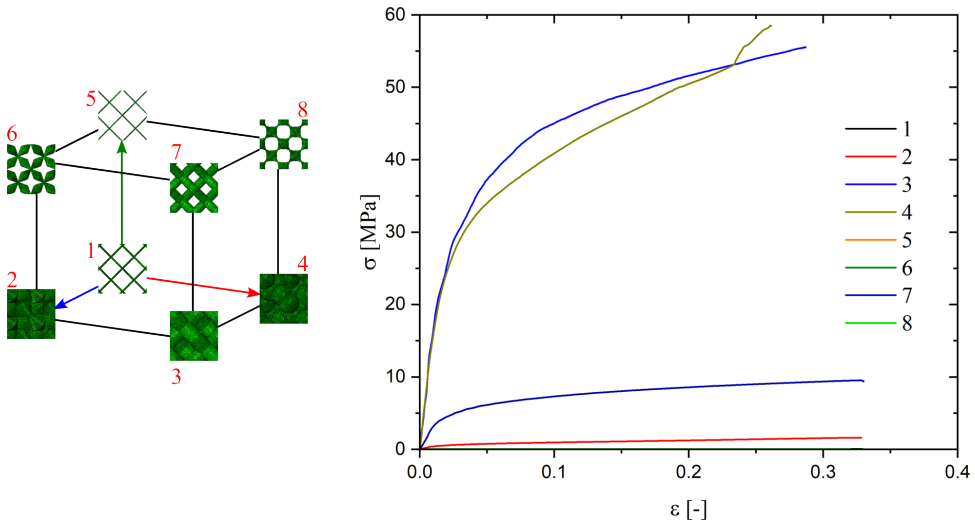

Figure 4.7: Stress-strain diagram for the eight specimens of the full factorial testing plan

The resulting effects of the three varied parameters (Figure 4.8 a)) again display the necessity to find a compromise since the two parameters **connection** and **strut length** influence the optimisation targets in opposing ways. A small **connection** gives a low action yet a small mass specific stiffness, where a small **strut length** results in a higher action but also a higher mass specific stiffness. The cause for this is the diameter of the joints of the single structural elements. For small joints, the mechanical wave transmission is hindered since the shear modulus is lower but the structure is rendered much weaker. This is also apparent from the yield strength (Table 4.2 structures 1, 2, 5). The small **middle** parameter of structure 8 again acts as the new joints with a small diameter and thus renders this structure much weaker.

Only the parameter **middle** gives a clear trend to structures with a small **middle** parameter to fulfil both optimisation targets since it maximises the mass specific stiffness and gives the lowest action. Yet, the **middle** parameter shows this trend only for the mass specific values, the unnormalised stiffness has also the opposing trend for the **middle** parameter (Figure 4.8 b)). The trend reversal is due to a high reduction in mass for small struts, so lightweight construction as a third optimisation goal has a huge impact on this parameter. Otherwise, for the mass specific stiffness the **strut length** shows the largest effect whereas **connection** has the largest effect on the action. For the action and the stiffness, **strut length** and **middle** are the least important parameter, respectively.

As **connection** and **middle** are the two most influential parameters to adjust the action, those two have also the largest interaction. With respect to the mass specific stiffness, the largest interaction is between **connection** and **strut length** since those two have the largest effect on that. From this however, no clear design guideline can be deduced since all three parameters have a strong influence on each other. The only insight from the interaction is that **middle** and **strut length** can be adjust almost independently concerning the stiffness.

Table 4.2: Resulting action (S), mass specific stiffness (E/m) and yield strength ($R_{p0.2}$) for the eight different specimens of the full factorial testing plan with the best compromise solution so far marked in green; 1 and -1 denote to the max and min value of the three geometry parameters middle, connection and strut thickness, respectively; for structure 6 no yield point could be evaluated since the simulation ran only up to 4 % strain

	number	parameter level	S [mJs]	E/m [MPa/g]	$R_{p0.2}$ [MPa]
small	1	-1-1-1	549.35	2.33	0.027
	2	1-1-1	8288.66	3.35	0.486
	3	1 1-1	279002.99	52.07	29.036
	4	-1 1-1	217390.21	28.62	24.705
large	5	-1-1 1	51.96	0.08	0.003
	6	1-1 1	302.60	0.02	-
	7	1 1 1	318111.12	4.39	4.716
	8	-1 1 1	3709.94	0.13	0.031

For the full factorial testing plan a good compromise solution is yielded by the smallest structure with all parameters on minimum (Table 4.2 green). As a proposed optimisation target the quotient of stiffness and action is used and the compromise was selected according to the largest quotient. Maximising this quotient means minimising the action, and thus perfecting the damping, since it is the denominator and at the same time maximising the mass specific stiffness since it is the numerator. The effects for this quotient (Figure 4.8 b)) also confirm the chosen compromise structure since it gets maximised for all three parameters on their respective lowest level. This measure, though, is not ideal due to the large difference in scale which is roughly 10^4 from smallest action to largest action and 10^3 for the mass specific stiffness. But as a first approximation this quotient can be regarded as a good initial measure. It might be desirable for a final optimisation to use weights for the two targets to give them a different importance, resulting then in a scaling of the quotient. The quotient also does not consider the yield strength, which for the compromise structure is the second lowest of all structures where it could be evaluated. Thus, while structure 1 may be the

best compromise in terms of this quotient, the actual applicability is questionable since a yield strength of 0.027 MPa might be too low for load bearing technical applications.

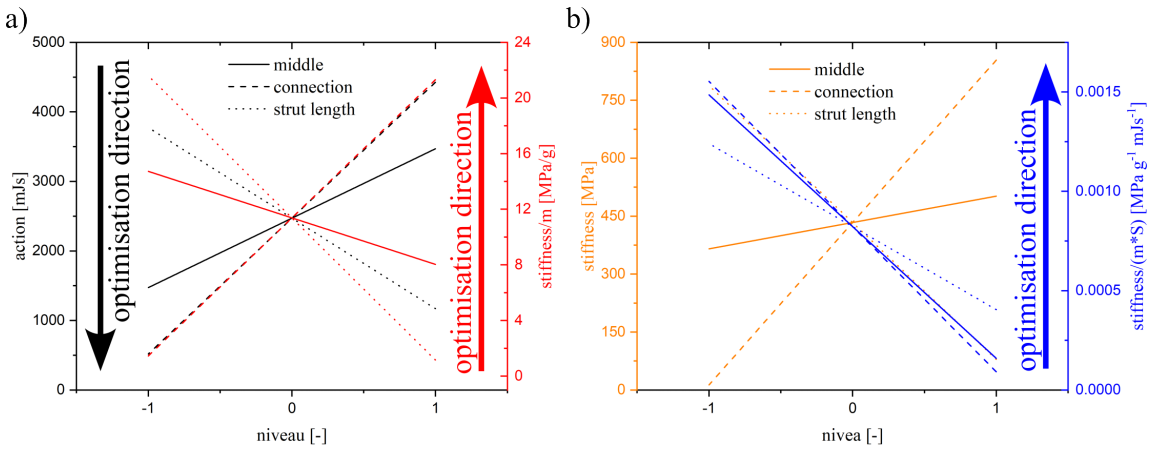

Figure 4.8: Effect plot of the three parameters a) on the two targets action and mass specific stiffness with direction of desired optimisation, b) on unnormalised stiffness and proposed optimisation quotient

The deformation behaviour on the example of structure 1 under oscillation and compression shows maximised stresses in the connection points of the base structures (Figure 4.9) and is representative for all structures. The computed Mieses stresses on the surface are, with 280.5 MPa within the joints, equal the ultimate tensile strength of the SLM aluminium (Figure 3.8). This is an indication, that the structure will potentially fail at the joints already during the first few oscillations. Since the simulations do not include damage, this is necessary to evaluate with experiments. Furthermore, the stresses along the struts is significantly lower, even almost zero in the middle of the strut. Thus, the deformation mechanism is not dominated by a bending of single struts as it is for other porous structures. So the main stability issues arise from the connector points.

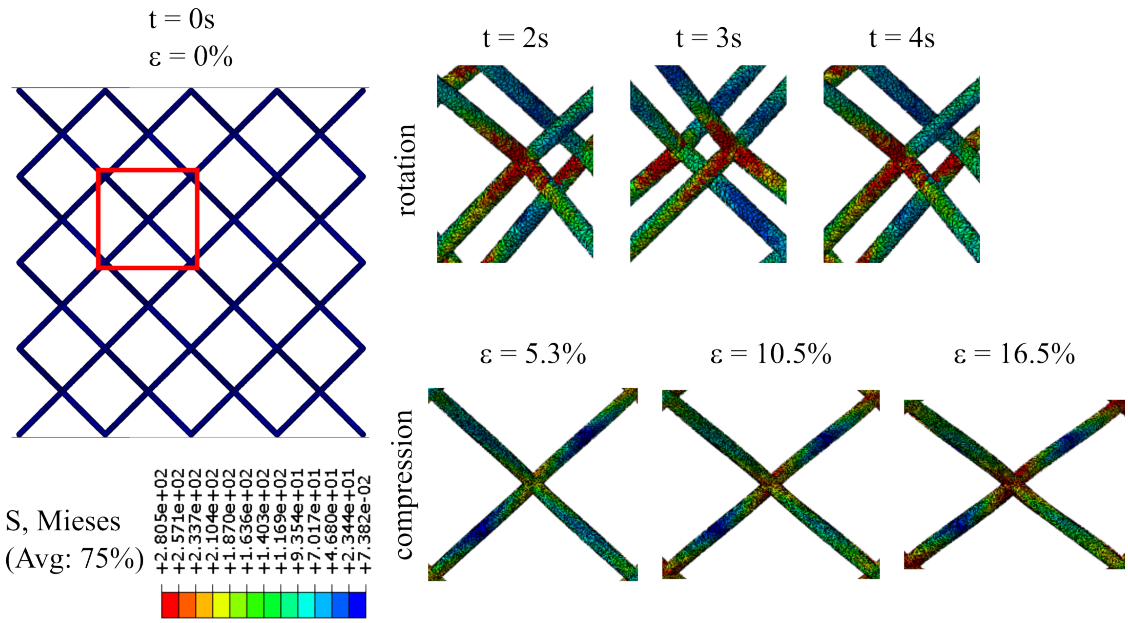

Figure 4.9: Deformation behaviour of structure 1 for rotation and compression at different times or global strains, respectively; for better visibility the images are zoomed in on one structural joint

4.3 Neural Network Training

After the initial investigation, a neural network is trained with adaptive sampling. The sampling algorithm was developed by Janis Mathieu [97] during his master seminar under supervision of Stefan Bronder. He showed for the auxetic data, that the adaptive sampling converges faster to lower test errors for trained neutral network compared to latin hypercube sampling or complete random sampling. Therefore, the adaptive sampling was employed here to keep the number of necessary simulations to a minimum.

In order to keep the consistency, the geometry parameter **angle** was also neglected for the training and optimisation. It also has a minor influence on the resulting action when varied between 90° and 130° (Figure 4.10) as an investigation for different angle on otherwise the best compromise structure from the previous section displays. There is no noteworthy change in the behaviour of the reaction moment when varying the **angle** (Figure 4.10 a)). The apparent best choice for **angle** seems to be around 100°, but the resulting action is only slightly lower than the one for the chosen 109.4° (Figure 4.10 b)). Hence, the optimisation potential concerning this geometry parameter is not significant. Moreover, this kept the necessary time to a minimum because it requires less simulations. If the

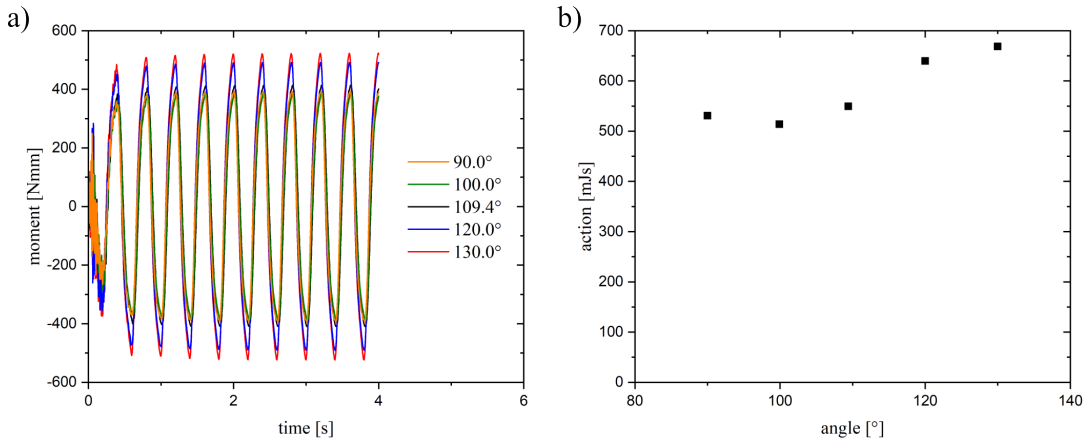

Figure 4.10: a) reaction moments for different values of the geometry parameter angle, b) resulting actions for different values of the geometry parameter angle; all other geometry parameters were chosen according to structure 1 from the previous design space investigation

parameter **angle** were considered, eight additional simulations each for the initial and testing data would have been necessary. Also one extra feature would have to be considered, which usually increases the total number of required training data to give good predictions for the neural network. Thus, the time save by neglecting **angle** is justified due to its small optimisation potential within a range of 50° and the probable best choice being around the selected 109.4°.

The eight structures from the previous section serve as a starting point for initial training of the adaptive sampling. Another eight simulations within the design space are necessary as initial testing points for the adaptive sampler. Since three geometry parameters are adapted, the design space is still displayable as a cuboid, with the initial training data points on the edges and the testing data within the volume (Figure 4.11 initial step). Testing data outside the cuboid are not necessary to study, since it determines the design space of the SLM machine.

The sampling algorithm identifies the worst and second worst regions by evaluating the MAPE on the testing data. It then requests two additional datasets within those regions to further commence the training. The two worst test points are added to the training data as well as one of the generated points within this region, the other generated point serves as a new test point for the region. In this way, the design space is always divided into eight test regions, which are iteratively explored and the information gain from new training points is maximised (Figure 4.11 3rd step and 6th step).

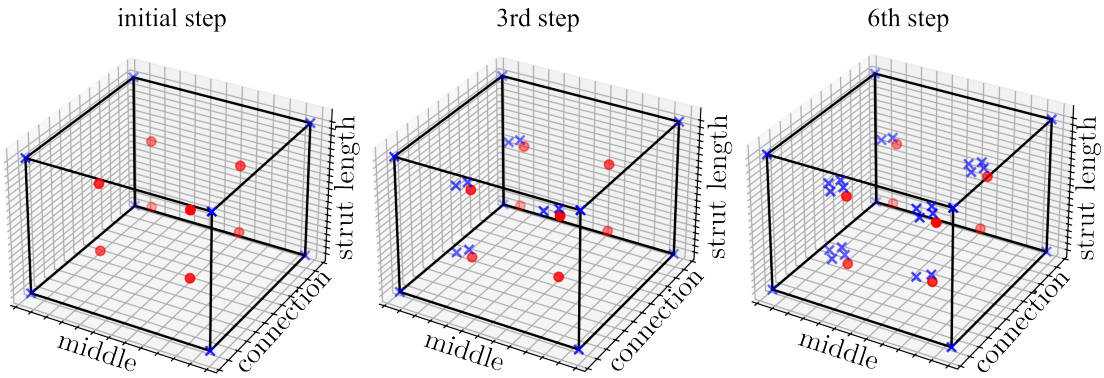

Figure 4.11: Initial training configuration and configuration after three and six training iterations of the adaptive sampling algorithm in the 3D design space; blue x are the training data points, red dots are the test data points

The network architecture was chosen based on the initial 16 simulations, eight from the design space investigation and further eight as the initial test data. Again, the number of hidden layers and neurons per layer were iteratively increased starting from two layers with 10 neurons each. As a result, a network with nine hidden layers, five with 40 neurons and four with 20 neurons per layer, emerged as best performing for the existing data. The SELU activation with the corresponding lecun initialiser was utilised for the network in order to benefit from the self normalising properties. The network in this case is only predicting the resulting action of a geometry parameters combination, thus it predicts only one numerical value, which is relevant for the optimisation.

The network architecture was not reevaluated during the training iterations of the adaptive sampler so as to not introduce more hyperparameters and to keep the adaptive sampling consistent, because with changing network architecture the data composition would also be prone to change. One adaptive sampling iteration consists of initialising, training and evaluating the network and then requesting the new data. With the procedure described above, in each iteration four new datasets are added to the training database. After a total of eight training iterations the average test error has reached an acceptable margin of error of 6.82 % (Figure 4.12 a)). Hence, there were only 36 simulations necessary to reach an average test error below 10 % for predicting the action of the structure. Even though the MAPE is reported here, since it gives a more intuitive understanding and the difference in scale for the target variable are significant, for the training the Huber loss was utilised. This is due to the larger values of this loss and thus the larger gradients, which should speed up the training process.

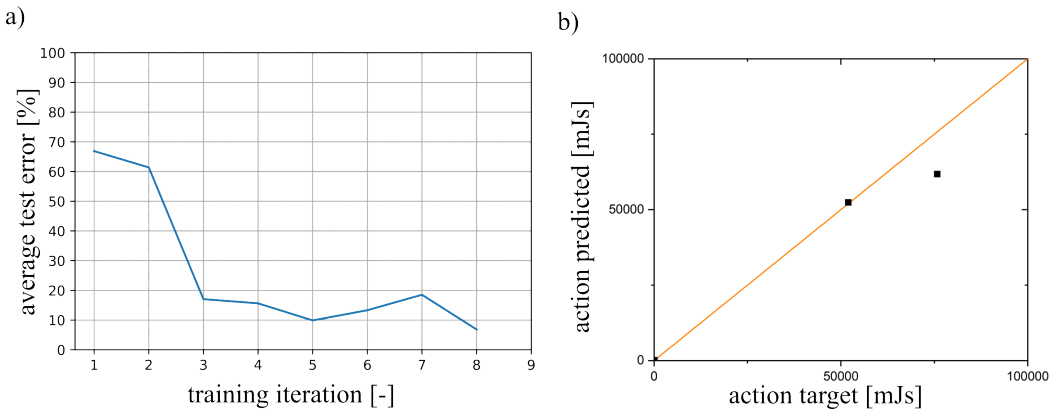

Figure 4.12: a) average test error over the adaptive sampling iterations for the pentamode structures, with each iteration four new datasets are added to the training data; b) predicted over target value of the action for three validation datasets, orange is the straight for a perfect match of both

The finial network for the optimisation was trained on all 44 datasets existent so far to make the best possible use of the available data. As a means to prevent overfitting, three additional simulations on random geometry parameters were done which were used as validation data to introduce an early stopping to the training. Thus the final network for the optimisation achieved a MAPE on the validation data of roughly 7 % (Figure 4.12 b)).

4.4 Optimising the Damping

To find the structure with the best damping capabilities, the surrogate optimisation scheme introduced for the auxetic structures in section 3.4.2 was used. Since there was no preexisting assumption for the surrogate model for the pentamode structures, different polynomial functions were tried out on the simulation data and the fit quality was evaluated using the R^2 score. Models of up to fifth order and different quadratic models were evaluated during this stage. Linear models were neglected because they would be too simplistic and always lead to a minimum on the border of the design space. For the data at hand the function

$$S = ax_0 + bx_0^2 + cx_1 + dx_1^2 + ex_2 + fx_2^2 + gx_0x_1x_2 + h \tag{4.1}$$

provided the best fit with $R^2 \approx 0.85$. The parameters a to h are curve fitting parameters, S is the target variable, in this case the action and $\mathbf{x} = (x_0, x_1, x_2)$ is the feature vector with the three geometry parameters to be optimised. Curiously, this surrogate model is similar to the one for the auxetic structures. Hence,

it might be possible that a quadratic surrogate model is applicable for multiple porous structures assembled periodically from a parametrised unit cell.

The multidimensional minimisation is also sensitive to the choice of the starting point. Therefore, ten different starting points within the design space were selected at random. After the ten minimisations, the one yielding the lowest action was selected as the global minimum. This resulted in a structure with minimal **connection** and **middle** and almost maximal **strut length** (Figure 4.13). The predicted value from the network with 84.29 mJ s differs only slightly from the value calculated from the simulation with 86 mJ s, which amounts to a 2 % error.

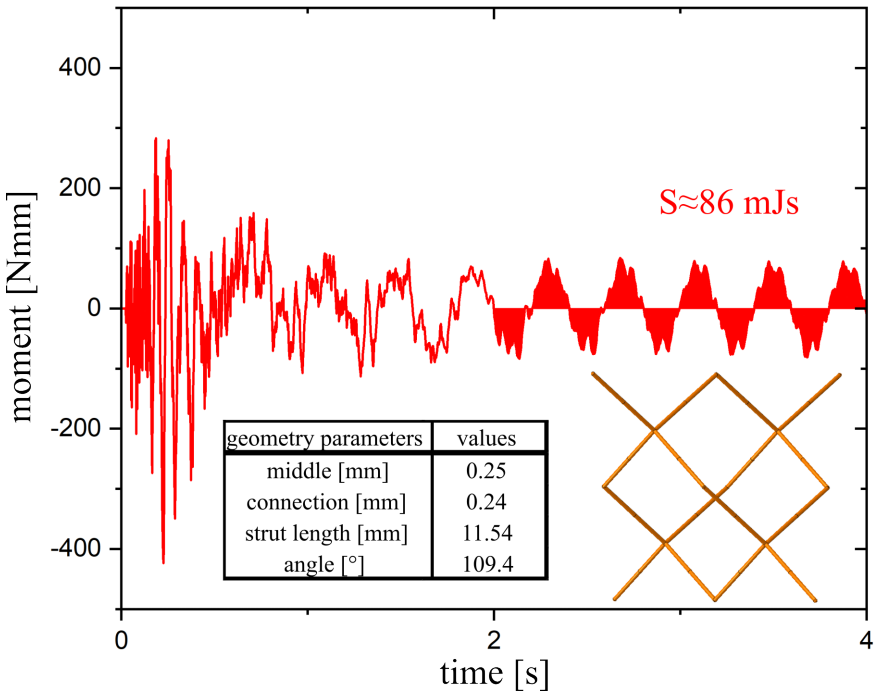

Figure 4.13: Resulting reaction moment over time for the damping optimised structure with corresponding unit cell, geometry parameters and calculated action S

For further evaluation, a compression experiment on the optimised structure was simulated. As already expected from the results of the design space investigation, this structures displays a very low stiffness of 0.06 MPa (Figure 4.14). Even though this structures has a very small estimated mass of 0.74 g, the mass specific stiffness is still low with 0.08 MPa g^{-1}. From the images at two different global strains it becomes apparent, that again the main deformation happens within

the joints of the structure and not due to a bending of single struts. The pseudo-elastic behaviour is also visible within those structures because there are already plastic deformations within the joints even in the first, linear deformation regime of the pentamode structures. Thus, the structure even though it displays a high damping, an application within a technical product might prove difficult and is strongly dependent on the applied load. This once again shows the necessity of a compromise solution as well as the clear definition of the application requirements and thereby a clear definition of the optimisation targets and constraints.

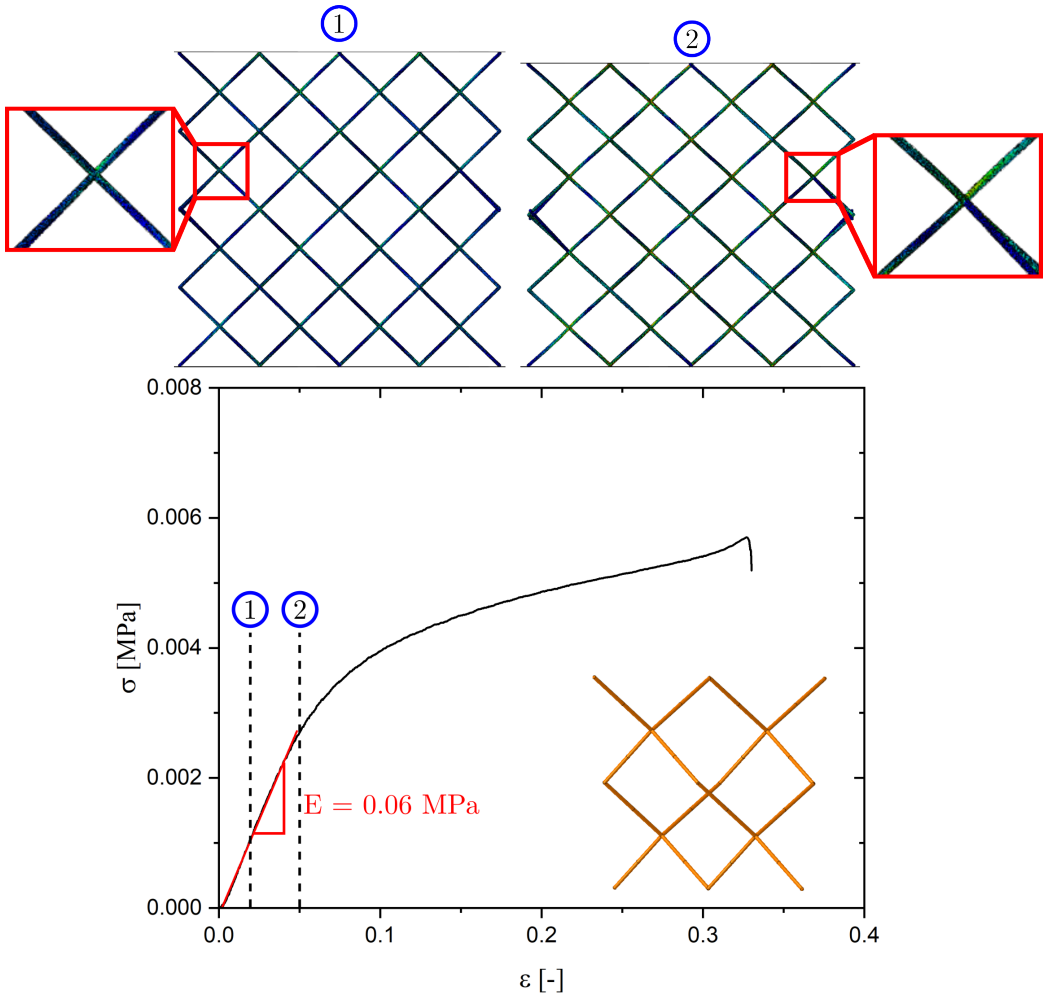

Figure 4.14: Stress-strain curve of the optimised structure with linear fit to evaluate the stiffness E and compression states 1 and 2 for two different global strains

4.5 Summarised Findings

This chapter was dedicated to the optimisation of the damping properties of pentamode structures. The investigation purely with simulations resulted in the following key aspects.

- Designing a pentamode structure with perfect damping and yet enough structural stiffness to keep its structural integrity is difficult because the targets require contrasting geometry parameters. Again, it is important to find a compromise solution similar as for the auxetics.
- The design space investigation displays the huge potential for these structures even when only three out of four identified geometry parameters were varied.
- For the mass specific stiffness, the influence of the **middle** parameter on the optimisation is aligned for both target values.
- The parameter **connection** is the most influential one for the optimisation of the damping, yet is also responsible for the structural stability. Small connector points renders the resulting structure weaker.
- The smallest possible structure within the chosen design space yields the best compromise for an unweighted quotient of mass specific stiffness and action.
- The parameter **angle** has a negligible influence on the damping properties of the pentamode structures.
- A neural network was trained using adaptive sampling. Thus, the amount of necessary simulations was kept very low with only 44 in total and already achieved a MAPE of roughly 7 % for prediction the action.
- The resulting structure only optimised for the damping capabilities is almost identical to structure 5 from the design space investigation and has a comparable action. It only has slightly shorter struts.

5

Final Thoughts and Discussion

5.1 Conclusion

The aim of this work was to establish a new and faster method to optimise microstructures without the extensive need of experiments and simulations. The basic concept, utilising and combining machine learning techniques, has already been employed in many fields of engineering and was also successfully implemented for this task. It provides a means to replace simulations or experiments by simply predicting the desired properties. Therefore, the time saved is directly linked with either the number of simulations, their duration, the time for specimen production, the time necessary for the experiments and their evaluation or a combination of the above.

The work flow was established and perfected on the example of **modified 3D re-entrant honeycomb auxetic structures** with five identified geometry parameters to describe the unit cell. There is of course the possibility to introduce even more parameters but for the sake of simplicity some symmetries within the cells were assumed. The superiority of the modified auxetics over the unmodified 3D unit cell was demonstrated on one example. The modified version is capable of withstanding larger deformation without losing its stiffness and thus has also a higher PCS and plateau compared to the purely auxetic unit cell. This enhances also the EAC and makes the structure more stable after an initial deformation which can become of more interest when there is a small crash and the structure is still usable for its protective properties.

Since finding a representative volume element is an especially difficult topic for cellular materials a first investigation was launched in order to find the RVE for the auxetics at hand. Even though the PCS and PS seem more stable for structures with at least $5 \times 5 \times 3$ unit cells, the chose RVE of $3 \times 3 \times 3$ unit

cells still gives a good approximation of the macroscopic behaviour and is within the variance of the single experiments. The larger RVE is also not feasible for simulations on the micostructural scale. Even with the smaller RVE one FE simulation of the microstructure can have well above 10^6 elements and hence a simulation time ranging from 24 to 96 hours for just one simulations. From this, it becomes directly apparent that an optimisation of the structure, which would require a large amount of simulations would take a few months. For example if all five geometry parameters were considered and each parameter was just investigated at three levels, it would already require 243 simulations for a full factorial evaluation, which would amount to at least 243 days just for all simulations to finish. If parallelisation were applied and 5 simulations could be run at once, this would still be approximately 50 days. Also this is still a very coarse grid and would only give some insight into the design space, especially if this space is not strongly confined or the behaviour for the parameters is not quadratic.

Yet, a full factorial design space investigation nevertheless can give valuable insight into the design space. Even if the assumprion of linearity is not necessarily given, some tendencies for the behaviour can be extracted and also particularly if the design target consists of multiple objectives on which the parameters have contrasting influence. For the auxetics the minimisation of the Poisson's ratio and the maximisation of the mass specific energy absorption capacity proved to be opposing to each other. Therefore, a compromise solution needed to be found and the optimisation target formulated accordingly as the product of both. Additionally, for simulations during this step of the optimisation it is easily possible to perform experiments to either validate the simulations or find errors with either the setup or the material model. In particular, specimens produced by additive manufacturing can prove to have different material parameters, which are strongly dependent on the procedure itself. Although, the SLM specimens showed little variance within the produced batches, a small change in production however, changed the material properties extensively. Another reason for discrepancies between experiment and simulations is on the one hand a different deformation mechanism in simulation and experiment and on the other hand the neglect of damage for the simulations, which occurs during the compression experiments.

As mentioned, the FE simulations have high durations and thus saving numbers of simulations means saving time and cost for later production of such structures. ML algorithms and in the case of this work neural networks are capable of making predictions within the fraction of a second. Consequently, only a few simulations can be used to train a neural network to predict the desired outcome and use this network for the optimisation instead of simulating every parameter combination. At this point, the numerical representation of the microstructure

becomes important. It is desirable to achieve a complete representation with as few features as possible since the less features the less training data is required by the neural network to learn an acceptable approximation of the correlations between features and target. Then again, the representation needs to allow enough variance in the model and nor confine the structure too strongly so there is a real possibility for optimisation potential to be used. Always with the ulterior motive of keeping the number of simulations as low as possible, different data sampling strategies were investigated on the auxetic structures, which at the end lead to 178 simulations that were used for the training of the neural network and the final optimisation. Nevertheless, Bronder et al. [21] showed that 88 simulations are already sufficient to reach an optimised structure. This means a reduction of 155 simulations compared to the full factorial design with 5 parameters on 3 levels each, so a total time save of roughly 155 days or with 5 simulations running in parallel 31 days. Of course, the neural network training is also a time consuming process, but even with a four-fold cross validation this takes only approximately one day. So its over a month of time saved to find an optimised structure for the auxetics.

The optimisation itself is handled by a quasi newton procedure, which is responsible for finding minima in multidimensional polynomials. Therefore, a surrogate model function is fitted to the relation between geometry parameters and optimisation target values. This can be regarded as another, very basic kind of ML tool, which makes the whole optimisation procedure a combination of different ML algorithms. The question, why not use the neural network output directly for minimisation may arise, since a multidimensional polynomial curve fit produces again some error. First, the surrogate model presents the opportunity to incorporate the already existing simulation data, which in this case is regarded as the ground truth and thus has no error for this purpose. Second, minimising a polynomial function, which can be selected according to the R^2 value can also provide a more intuitive understanding of the data and the correlation between geometry parameters and target values. Third, the error of the curve fit is well within the manufacturing tolerance of the SLM procedure. So it is more beneficial to reuse the simulation data and make a small error with the curve fitting than neglecting this data and only use the network predictions which are also prone to errors. Also this technique can potentially lessen the iterations to reach a minimum and since the polynomial in this case was quadratic, the found minimum is, with a high probability, the global minimum within the design space.

The prediction of the two trained neural networks, the one for the stress-strain behaviour and the other one for the Poisson's ratio, were validated with a simulation and were found to give a very close match to the values from the simulation. Unfortunately, the material model for the simulations on which the networks

were trained on needed correction, so the simulation data was not a good match for the actual experiments and a complete do over of the simulations would have consumed too much time. However, the optimisation is still valid since the error for all simulations within the material model is constant. After a recalibration with new tensile specimens, the experiments and simulations were a much better match. So even if the ground truth data for the network training was faulty, the established optimisation procedure was validated to yield good results within a much smaller time frame than without ML tools.

The whole optimisation procedure was then transferred to another metamaterial structure, the **pentamodes**. The primary objective with these structures is to maximise the damping capabilities for transverse waves while providing enough stiffness to keep the structural integrity. The damping capabilities in this case was measured as the action, which is the integrated area under the reaction moments measured on the bottom of the structure while an oscillation is induced on the topside. Due to time constraints, the pentamode investigation was done purely with simulations, which is why the RVE was just assumed to be of $2 \times 2 \times 2$ unit cells. But as one unit cell consists of four pentamode base structures, this was deemed a sufficient size, which can still be simulated within a feasible time window. The complex structure, especially the very small joints need a fine mesh, which lead to element numbers well above 10^6. This fine mesh and the simulation duration were the reasons why those structures were meshed using linear elements.

In order to optimise both targets, damping and structural stability, two different deformation modes of the pentamode structures need to be investigated, which means two different types of simulations. Again, due to time constraints, only the dataset to train a neural network for the prediction of the damping was done. This means avoiding the necessary compression simulations to train a neural network to predict the mass specific stiffness and yield strength. The full factorial investigation of the design space however, was performed on both deformation modes, rotation and compression. Surprisingly, not all parameters are of contrasting influence on the optimisation for the two targets action and mass specific stiffness. Nevertheless, this is only true in case of the mass specific stiffness, since the amount of mass reduction is significant when the middle parameter of these structures is small. This means the third governing objective for almost all constructions, reducing mass and used material, has a significant influence on the optimisation of these structures, where for auxetics it had only a peripheral role but did not change the behaviour towards one of the geometry parameters. The yield strength as yet another optimisation target can also be considered, but since a higher mass specific stiffness leads to an increased yield strength, optimising the stiffness should be sufficient and the yield strength can be applied in case there are constraints with certain applications.

Further, the investigation of the design space makes the necessity of a compromise solution apparent since the behaviour of the other two geometry parameters has a contrasting influence on the optimisation for the two targets action and mass specific stiffness. The maximisation of the quotient of stiffness and action is a first viable measure since smaller actions and larger stiffnesses lead to a growing quotient. Meanwhile, a more sophisticated measure, such as a weighted quotient might be necessary to compensate for the large scale differences between the minimal and maximal action.

Starting from the outer edges of the design space, a neural network was designed to predict the action of the structures based on their geometry parameter composition for the three parameters middle, connection and strut length. The adaptive learning scheme, developed on the auxetics was used and achieved good prediction results with just 44 simulations in total. Here, one simulation of a structure took about 24 to 48 hours with just a few exceptions that were faster. So in total the simulations needed approximately 11 days with four simulations running in parallel. Compared to a full factorial design with only these three parameters on four levels 64 simulations would be required, which already saves 20 simulations with the neural network approach. Moreover, the structures are not easy to mesh and hence each non necessary simulation also prevents possible meshing and calculation problems. This is especially true for the compression simulations, which also suffered sometimes from dynamic influences, which had to be remedied by increasing the virtual deformation time or reducing the total amount of deformation for some structures of the full factorial design. Thus, saving simulations in this case means not only a time save of a day per four simulations but also reduces possible complications with the simulations of the structures.

The optimisation, at least for the damping was successful, yet the result was already obvious from the design space investigation. The largest structure with the minimal connection and middle parameter has the smallest action, and the optimisation with the neural network yielded almost the same structure. The discrepancy can be regarded as a result of the curve fit to the multidimensional polynomial, which produces some small error in the approximation. Yet, the tendency is clear and the neural network prediction and validation simulation are in good accordance. Therefore, the optimisation scheme was successfully transferred to the pentamode structures.

5.2 Future Work

Optimisation of microstructures is ongoing research and even though the resulting scheme works successfully there are still many more angles and investigations to consider. For the **auxetics** the next step is investigating the behaviour under dynamic loading, which was already partly begun in [46] and introducing damage behaviour to the simulations. Towards that end, the master thesis of Alexander Engel [41] already provides a cornerstone. Utilising macroscopic tensile specimens to identify parameters for a damage model was proven to not work. Therefore, microtensile experiments are necessary to identify the damage parameters for the struts in the auxetic structures.

Also, when considering the design aspect of larger components, a homogenised material model for the auxetics is necessary, where neural networks could easily be applied. Therefore, other loading modes need to be investigated, especially multiaxial loading cases or yield surfaces. Yet, it is easily possible to train and use a neural network to predict material behaviour of a homogenised material model instead of trying to describe the model with phenomenological equations which also might be next to impossible in the case of complex microstructures.

Another important consideration is the change of the base material. All investigations presented in this work were done on the assumption of specimens produced out of AlMg10Si powder on an SLM machine. So the question what happens when the metal or even the material class is changed is important to study. Leading to the following exemplary research questions that might arise and which are another step towards a homogenised material model:

- If the metallic powder is changed, what happens to the structural properties?
- Can simply some sort of scaling factor be applied?
- How important for the overall behaviour is the structure and how important the base material?
- What happens when the material class is changed to polymers, ceramics or hybrid materials?
- If it is just a matter of a scaling factor when exchanging for example the metallic powder, would it be possible to predict the behaviour of the structures based on macroscopic material properties such as Young's modulus in advance without actually producing the structures?

Moving on to the future work concerning the **pentamode structures**, there is still a lot more ground to cover. First, an experimental investigation of the design space and the RVE need to be launched in order to validate the results obtained from the simulations. Second, a neural network needs to be trained to predict the mass specific stiffnesses in order to finalise the optimisation, which in turn needs to be verified by experiments. Third, the current investigation includes only three out of the four identified geometry parameters. Thus, an investigation on the influence of the angle between the struts is required. Fourth, it is of interest to study the behaviour under different stimulation frequencies since this is also a parameter of concern to a potential user.

All the above are just direct consequences of the time constraint and are necessary steps to achieve comparability with the investigation of the auxetics. But to take the idea further, again the investigation of different base materials is the next large step towards an applicable model. Also the influence of damage is important to examine, especially for a long term use as a dampening module that is subject to many load cycles. So the longevity, the resulting degradations of the material behaviour, if any and the connected degradation of the dampening properties and structural stability need to be investigated. Also implementing damage into the compression simulations might be necessary, if the experiments yield results that differ largely from the simulations. As the pentamode structures are thought of as a mechanical dampening module within this work, it is also of interest to study the behaviour under combined oscillating loading cases of compressive and transversal waves for example.

Finally, an optimised pentamode structure for stiffness and damping, which is experimentally validated, provides a good starting structure for the further investigations of longevity, different materials and such. The same applies to the optimised version of the modified auxetics. Both structures provide a sensible initial point for an all encompassing study of the structures.

Bibliography

[1] Abbassi, F., Belhadj, T., Mistou, S., and Zghal, A. Parameter identification of a mechanical ductile damage using artificial neural networks in sheet metal forming. *Materials & Design 45* (2013), 605–615.

[2] Abueidda, D. W., Almasri, M., Ammourah, R., Ravaioli, U., Jasiuk, I. M., and Sobh, N. A. Prediction and optimization of mechanical properties of composites using convolutional neural networks. *Composite Structures 227* (2019), 111264.

[3] Aggarwal, C. C. *Machine learning for text*, vol. 848. Springer, 2018.

[4] Aggarwal, C. C., et al. *Neural networks and deep learning*, vol. 10. Springer, 2018.

[5] Albon, C. *Machine learning with python cookbook: Practical solutions from preprocessing to deep learning.* " O'Reilly Media, Inc.", 2018.

[6] Alderson, A., and Alderson, K. Auxetic materials. *Proceedings of the Institution of Mechanical Engineers, Part G: Journal of Aerospace Engineering 221*, 4 (2007), 565–575.

[7] Alderson, K., Alderson, A., Smart, G., Simkins, V., and Davies, P. Auxetic polypropylene fibres: Part 1-manufacture and characterisation. *Plastics, Rubber and Composites 31*, 8 (2002), 344–349.

[8] Alderson, K., Kettle, A., Neale, P., Pickles, A., and Evans, K. The effect of the processing parameters on the fabrication of auxetic polyethylene. *Journal of materials science 30*, 16 (1995), 4069–4075.

[9] Alderson, K. L., Simkins, V. R., Coenen, V. L., Davies, P. J., Alderson, A., and Evans, K. E. How to make auxetic fibre reinforced composites. *Physica Status Solidi (b) 242*, 3 (2009), 509–518.

[10] Allaire, G., Jouve, F., and Toader, A.-M. A level-set method for shape optimization. *Comptes Rendus Mathematique 334*, 12 (2002), 1125–1130.

[11] Allaire, G., Jouve, F., and Toader, A.-M. Structural optimization using sensitivity analysis and a level-set method. *Journal of computational physics 194*, 1 (2004), 363–393.

[12] Almgren, R. An isotropic three-dimensional structure with poisson's ratio =-1. *J. Elast. 15* (1985), 427–427.

[13] Altenbach, H. *Kontinuumsmechanik*. Springer, 2018.

[14] Berger, L., Eoin, H., Cardoso, M. J., and Ourselin, S. An adaptive sampling scheme to efficiently train fully convolutional networks for semantic segmentation. In *Annual Conference on Medical Image Understanding and Analysis* (2018), Springer, pp. 277–286.

[15] Berk, R. A., et al. *Statistical learning from a regression perspective*, vol. 14. Springer, 2008.

[16] Bezazi, A., and Scarpa, F. Mechanical behaviour of conventional and negative poisson's ratio thermoplastic polyurethane foams under compressive cyclic loading. *International Journal of Fatigue 29*, 5 (2007), 922 – 930.

[17] Bianchi, M., Scarpa, F., and Smith, C. Shape memory behaviour in auxetic foams: Mechanical properties. *Acta Materialia 58*, 3 (2010), 858 – 865.

[18] Brillinger, M., Wuwer, M., Hadi, M. A., and Haas, F. Energy prediction for cnc machining with machine learning. *CIRP Journal of Manufacturing Science and Technology 35* (2021), 715–723.

[19] Bronder, S., Adorna, M., Fíla, T., Koudelka, P., Falta, J., Jiroušek, O., and Jung, A. Hybrid auxetic structures: Structural optimization and mechanical characterization. *Advanced Engineering Materials* (2021), 2001393.

[20] Bronder, S., Diebels, S., and Jung, A. Neural networks for structural optimisation of mechanical metamaterials. *PAMM 20*, 1 (2021), e202000238.

[21] Bronder, S., Herter, F., Bähre, D., and Jung, A. Optimized design for modified auxetic structures based on a neural network approach. *Materials Today Communications 32* (2022), 103931.

[22] Bronder, S., Herter, F., Röhrig, A., Bähre, D., and Jung, A. Design study for multifunctional 3d re-entrant auxetics. *Advanced Engineering Materials* (2022), 2100816.

[23] Broyden, C. G. The convergence of a class of double-rank minimization algorithms: 2. the new algorithm. *IMA journal of applied mathematics 6*, 3 (1970), 222–231.

[24] Bückmann, T., Thiel, M., Kadic, M., Schittny, R., and Wegener, M. An elasto-mechanical unfeelability cloak made of pentamode metamaterials. *Nature communications 5*, 1 (2014), 1–6.

[25] Byrd, R., Lu, P., Nocedal, J., and Zhu, C. A limited memory algorithm for bound constrained optimization. *SIAM Journal on Scientific Computing 16*, 5 (1995), 1190–1208.

[26] Caddock, B., and Evans, K. Negative poisson ratios and strain-dependent mechanical properties in arterial prostheses. *Biomaterials 16*, 14 (1995), 1109–1115.

[27] Challapalli, A., Patel, D., and Li, G. Inverse machine learning framework for optimizing lightweight metamaterials. *Materials & Design 208* (2021), 109937.

[28] Chawla, K. K., and Meyers, M. *Mechanical behavior of materials*. Prentice Hall, 1999.

[29] Chu, W., Ho, P. S., and Li, W. An adaptive machine learning method based on finite element analysis for ultra low-k chip package design. *IEEE Transactions on Components, Packaging and Manufacturing Technology 11*, 9 (2021), 1435–1441.

[30] Clare, A. T., Chalker, P. R., Davies, S., Sutcliffe, C. J., and Tsopanos, S. Selective laser melting of high aspect ratio 3d nickel–titanium structures two way trained for mems applications. *International Journal of Mechanics and Materials in Design 4*, 2 (2008), 181–187.

[31] Clarke, J., Duckett, R., Hine, P., Hutchinson, I., and Ward, I. Negative poisson's ratios in angle-ply laminates: theory and experiment. *Composites 25*, 9 (1994), 863–868.

[32] Das, S. Physical aspects of process control in selective laser sintering of metals. *Advanced Engineering Materials 5*, 10 (2003), 701–711.

[33] Dassault Systèmes Simulia Corp. *ABAQUS/Standard User's Manual, Version 6.10*, 2010.

[34] Dauphin, Y. N., Pascanu, R., Gulcehre, C., Cho, K., Ganguli, S., and Bengio, Y. Identifying and attacking the saddle point problem in high-dimensional non-convex optimization. *Advances in neural information processing systems 27* (2014).

[35] Davis, P. J., and Rabinowitz, P. *Methods of numerical integration*. Courier Corporation, 2007.

[36] DIN. Din en iso 6892-1. *Metallische Werkstoffe—Zugversuch—Teil 1: Prüfverfahren bei Raumtemperatur* (2017).

[37] Duchi, J., Hazan, E., and Singer, Y. Adaptive subgradient methods for online learning and stochastic optimization. *Journal of machine learning research 12*, 7 (2011).

[38] Dudek, K., Drzewiński, A., and Kadic, M. Self-rotating 3d chiral mechanical metamaterials. *Proceedings of the Royal Society A 477*, 2251 (2021), 20200825.

[39] Durmaz, A. R., Müller, M., Lei, B., Thomas, A., Britz, D., Holm, E. A., Eberl, C., Mücklich, F., and Gumbsch, P. A deep learning approach for complex microstructure inference. *Nature communications 12*, 1 (2021), 1–15.

[40] Eichler, H. J., and Eichler, J. *Laser: Bauformen, Strahlführung, Anwendungen*. Springer-Verlag, 2015.

[41] Engel, A. Einsatz von Schädigungsmodellen zur Verbesserung der Materialmodellierung modifizierter auxetischer Strukturen. Master's thesis, Saarland University, 2022.

[42] Evans, K. E., Nkansah, M., and Hutchinson, I. Auxetic foams: modelling negative poisson's ratios. *Acta metallurgica et materialia 42*, 4 (1994), 1289–1294.

[43] Evans, K. E., Nkansah, M., Hutchinson, I., and Rogers, S. Molecular network design. *Nature 353*, 6340 (1991), 124–124.

[44] Fabbrocino, F., Amendola, A., Benzoni, G., and Fraternali, F. Seismic application of pentamode lattices. *Ing. Sismica 33*, 1-2 (2016), 62–70.

[45] Feng, S., Zhou, H., and Dong, H. Using deep neural network with small dataset to predict material defects. *Materials & Design 162* (2019), 300–310.

[46] Fíla, T., Koudelka, P., Falta, J., Zlámal, P., Rada, V., Adorna, M., Bronder, S., and Jiroušek, O. Dynamic impact testing of cellular solids and lattice structures: Application of two-sided direct impact hopkinson bar. *International Journal of Impact Engineering* (2021), 103767.

[47] Fletcher, R. A new approach to variable metric algorithms. *The computer journal 13*, 3 (1970), 317–322.

[48] Foster, L., Peketi, P., Allen, T., Senior, T., Duncan, O., and Alderson, A. Application of auxetic foam in sports helmets. *Applied Sciences 8*, 3 (2018), 354.

[49] Frolich, L., Labarbera, M., and Stevens, W. Poisson's ratio of a crossed fibre sheath: the skin of aquatic salamanders. *Journal of Zoology 232*, 2 (1994), 231–252.

[50] Gareth, J., Daniela, W., Trevor, H., and Robert, T. *An introduction to statistical learning: with applications in R*. Spinger, 2013.

[51] Gauch Jr, H. G., and Gauch, H. G. *Scientific method in practice*. Cambridge University Press, 2003.

[52] Géron, A. *Hands-on machine learning with Scikit-Learn, Keras, and TensorFlow: Concepts, tools, and techniques to build intelligent systems.* " O'Reilly Media, Inc.", 2019.

[53] Gibson, L. J., and Ashby, M. Mf, cellular solids: structure and properties.

[54] Glorot, X., and Bengio, Y. Understanding the difficulty of training deep feedforward neural networks. In *Proceedings of the thirteenth international conference on artificial intelligence and statistics* (2010), JMLR Workshop and Conference Proceedings, pp. 249–256.

[55] Goldfarb, D. A family of variable-metric methods derived by variational means. *Mathematics of computation 24*, 109 (1970), 23–26.

[56] Goodfellow, I., Bengio, Y., and Courville, A. *Deep learning*. MIT press, 2016.

[57] Goodfellow, I. J., Vinyals, O., and Saxe, A. M. Qualitatively characterizing neural network optimization problems. *arXiv preprint arXiv:1412.6544* (2014).

[58] Gorodtsov, V., and Lisovenko, D. Auxetics among materials with cubic anisotropy. *Mechanics of Solids 55*, 4 (2020), 461–474.

[59] Grednev, S. Dealing with scarce data inpredicting stress-strain relationshipsfor auxetic structures - comparison of ml algorithms -. Master's thesis, Saarland University, 2022.

[60] Grima, J. N., and Evans, K. E. Auxetic behavior from rotating squares. *Journal of Materials Science Letters 19*, 17 (2000), 1563–1565.

[61] Harrell, F. E. J. *Regression modeling strategies: with applications to linear models, logistic regression, and survival analysis*, 2 ed., vol. 608. Springer, 2015.

[62] Hastie, T., Tibshirani, R., and Friedman, J. The elements of statistical learning: data mining, inference, and prediction. springer series in statistics. *Springer New York* (2009).

[63] Hedayati, R., Leeflang, A., and Zadpoor, A. Additively manufactured metallic pentamode meta-materials. *Applied Physics Letters 110*, 9 (2017), 091905.

[64] Hennebold, C., Klöpfer, K., Lettenbauer, P., and Huber, M. Machine learning based cost prediction for product development in mechanical engineering. *Procedia CIRP 107* (2022), 264–269.

[65] Herakovich, C. T. Composite laminates with negative through-the-thickness poisson's ratios. *Journal of Composite Materials 18*, 5 (1984), 447–455.

[66] Hornik, K., Stinchcombe, M., and White, H. Multilayer feedforward networks are universal approximators. *Neural networks 2*, 5 (1989), 359–366.

[67] Hu, W., Cao, X., Zhang, X., Huang, Z., Chen, Z., Wu, W., Xi, L., Li, Y., and Fang, D. Deformation mechanisms and mechanical performances of architected mechanical metamaterials with gyroid topologies: Synchrotron x-ray radiation in-situ compression experiments and 3d image based finite element analysis. *Extreme Mechanics Letters 44* (2021), 101229.

[68] Huang, C., and Chen, L. Negative poisson's ratio in modern functional materials. *Advanced Materials 28*, 37 (2016), 8079–8096.

[69] Hyndman, R. J., and Koehler, A. B. Another look at measures of forecast accuracy. *International journal of forecasting 22*, 4 (2006), 679–688.

[70] Igual, L., and Seguí, S. *Introduction to Data Science: A Python Approach to Concepts, Techniques and Applications*. Spinger, 2017.

[71] Imbalzano, G., Linforth, S., Ngo, T. D., Lee, P. V. S., and Tran, P. Blast resistance of auxetic and honeycomb sandwich panels: Comparisons and parametric designs. *Composite Structures 183* (2018), 242–261.

[72] Ioffe, S., and Szegedy, C. Batch normalization: Accelerating deep network training by reducing internal covariate shift. In *International conference on machine learning* (2015), PMLR, pp. 448–456.

[73] Jiang, Y., Liu, Z., Matsuhisa, N., Qi, D., Leow, W. R., Yang, H., Yu, J., Chen, G., Liu, Y., Wan, C., et al. Auxetic mechanical metamaterials to enhance sensitivity of stretchable strain sensors. *Advanced Materials 30*, 12 (2018), 1706589.

[74] Kadic, M., Bückmann, T., Stenger, N., Thiel, M., and Wegener, M. On the practicability of pentamode mechanical metamaterials. *Applied Physics Letters 100*, 19 (2012), 191901.

[75] Kadic, M., Milton, G. W., van Hecke, M., and Wegener, M. 3d metamaterials. *Nature Reviews Physics 1*, 3 (2019), 198–210.

[76] Kim, B., Lee, S., and Kim, J. Inverse design of porous materials using artificial neural networks. *Science advances 6*, 1 (2020), eaax9324.

[77] Kingma, D. P., and Ba, J. Adam: A method for stochastic optimization. *arXiv preprint arXiv:1412.6980* (2014).

[78] Klambauer, G., Unterthiner, T., Mayr, A., and Hochreiter, S. Self-normalizing neural networks. *Advances in neural information processing systems 30* (2017).

[79] Körner, C., and Liebold-Ribeiro, Y. A systematic approach to identify cellular auxetic materials. *Smart Materials and Structures 24*, 2 (2014), 025013.

[80] Krakhmalev, P., and Yadroitsev, I. Microstructure and properties of intermetallic composite coatings fabricated by selective laser melting of ti–sic powder mixtures. *Intermetallics 46* (2014), 147–155.

[81] Kubat, M., and Kubat. *An introduction to machine learning*, vol. 2. Springer, 2017.

[82] Kuhn, M., Johnson, K., et al. *Applied predictive modeling*, vol. 26. Springer, 2013.

[83] Kushner, H. J. A New Method of Locating the Maximum Point of an Arbitrary Multipeak Curve in the Presence of Noise. *Journal of Basic Engineering 86*, 1 (03 1964), 97–106.

[84] Lakes, R. Foam structures with a negative poisson's ratio. *Science 235* (1987), 1038–1040.

[85] Lakes, R. No contractile obligations. *Nature 358*, 6389 (1992), 713.

[86] Lakes, R. Design considerations for materials with negative poisson's ratios. *Journal of Mechanical Design 115*, 4 (1993), 696–700.

[87] Lakes, R., and Elms, K. Indentability of conventional and negative poisson's ratio foams. *Journal of Composite Materials 27*, 12 (1993), 1193–1202.

[88] LeCun, Y. A., Bottou, L., Orr, G. B., and Müller, K.-R. Efficient backprop. In *Neural networks: Tricks of the trade*. Springer, 2012, pp. 9–48.

[89] Lees, C., Vincent, J. F., and Hillerton, J. E. Poisson's ratio in skin. *Bio-medical materials and engineering 1*, 1 (1991), 19–23.

[90] Li, R., Liu, J., Shi, Y., Wang, L., and Jiang, W. Balling behavior of stainless steel and nickel powder during selective laser melting process. *The International Journal of Advanced Manufacturing Technology 59*, 9 (2012), 1025–1035.

[91] Lim, T.-C. Thermal stresses in auxetic plates and shells. *Mechanics of Advanced Materials and Structures 22*, 3 (2015), 205–212.

[92] Liu, R., Kumar, A., Chen, Z., Agrawal, A., Sundararaghavan, V., and Choudhary, A. A predictive machine learning approach for microstructure optimization and materials design. *Scientific reports 5*, 1 (2015), 1–12.

[93] Liu, Y., and Zhang, X. Metamaterials: a new frontier of science and technology. *Chemical Society Reviews 40*, 5 (2011), 2494–2507.

[94] Lookman, T., Balachandran, P. V., Xue, D., and Yuan, R. Active learning in materials science with emphasis on adaptive sampling using uncertainties for targeted design. *npj Computational Materials 5*, 1 (2019), 1–17.

[95] Malik, A., Abendroth, M., Hütter, G., and Kiefer, B. A hybrid approach employing neural networks to simulate the elasto-plastic deformation behavior of 3d-foam structures. *Advanced Engineering Materials 24*, 2 (2021), 2100641.

[96] Martens, J., et al. Deep learning via hessian-free optimization. In *ICML* (2010), vol. 27, pp. 735–742.

[97] Mathieu, J. Adaptive Sampling Algorithmus für die Generierung von Trainingsdaten zur Vorhersage konstitutiven Verhaltens auxetischer Strukturen. 2022.

[98] Mauko, A., Fíla, T., Falta, J., Koudelka, P., Rada, V., Neuhäuserová, M., Zlámal, P., Vesenjak, M., Jiroušek, O., and Ren, Z. Dynamic deformation behaviour of chiral auxetic lattices at low and high strain-rates. *Metals 11*, 1 (2021), 52.

[99] McCulloch, W. S., and Pitts, W. A logical calculus of the ideas immanent in nervous activity. *The bulletin of mathematical biophysics 5*, 4 (1943), 115–133.

[100] McKay, M., and Conover, W. Rj beckman a comparison of three methods for selecting values of input variables in the analysis of output from a computer code. *Technometrics 21* (1979), 239–245.

[101] Meiners, W., Wissenbach, K., and Gasser, A. Fraunhofer ges forschung, germany,'shaped body especially prototype or replacement part production'. *German Patent 19* (1998), 649–865.

[102] Milton, G. W., and Cherkaev, A. V. Which elasticity tensors are realizable? *Journal of Engineering Materials and Technology* (1995).

[103] Minsky, M. L., and Papert, S. A. *Perceptrons: expanded edition*. MIT press, 1988.

[104] Mizzi, L., and Spaggiari, A. Lightweight mechanical metamaterials designed using hierarchical truss elements. *Smart Materials and Structures 29*, 10 (2020), 105036.

[105] Mizzi, L., and Spaggiari, A. Chiralisation of euclidean polygonal tessellations for the design of new auxetic metamaterials. *Mechanics of Materials 153* (2021), 103698.

[106] Mockus, J., Tiesis, V., and Zilinskas, A. The application of bayesian methods for seeking the extremum. *Towards global optimization 2*, 117-129 (1978), 2.

[107] Müller, A. C., and Guido, S. *Introduction to machine learning with Python: a guide for data scientists*. " O'Reilly Media, Inc.", 2016.

[108] Nielsen, M. A. *Neural networks and deep learning*, vol. 25. Determination press San Francisco, CA, USA, 2015.

[109] Nocedal, J., and Wright, S. J. *Numerical optimization 2nd*. Springer, 2006.

[110] Novak, N., Starčevič, L., Vesenjak, M., and Ren, Z. Blast response study of the sandwich composite panels with 3d chiral auxetic core. *Composite Structures 210* (2019), 167 – 178.

[111] Novak, N., Vesenjak, M., and Ren, Z. Crush behaviour of auxetic cellular structures. *Science and Technology of Materials 30*, 1 (2018), 4–7.

[112] Novak, N., Vesenjak, M., Tanaka, S., Hokamoto, K., and Ren, Z. Compressive behaviour of chiral auxetic cellular structures at different strain rates. *International Journal of Impact Engineering* (2020), 103566.

[113] Osisanwo, F., Akinsola, J., Awodele, O., Hinmikaiye, J., Olakanmi, O., and Akinjobi, J. Supervised machine learning algorithms: classification and comparison. *International Journal of Computer Trends and Technology (IJCTT) 48*, 3 (2017), 128–138.

[114] Paturi, U. M. R., Cheruku, S., Pasunuri, V. P. K., Salike, S., Reddy, N., and Cheruku, S. Machine learning and statistical approach in modeling and optimization of surface roughness in wire electrical discharge machining. *Machine Learning with Applications 6* (2021), 100099.

[115] Polyak, B. T. Some methods of speeding up the convergence of iteration methods. *Ussr computational mathematics and mathematical physics 4*, 5 (1964), 1–17.

[116] Qi, D., Hu, W., Xin, K., Zeng, Q., Xi, L., Tao, R., Liao, H., Deng, Y., Liao, B., and Wu, W. In-situ synchrotron x-ray tomography investigation of micro lattice manufactured with the projection micro-stereolithography (pμsl) 3d printing technique: Defects characterization and in-situ shear test. *Composite Structures 252* (2020), 112710.

[117] Quadrelli, D. E., Casieri, M. A., Cazzulani, G., La Riviera, S., and Braghin, F. Experimental validation of a broadband pentamode elliptical-shaped cloak for underwater acoustics. *Extreme Mechanics Letters 49* (2021), 101526.

[118] Querin, O., Steven, G., and Xie, Y. Evolutionary structural optimisation (eso) using a bidirectional algorithm. *Engineering Computations 15*, 8 (1998), 1031–1048.

[119] Raissi, M., Perdikaris, P., and Karniadakis, G. E. Physics-informed neural networks: A deep learning framework for solving forward and inverse problems involving nonlinear partial differential equations. *Journal of Computational physics 378* (2019), 686–707.

[120] Rosenblatt, F. Perceptron simulation experiments. *Proceedings of the IRE 48*, 3 (1960), 301–309.

[121] Rozvany, G. I., Zhou, M., and Birker, T. Generalized shape optimization without homogenization. *Structural Optimization 4*, 3-4 (1992), 250–252.

[122] Rumelhart, D. E., Hinton, G. E., and Williams, R. J. Learning representations by back-propagating errors. *nature 323*, 6088 (1986), 533–536.

[123] Saxe, A. M., McClelland, J. L., and Ganguli, S. Exact solutions to the nonlinear dynamics of learning in deep linear neural networks. *arXiv preprint arXiv:1312.6120* (2013).

[124] Saxena, K. K., Das, R., and Calius, E. P. Three decades of auxetics research- materials with negative poisson's ratio: a review. *Advanced Engineering Materials 18*, 11 (2016), 1847–1870.

[125] Scarpa, F., Pastorino, P., Garelli, A., Patsias, S., and Ruzzene, M. Auxetic compliant flexible pu foams: static and dynamic properties. *Physica Status Solidi (B) 242*, 3 (2005), 681–694.

[126] Schittny, R., Bückmann, T., Kadic, M., and Wegener, M. Elastic measurements on macroscopic three-dimensional pentamode metamaterials. *Applied Physics Letters 103*, 23 (2013), 231905.

[127] Sejnowski, T. J., and Rosenberg, C. R. Parallel networks that learn to pronounce english text. *Complex systems 1*, 1 (1987), 145–168.

[128] Settgast, C., Abendroth, M., and Kuna, M. Constitutive modeling of plastic deformation behavior of open-cell foam structures using neural networks. *Mechanics of Materials 131* (2019), 1–10.

[129] Shanno, D. F. Conditioning of quasi-newton methods for function minimization. *Mathematics of computation 24*, 111 (1970), 647–656.

[130] Siebertz, K., van Bebber, D., and Hochkirchen, T. *Versuchspläne*. Springer, 2010.

[131] Sigmund, O. Tailoring materials with prescribed elastic properties. *Mechanics of Materials 20*, 4 (1995), 351–368.

[132] Skiena, S. S. *The data science design manual*. Springer, 2017.

[133] Stigler, S. M. Gauss and the invention of least squares. *the Annals of Statistics* (1981), 465–474.

[134] Sun, Z., Shi, Y., Sun, X., Jia, H., Jin, Z., Deng, K., and Yang, J. Underwater acoustic multiplexing communication by pentamode metasurface. *Journal of Physics D: Applied Physics 54*, 20 (2021), 205303.

[135] Surjadi, J. U., Gao, L., Du, H., Li, X., Xiong, X., Fang, N. X., and Lu, Y. Mechanical metamaterials and their engineering applications. *Advanced Engineering Materials 21*, 3 (2019), 1800864.

[136] Tamura, R., Osada, T., Minagawa, K., Kohata, T., Hirosawa, M., Tsuda, K., and Kawagishi, K. Machine learning-driven optimization in powder manufacturing of ni-co based superalloy. *Materials & Design 198* (2021), 109290.

[137] Tibshirani, R. J., and Efron, B. An introduction to the bootstrap. *Monographs on statistics and applied probability 57* (1993), 1–436.

[138] Tieleman, T., and Hinton, G. Lecture 6.5-rmsprop, coursera: Neural networks for machine learning. *University of Toronto, Technical Report 6* (2012).

[139] Tosi, P., Sbarra, P., and De Rubeis, V. Earthquake sound perception. *Geophysical Research Letters 39*, 24 (2012).

[140] VanderPlas, J. *Python data science handbook: Essential tools for working with data*. " O'Reilly Media, Inc.", 2016.

[141] Veronda, D., and Westmann, R. Mechanical characterization of skin—finite deformations. *Journal of biomechanics 3*, 1 (1970), 111–124.

[142] Wang, X., Jiang, M., Zhou, Z., Gou, J., and Hui, D. 3d printing of polymer matrix composites: A review and prospective. *Composites Part B: Engineering 110* (2017), 442–458.

[143] Wang, X.-T., Li, X.-W., and Ma, L. Interlocking assembled 3d auxetic cellular structures. *Materials & Design 99* (2016), 467–476.

[144] Wong, J., Gong, A. T., Defnet, P. A., Meabe, L., Beauchamp, B., Sweet, R. M., Sardon, H., Cobb, C. L., and Nelson, A. 3d printing ionogel auxetic frameworks for stretchable sensors. *Advanced Materials Technologies 4*, 9 (2019), 1900452.

[145] Wong, K. V., and Hernandez, A. A review of additive manufacturing. *ISRN Mechanical Engineering 2012* (2012).

[146] Wu, W., Hu, W., Qian, G., Liao, H., Xu, X., and Berto, F. Mechanical design and multifunctional applications of chiral mechanical metamaterials: A review. *Materials & Design 180* (2019), 107950.

[147] Wu, W., Qi, D., Hu, W., Xi, L., Sun, L., Liao, B., Berto, F., Qian, G., and Xiao, D. Synchrotron x-ray micro-computed tomography imaging of 3d re-entrant micro lattice during in situ micro compression experimental process. *Materials & Design 192* (2020), 108743.

[148] Wu, W., Qi, D., Liao, H., Qian, G., Geng, L., Niu, Y., and Liang, J. Deformation mechanism of innovative 3d chiral metamaterials. *Scientific reports 8*, 1 (2018), 1–10.

[149] Xiong, B., Zhao, X., Hu, Y., Huang, H., Liu, Y., and Su, Y. Machine learning assisted empirical formula augmentation. *Materials & Design 210* (2021), 110037.

[150] Yang, H., Wang, B., and Ma, L. Mechanical properties of 3d double-u auxetic structures. *International Journal of Solids and Structures 180* (2019), 13–29.

[151] Yang, W., Li, Z.-M., Shi, W., Xie, B.-H., and Yang, M.-B. Review on auxetic materials. *Journal of Materials Science 39*, 10 (May 2004), 3269–3279.

[152] Yap, C. Y., Chua, C. K., Dong, Z. L., Liu, Z. H., Zhang, D. Q., Loh, L. E., and Sing, S. L. Review of selective laser melting: Materials and applications. *Applied physics reviews 2*, 4 (2015), 041101.

[153] Yu, X., Zhou, J., Liang, H., Jiang, Z., and Wu, L. Mechanical metamaterials associated with stiffness, rigidity and compressibility: A brief review. *Progress in Materials Science 94* (2018), 114–173.

[154] Zadpoor, A. A. Mechanical meta-materials. *Materials Horizons 3*, 5 (2016), 371–381.

[155] Zeiler, M. D. Adadelta: an adaptive learning rate method. *arXiv preprint arXiv:1212.5701* (2012).

6

Appendix

6.1 Publications

1. A. Jung, S. Bronder, S. Diebels, M. Schmidt, & S. Seelecke (2018). Thermographic investigation of strain rate effects in Al foams and Ni/Al hybrid foams. *Materials & Design*, 160, 363-370.

2. M. Adorna, S. Bronder, J. Falta, P. Zlámal, & T. Fíla (2019). Evaluation of Hopkinson bar experiments using multiple digital image correlation software tools. *In Proceedings of the 17th Youth Symposium on Experimental Solid Mechanics, YSESM* (pp. 1-5).

3. S. Bronder, S. Diebels, & A. Jung (2021). Neural networks for structural optimisation of mechanical metamaterials. *PAMM*, 20(1), e202000238.

4. T. Fíla, P. Koudelka, J. Falta, P. Zlámal, V. Rada, M. Adorna, S. Bronder, & O. Jiroušek (2021). Dynamic impact testing of cellular solids and lattice structures: Application of two-sided direct impact Hopkinson bar. *International Journal of Impact Engineerin*g, 148, 103767.

5. S. Bronder, M. Adorna, T. Fíla, P. Koudelka, J. Falta, O. Jiroušek, & A. Jung (2021). Hybrid auxetic structures: Structural optimization and mechanical characterization. *Advanced Engineering Materials*, 23(5), 2001393.

6. S. Bronder, F. Herter, A. Röhrig, D. Bähre, & A. Jung (2022). Design Study for Multifunctional 3D Re-entrant Auxetics. *Advanced Engineering Materials*, 24(1), 2100816.

7. S. Bronder, F. Herter, D. Bähre, & A. Jung (2022). Optimized design for modified auxetic structures based on a neural network approach. *Materials Today Communications*, 32, 103931.

8. S.Grednev, S. Bronder, F. Kunz, M. Reis, S. M. Kirsch, F. Welsch, S. Seelecke, S. Diebels, & A. Jung (2022). Applicability of correlated digital image correlation and infrared thermography for measuring mesomechanical deformation in foams and auxetics. *GAMM-Mitteilungen*, 45(3-4), e202200014.

6.2 Presentations

1. S. Bronder , M. Adorna, T. Fíla, P. Koudelka, O. Jiroušek , A. Jung
   "Structural Optimisation of Hybrid Auxetic Structures"
   InCell conference, September 19-20 2019, Maribor, Slovenia

2. S. Bronder , S. Diebels , A. Jung
   "Neural Networks for Structural Optimisation of Mechanical Metamaterials"
   91st GAMM Annual Meeting, March 15-19 2021, Kassel, Germany

3. S. Bronder , F. Herter, S. Diebels , A. Jung
   "Neural Network Supported Optimisation of Modified Auxetics" ACEX, July 3-7 2022, Florence, Italy

6.3 Poster

1. S. Bronder , S. Diebels , A. Jung
   "Optimisation of Mechanical Metamaterials with Neural Networks" Doktorandentag der Fakultät NT, Saarland University, Januar 2020, Saarbrücken, Germany